Fast non-destructive internal state detection of neutral atoms in optical potentials

Dissertation
zur
Erlangung des Doktorgrades (Dr. rer. nat.)
der
Mathematisch-Naturwissenschaftlichen Fakultät
der
Rheinischen Friedrich-Wilhelms-Universität Bonn

von

Miguel Martínez Dorantes

aus

Tecámac, Mexiko

Bonn, Februar 2016

Dieser Forschungsbericht wurde als Dissertation von der Mathematisch-Naturwissenschaftlichen Fakultät der Universität Bonn angenommen und ist auf dem Hochschulschriftenserver der ULB Bonn `http://hss.ulb.uni-bonn.de/diss_online` elektronisch publiziert.

1. Gutachter:	Prof. Dr. Dieter Meschede
2. Gutachter:	Prof. Dr. Peter Reiter
Tag der Promotion:	24.05.2016
Erscheinungsjahr:	2016

Abstract

Neutral atoms trapped in optical lattices are promising candidates for quantum information processing and quantum simulation. Over the last decades, elegant tools for the manipulation of the internal and external states of optically trapped atoms have been developed. The crucial capability of scalable internal state readout in these systems, however, still relies on destructive methods. In spite of the important role of near-resonant illumination for the manipulation and detection of atoms in the lattice, there also exists a significant lack of studies on the heating and cooling dynamics of optically trapped atoms interacting with near-resonant light. An in-depth understanding of the heating and cooling processes is essential to finding the conditions of illumination that enable the non-destructive internal state readout of multiple atoms.

This work presents an experimental system to cool, trap, manipulate, and detect the internal and external states of a small ensemble of ^{87}Rb neutral atoms trapped in a one-dimensional optical lattice. A high photon detection efficiency in our experimental system allows for fast fluorescence imaging with acquisition times of 20 ms and fast position determination of atoms in the optical lattice with an accuracy of ~ 40 nm.

Using this experimental system, we investigate the heating dynamics of a neutral atom trapped in a standing wave dipole trap illuminated by a single near-resonant laser beam. A theoretical description to describe our measurements is provided in two experimentally relevant regimes. First, we consider the case of a weak near-resonant beam and later the case of off-resonant illumination. From this analysis, we find settings for the illumination light which allows an atom to scatter many photons before it is expelled from the trap.

Building on these results we demonstrate simultaneous, non-destructive determination of the internal state of spatially resolved atoms trapped in a one-dimensional optical lattice with a fidelity of $98.6 \pm 0.2\%$ and a survival probability of $99.0 \pm 0.2\%$. During the readout process, less than 2% of the atoms change their initial ground state.

In order to determine the state of atoms that are not spatially resolved, a novel image analysis technique is presented. The technique uses Bayesian methods, which include the statistics of the detected photons as well as the response from the EMCCD camera. The Bayesian method is implemented on experimental data for atoms trapped in a one-dimensional optical lattice and its accuracy is tested by numerical simulations. In addition, an extension of this algorithm for atoms trapped in two-dimensional lattices is provided.

Finally, the non-destructive state detection method is utilized as a tool for the state determination following the coherent control of the internal and external states of atoms in the optical trap. Here Raman sideband cooling is implemented and utilized in an atomic compression sequence for the creation of a small and dense atomic ensemble. These techniques will play an important role in experiments studying the collective light interaction of the atomic ensemble in a recently added optical fiber cavity.

Contents

CHAPTER 1

Introduction

The transmission of information between two parties has been an essential part of the evolution of human society. The necessity for a secure communication has been always present, and it is nowadays of vital importance for the stability of the complex human society in the information age in the 21st century. Different ways to encode messages have emerged through the centuries giving birth to the field of cryptography. A breakthrough in secure communication was achieved by the invention of the so-called one-time pad encryption [1, 2], which uses a symmetric, random secret key shared between sender and receiver. This is an optimal method and, in principle, cannot be broken provided the parties do not reuse their key [3]. To use this scheme the two parties, however, must have a secure channel to share the secret key.

Quantum mechanics provides a channel where the security relies on basic principles of quantum physics [4]. This was proposed by Bennett and Brassard [5, 6] and Ekert [7] who have created a scheme to share a secret key protected by the impossibility of copying a quantum state. The distribution of quantum states, carried by single photons, over long distances is in practice limited by the losses in the communication channels. In contrast to a classical communication channel, quantum information cannot be amplified since amplification, i.e. copying of the quantum state, is not possible. A solution for the problems caused by the losses in the transmission channels has been proposed by using the so-called *quantum repeater* scheme [8, 9], where a quantum memory is an essential element necessary to store and retrieve information, i.e. qubits, at will.

The internal states of neutral atoms are prominent candidates for the storage of qubits. In particular, atoms trapped in optical lattices are systems with ideal characteristics [10]. The tight confinement in a 3D lattice guarantees that the atoms are localized in a small region and limits their movement over distances much smaller than the wavelength of the light used to encode the information. The fixed locations of the atoms are a prerequisite for long survival of the spin wave since the motion of atoms destroys the spin wave and impedes the retrieval of the collectively encoded information [8].

Over the last decades, a large variety of tools have been developed allowing the manipulation and detection of neutral atoms trapped in optical lattices [11–14]. Coherent manipulation of the internal and external degrees of freedom provide the means for a precise control of the internal states as well as the atomic motion, and has lead e.g. to the 3D cooling of an atom to its motional ground state [15–17]. These tools have been used to perform a wide variety of experiments, from individual quantum systems [18–20] up to quantum many body systems containing thousands of atoms [21–26]. The scalability of quantum systems is not only essential for practical applications, such as quantum information storage and

processing [27–30], or optical atomic clocks [31–33], but it also enables the investigation of fundamental quantum effects. The control at the single atom level has provided experimentalists with the ability to simulate complicated physical systems, e.g. in solid state physics, by using atoms trapped in optical lattice showing their potential to implement quantum simulators [34–37].

Information on atoms trapped in optical lattices is in general obtained by the interaction between light and the trapped atom. For example, by illuminating the atoms with near-resonant light and collecting the atomic fluorescence with a high-resolution optical system, it is possible to determine with high accuracy the number of atoms trapped in an optical lattice as well as their exact localization in the trap [38].

Optical readout can also extract information about an atom's internal and external degrees of freedom. For example, by sideband spectroscopy, it is possible to determine the vibrational state of an atom. In most experiments it is required to determine the internal state of an atom with high precision. Current techniques for the detection of the internal state of multiple atoms in an optical lattice rely on a destructive "push-out" method [39]. Using this method, atoms in one hyperfine ground state are pushed out of the trap when they are illuminated by a strong resonant beam, while atoms in another hyperfine ground state are off-resonant to the illumination light and, therefore, remain trapped. With this destructive technique it is possible to estimate their initial ground state from the atoms that survive the push-out beam. The method has a high fidelity at the cost of removing the atoms from the trap. On the other hand, non-destructive methods to determine the internal state for a single atom have been implemented, for example by using an high finesse optical cavity [40–42] and more recently by resonance fluorescence for single atoms in free space [43, 44]. However, up until now there is no technique that allows the determination of the internal state of multiple atoms trapped in an optical lattice in a non-destructive fashion.

In this work, I present a new non-destructive tool that allows for a fast and simultaneous determination of the internal state of multiple atoms trapped in a one-dimensional optical lattice by state dependent fluorescence. The thesis is structured as follows:

In the first chapter, the experimental apparatus is described. Atoms are cooled in a small magneto-optical trap and transferred into a one-dimensional tightly focused optical lattice. There a large numerical aperture lens allows for the precise determination of the atoms' positions in the optical lattice.

In the second chapter, we study the heating mechanisms present during the interaction between an optically trapped neutral atom and a near-resonant optical field. We find conditions for the illumination field that minimize the heating induced by this process allowing an atom to scatter a large number of photons before it is expelled from the trap.

In the third chapter, I utilize the results obtained in Chapter 2 to implement state-dependent near-resonance fluorescence, which allows non-destructive state detection. In addition, we present a novel technique that uses Bayesian methods to include information about the experimental system in order to improve the fidelity of the readout process. This is experimentally implemented for atoms trapped in a 1D optical lattice, and an extension for 2D traps is provided.

In the last chapter, the non-destructive method is utilized as a tool for the state detection following the coherent manipulation of the internal and external states of atoms in the trap. Here, Raman sideband cooling is implemented and utilized in an atomic compression sequence for the creation of a small and dense atomic ensemble [45].

CHAPTER 2

Tools for atom cooling, trapping and detection

Optical cooling and trapping of neutral atoms represent one of the most elegant methods in experimental physics and has opened a new range of possibilities by allowing access to ultra-low energies. These techniques have lead to the ability to resolve and manipulate individual atoms in traps containing from a single atom [18, 38, 46] up to thousands of them [21, 22, 24–26]. The large versatility of these systems has increased the spectrum for different applications such as fundamental test of quantum mechanics [47], quantum information [28], and quantum simulation [48].

The fast technological progress in the last decades has shown the benefits of miniaturization and integration, not only for scientific research but also in the everyday life. Integration of optical elements in experimental systems for the study of ultracold atoms allows the usage of short focal length and large numerical aperture lenses to create robust and efficient systems. These optical elements can be used to create deep potentials, with a size of a few micrometers, and at the same time provide the means for a fast and precise detection of individual atoms inside the traps.

In this chapter, I present the experimental system used to cool, trap, and detect a small ensemble of neutral ^{87}Rb atoms. In Sec. 2.1 a general overview of the main setup is introduced. In Secs. 2.2 and 2.3 the implementation of a small magneto-optical trap and a tightly-focused 1D optical lattice is presented. Finally, Sec. 2.4 describes the detection of ^{87}Rb neutral atoms in the optical lattice by fluorescence imaging. The technique presented in this last section allows a precise determination of the position of individual atoms in the optical lattice, the precision of this method is quantitatively analyzed.

2.1 Experimental setup overview

Laser cooling, trapping, and detection of neutral atoms, require three basic components: an ultra-high vacuum chamber, electromagnets, and detection optics. The first is needed to isolate the atoms under study from interactions with the surrounding gas. The second, to generate the magnetic fields used for atom trapping and manipulation. The third is necessary to collect the atomic fluorescence in order to observe and obtain information from the atoms. In this section, the implementation of the three components in our system is described.

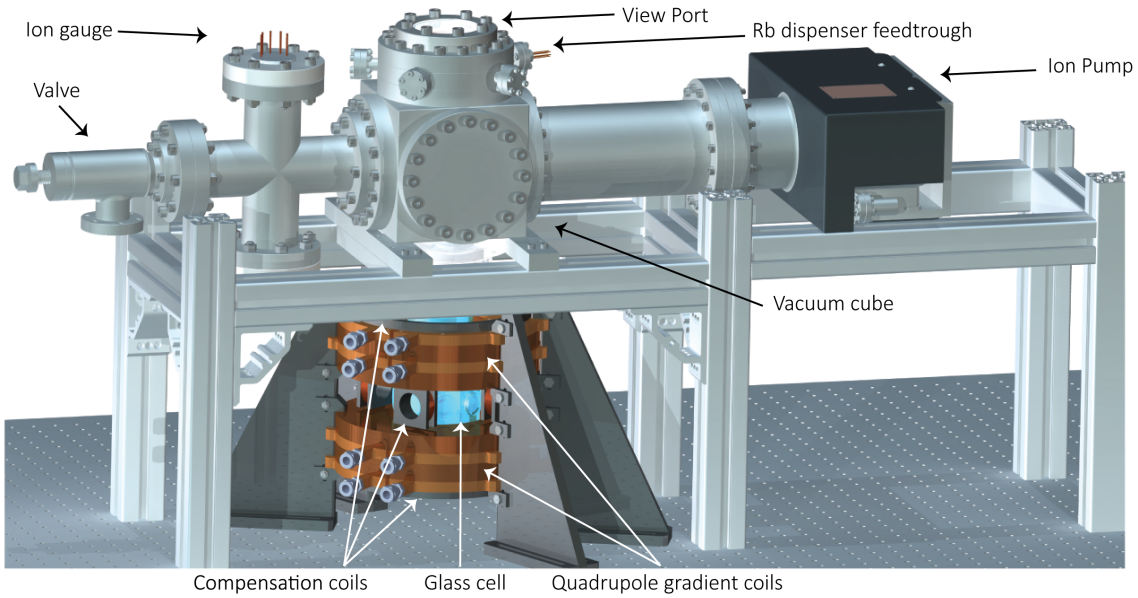

Figure 2.1. *Experimental chamber.* The ultra-high vacuum chamber is mounted on an optical table. The glass cell is located inside the quadrupole gradient coils

2.1.1 Ultra-high vacuum chamber

To store atoms in optical traps, it is necessary to reduce the background gas pressure in order to decrease the probability that a background particle collides with a trapped atom and removes it from the trap. In typical experiments, it is required that atoms are held in place, at least, for a few seconds. Therefore, an Ultra-High Vacuum (UHV) environment is required. The layout of the constructed UHV chamber is shown Fig. 2.1. To achieve the required UHV, the chamber was evacuated using two turbo pumps[1] in series while keeping the chamber temperature at 120°C for two weeks[2]. Then, the chamber was closed using an all-metal valve[3] and cooled down to room temperature reaching a pressure of 2.1×10^{-10} mbar, measured from the display on the ion pump.

Vacuum pump. In the system, an ion pump from Agilent Technologies, (model VacIon Plus 75) was installed. Ion pumps provide a continuous vacuum with no mechanical vibrations allowing to reach pressures down to 10^{-11} mbar. Due to the intense magnetic fields generated by the permanent magnets inside the pump, it is preferable to place the ion pump far from the location where the atoms are trapped.

Rubidium source. The ^{87}Rb source is stored in three alkali metal dispensers[4] that allow for ^{87}Rb emission on demand. One of the dispensers was entirely used after closing the system to coat the internal walls of the UHV chamber before providing a uniform Rb background pressure gas.

Glass cell. To manipulate and cool neutral atoms, it is necessary to switch on and off magnetic fields within a few milliseconds. This fast switching generates eddy currents in the metallic components of the

[1] Pfeiffer, Model TSU 071 E.
[2] Previously, the metallic components were baked at 250 °C.
[3] Hositrad, model VMD38CF35R.
[4] SAES, model RB/Nf/3.4/12/FT.

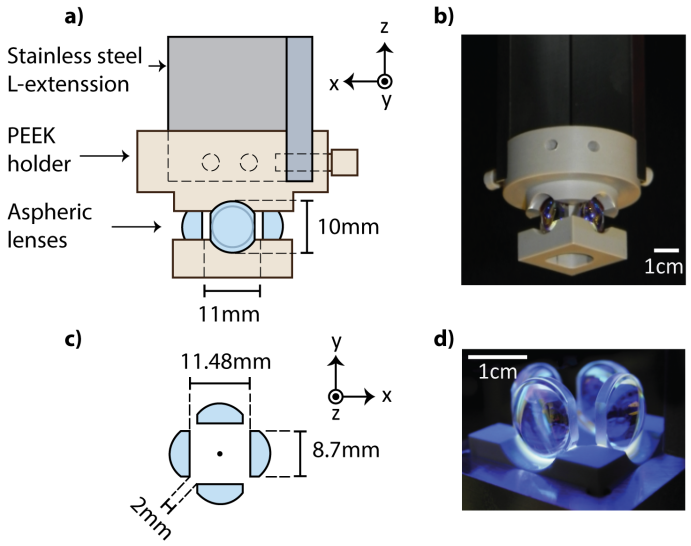

Figure 2.2. *Aspheric lenses* **a)** Diagram of the aspheric lenses mounted in a PEEK holder connected to an L-shaped stainless steel extension. **b)** Photography of the lens assembly mounted on a stainless steel L-shaped extension prior to inserting it into the vacuum chamber. **c)** Top view of the aspheric lenses array. All lenses are aligned to the same focal point. **d)** Photography of the four lenses during the UV-glue curing process. In this picture, they are glued just to the lower part of the holder.

UHV chamber, which limits the duty cycle of an experiment. The usage of a glass cell is ideal to reduce the effect of such eddy currents. In the UHV system, we use a custom octagonal glass cell from the company Precision Glass Blowing, which has a (non-optical) quartz body with nine optical windows each with Anti-Reflection (AR) coating on both sides (see Fig. 2.3a). The cell is attached to the chamber via a glass to metal transition. The AR coating provides a reflectivity $< 1.5\%$ per surface for 780-1060 nm, which means that each window transmits $\sim 97\%$ of the light. The delivered glass cell, though, has a coating quality below manufacturing specifications. From the 3% of the light that is not transmitted approximately one quarter of it is dispersed, which represents ten times the dispersion of a standard optical element with a similar coating.

2.1.2 In-vacuum aspheric lenses

Detection of individual atoms trapped in optical potentials with a size of just a few micrometers relies on the development of efficient optical systems with a diffraction limited performance. A high Numerical Aperture (NA) is desirable for a better image resolution and to increase the number of collected photons emitted by an atom. Common solutions for this application are either large working distance microscope objectives [22, 49] or in-vacuum aspheric lenses with a shorter focal length [50]. Besides the low cost, an aspheric lens has the advantage that it can be placed inside the UHV system, avoiding experimental constraints such as optical compensation for imaging through a window of the vacuum cell, or other specific geometrical restrictions. Furthermore, the short focal length provides better pointing stability.

The core of our optical system consists of four aspheric lenses with a NA=0.5, a working distance of 5.9 mm, and an effective focal length of 8 mm[5]. The set of lenses is arranged such that all lenses have the same focal point (see Fig. 2.2c). These lenses were designed by the manufacturer for laser diode collimation, the factory design considers the effect of a glass window present on the laser diodes. However, they can be used as an objective lens for single atom imaging by using an extra long focal distance lens to compensate for the absence of the glass window, restoring the aberration-free operation [50]. To provide better optical access for the MOT beams, a small portion of the edge of the four lenses was removed,

[5] Lightpath 352240, anti-reflection B-coated.

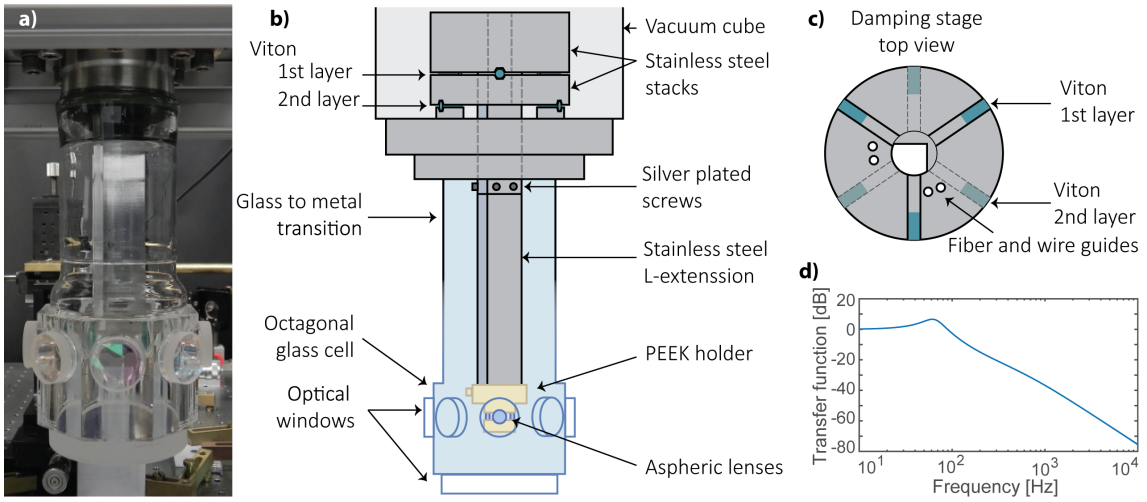

Figure 2.3. *Glass cell and damping Stage*. **a)** Octagonal glass cell mounted on the vacuum chamber with the set of aspheric lenses inside. **b)** Diagram showing the set of aspheric lenses mounted inside the chamber via the damping stage. **c)** Top view of the damping stage. **d)** Calculated transfer function for the two-stage vibration isolation system.

leaving intact the clear aperture of the lens (see Fig. 2.2d). The four lenses were carefully aligned and glued to a PEEK holder (see Appendix A), the PEEK holder is then attached to a damping stage by an L-shaped stainless steel bar and fixed with four silver plated screws inside the vacuum chamber (see Fig. 2.3).

For the design of the holder, it is important to avoid any metallic component that could reflect the microwave radiation that will be sent by an external antenna. For this reason, we have used PEEK as a material for the lens holder. PEEK is one of the few types of plastics that are suitable for UHV applications [51] and it is easily machined compared to brittle ceramic components.

2.1.3 Damping system

Measurements need to be performed in a vibration-free environment. To this end, the experimental chamber is mounted in a non-magnetic vibration isolation optical table. Optical tables are designed to reduce background noise caused by ambient vibrations, usually in the range from a few to 100 Hz. The air spring of the supporting structure for the table is designed by the manufacturer such that its first resonance is well above 100 Hz [52]. However, other sources of vibrations still affect the system, especially acoustic frequencies in the range of 0.1-20 kHz. Remaining effects of external perturbations in the low-frequency range can be reduced by active feedback techniques, which have a typical bandwidth of a few kilohertz and can be implemented, e.g. by using piezoelectric elements [53].

Vibrations above a hundred kHz create perturbations that cannot be actively compensated. To reduce the effect of such high frequencies, the lens system is mounted on a passive vibration isolation stage inside the UHV system. The design of the stage was inspired by Ref. [54], it consists of two stainless steel stacks[6] separated by Viton® rubber dampers. Viton® is an elastomer that is chemically stable and it has

[6] With a mass of 0.6 and 2.2 Kg respectively.

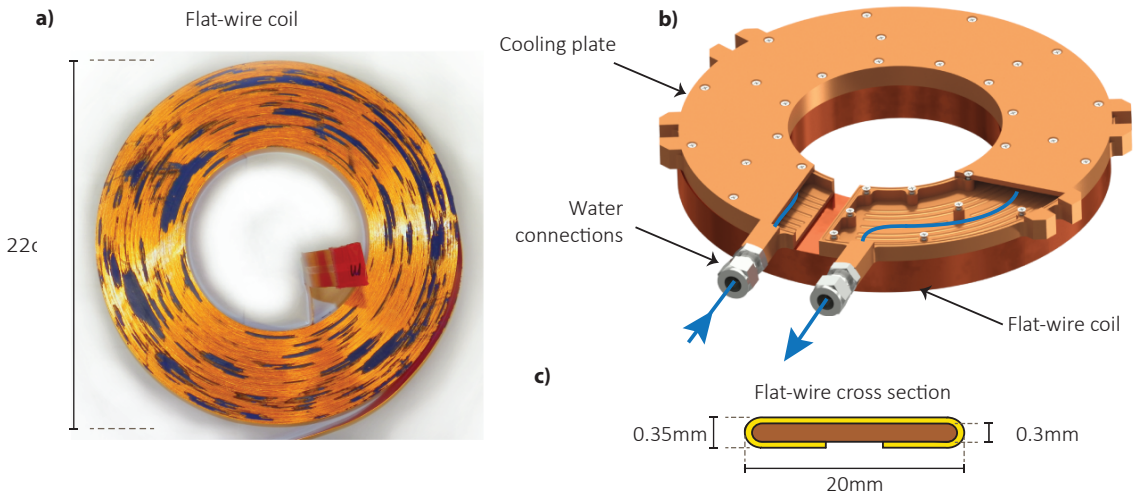

Figure 2.4. *Magnetic gradient coils.* **a)** Picture of flat-wire coil with 125 turns. **b)** Drawing of the water cooling plate. **c)** Flat-wire cross section.

physical characteristics that make it ideal to be used inside UHV systems[7]. It is relatively incompressible due to its high compressive stiffness, thus providing good long term stability. It also has a high internal damping, making it suitable to be used as a damper for the vibration isolation stage [55]. Small cylinders of Viton® with 6 mm diameter and 5 mm length were used as spacers. Each stage is separated from the next one by a set of three spacers placed 120° from each other. The next layer is rotated by 60°in order to avoid a direct line of sound [54]. The Viton® spacers rest in hexagonal shaped grooves, which provide good lateral stability (see Fig. 2.3b,c).

The transfer function of the damping stage can be modeled as a set of coupled damped harmonic oscillators [56–58]. From the estimated transfer function for the damping stage (see Fig. 2.3d), it is estimated a reduction of noise at frequencies above 0.1 kHz. The cut-off frequency and the amplitude of the first resonance could be lowered by increasing the mass as well as by including more stacks.

2.1.4 Magnetic field generation

To trap neutral atoms in a small volume, it is essential to have a fast and precise control over magnetic fields, in particular, the ability to create either uniform fields or strong magnetic gradients. Uniform fields can be created by a pair of coils in Helmholtz configuration for each spatial direction. The generation of a strong gradient is typically achieved by using a pair of coils assembled in anti-Helmholtz configuration leading to a quadrupole magnetic gradient. This section describes the set of electromagnets used to generate such magnetic fields.

Gradient Coils

For the design of the electromagnets used to generate the quadrupole gradient, two main aspects need to be considered: the coil dimensions and heat dissipation. It is ideal to choose the inner diameter of the coils as small as possible to reduce the driving current required. In our system, the inner dimensions of

[7] Down to 10^{-11}mbar [54].

the quadrupole coils are limited by the glass cell external diameter of 11 cm. Heat dissipation must be under control, excessive heat generated by high electric current densities may damage the coils. Even at low currents, the temperature variation of a few degrees will cause thermal expansion that can affect the stability of the field, especially for bulky coils systems. Therefore, for powers larger than few tens of watts water cooling is required.

The quadrupole gradient is generated by two stacks of coils in anti-Helmholtz configuration. Each stack consists of two coils with 125 turns of flat cooper wire (see Fig. 2.1a). The coils are glued[8] to a pair of home-built cooper cooling plates as shown in Fig. 2.4b. The optimum distance between the stacks, at which the maximum gradient is achieved, was estimated by numerically optimizing the coils system [59]. From the numerical simulation, a field gradient of $\frac{dB_z}{dz} = 4\,\text{Gauss/cm} \times \text{A}$ is expected. To reduce the induction of eddy currents, each plate has a slit at the center and the whole system is mounted on a plastic holder attached to the optical table.

For efficient heat dissipation, a good thermal contact between the electric conductor and the cooling plates is desirable. For this reason, we have used cooper flat-wire[9] with a cross section of $20\,\text{mm} \times 0.3\,\text{mm}$ to build the set of coils as shown in Fig. 2.4. This wire has the advantage that only a thin layer of 25 μm of Kapton® separates the conductor and the cooling plate. The fact that heat is directly conducted by copper itself allows for a great heat dissipation. Another advantage, compared to standard round wires, is the density of copper in the coil, which reduces the required size of the electromagnet. When a continuous current of 50 A is applied[10] to the quadruple coils, and water cooling at 17°C flows through the cooling plates (from the building's cooling system), the electromagnets reach an equilibrium temperature[11] of $\sim$ 45°C. Nevertheless, a high gradient is required just for a few milliseconds in most experimental sequences.

Compensation Coils

Compensation and bias magnetic fields are generated by three pairs of mutually orthogonal coils. The coils used to generate the field in the *xy* plane are wound around a plastic holder with an internal diameter of 3 cm using wire of 0.7 mm diameter cross section, each one containing 90 turns. The coil in the z direction has an internal diameter of 18.5 cm with the same number of turns and the same wire (see Fig. 2.1).

All compensation coils are powered by low-noise current power supplies[12], which provide stable current sources with a fast switching time. They run at a constant offset that is set to compensate earth's magnetic field but the offset value can be changed by adding a reference voltage via the computer card. However, when doing so, the stability of the current source is limited by the stability of the computer card. To take full advantage of the high stability of the supplies, a set of relays was added in order to disconnect the computer card from the power supplies when a stable field is required in the experimental sequence.

[8] Fischer electronik WLK 30 adhesive, thermally conductive, 30G.
[9] CMC 38390 Kapton® insulated flat wire.
[10] For this measurement we used a power supply from TET electronics model Hercules-5kW, but later it was exchanged to a power supply from Elektro-Automatik, model EA-PS-3016-20B that provides only up to 16 A.
[11] The temperature was measured on the outside part of the coil. Internally the temperature might be slightly higher.
[12] Toptica current controller, DC110 and two DC100, all providing up to 500 mA.

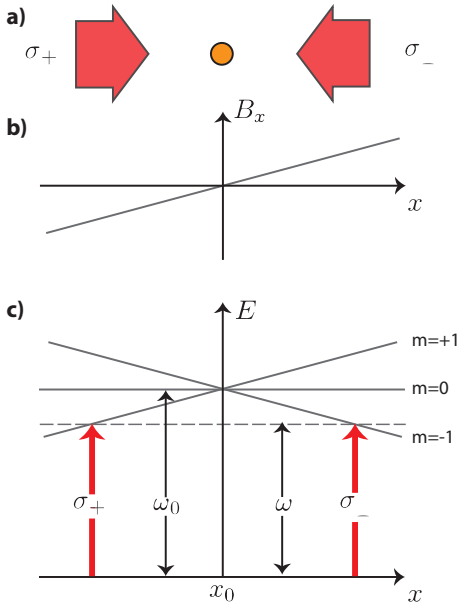

Figure 2.5. *Working principle of a MOT* **a)** Two counter-propagating beams, with a frequency ω and opposite circular polarization interacting with a two-level neutral atom with a resonance frequency ω_0. **b)** Position dependence of the MOT's magnetic field. **c)** Position dependence of the energy splitting for the Zeeman sub-levels.

2.2 A small magneto-optical trap

A Magneto-Optical Trap (MOT) is the essential element to cool and trap neutral atoms from a background gas at room temperature and it has been extensively discussed in the literature [60–63]. In this section, a very general description of the working principle of a MOT is presented and later we focus on the experimental implementation of a small MOT, which is used to capture from a single to a few tens of atoms.

2.2.1 Working principle

Doppler cooling. Atoms moving at velocity v in a monochromatic light field of frequency ω will experience the Doppler effect by observing a shift in the light frequency given by $\omega' = \omega \pm k \cdot v$, where k is the wave number. Atoms moving towards (away from) the light source observe a higher (lower) frequency. When the frequency of the light source is detuned an amount $\delta \approx -k \cdot v$ below the atomic resonance, atoms moving towards the light source see a resonant field leading to an increased photon absorption. In each absorption process, an atom preferentially receives a kick from the photon opposite to its direction of motion and, due to the random direction of the spontaneous emission, the total momentum of the atom is reduced in the direction of motion.

Optical Molasses. In an optical molasses, three orthogonal pairs of counter-propagating beams are used to reduce the momentum along all directions by Doppler cooling. Nevertheless, the energy cannot be arbitrarily reduced since the random nature of the spontaneous emission process acts as a dispersive mechanism that counteracts the Doppler cooling process. In the steady state this leads, for $\delta = -\Gamma/2$, to the *Doppler temperature* limit [64]

$$T = \frac{\hbar\Gamma}{2k_B},$$

where Γ and k_B are the natural decay rate and Boltzmann constant.

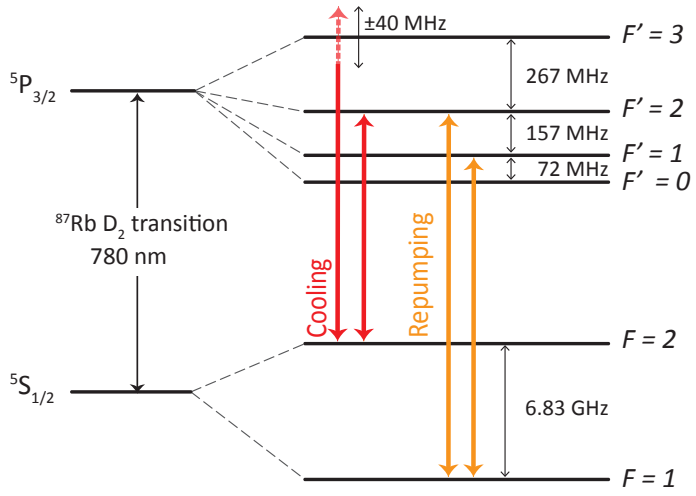

Figure 2.6. *Relevant ^{87}Rb D_2-line levels.* The cooling laser can be tuned to the $F = 2 \rightarrow F' = 3$ transition. The other light frequencies are fixed at the indicated transitions (frequency splittings are not up to scale and Zeeman levels are not shown).

Magneto-Optical Trap. An optical molasses reduces the kinetic energy of the atoms but these can still escape the cooling region due to the lack of a trapping force. To implement such spatial dependent force, a magnetic gradient is introduced, which creates a position-dependent radiation pressure. The working principle can be understood better with a 1D example. Assume that a two-level atom with three Zeeman sublevels, $m = -1, 0, +1$, interacts with two counter-propagating laser beams. The laser beams have orthogonal polarizations $\sigma_{\pm}$ and their frequency ω is detuned with respect to the atomic resonance ω_0 (see Fig. 2.5). The position dependence is introduced by a magnetic field gradient, which creates a linear shift on the Zeeman levels. An atom on the right side observes a frequency closer to resonance for the σ_- beam, which pushes the atom to the left. The equivalent happens in the opposite direction, pushing always the atom back to $x = 0$. The extension to 3D is straightforward by using three pairs or counter-propagating beams.

2.2.2 Experimental implementation

Laser system

To generate the beams required to create the MOT, we use two home built diode lasers. The frequency for both lasers is stabilized using polarization spectroscopy of Rubidium vapor cells [65–67]. The first laser, which will be referred as the *cooling* laser, provides a maximum power of 60 mW and it is locked to the crossover of the transitions $F = 2 \rightarrow F' = 2, 3$. Part of the laser light goes through an Acousto-Optical Modulator[13] (AOM) in double pass configuration to address the $F = 2 \rightarrow F' = 3$ transition, providing a frequency tuning range of ±40MHz. Both frequency and intensity of the beam are controlled via the computer card. The rest of the light is similarly frequency shifted to address the transition $F = 2 \rightarrow F' = 2$ (see Fig. 2.6).

The second laser, which will be referred as the *repumping* laser, provides up to 30 mW of power and is locked to the transition $F = 1 \rightarrow F' = 1$. Part of the light is sent through an AOM to address the transition $F = 1 \rightarrow F' = 2$. In this case, the intensity and frequency are fixed and the beams are turned on and off by using a radio frequency switch.

[13] Crystal Technology, LLC., Model: 3080-122 at 80 MHz central frequency.

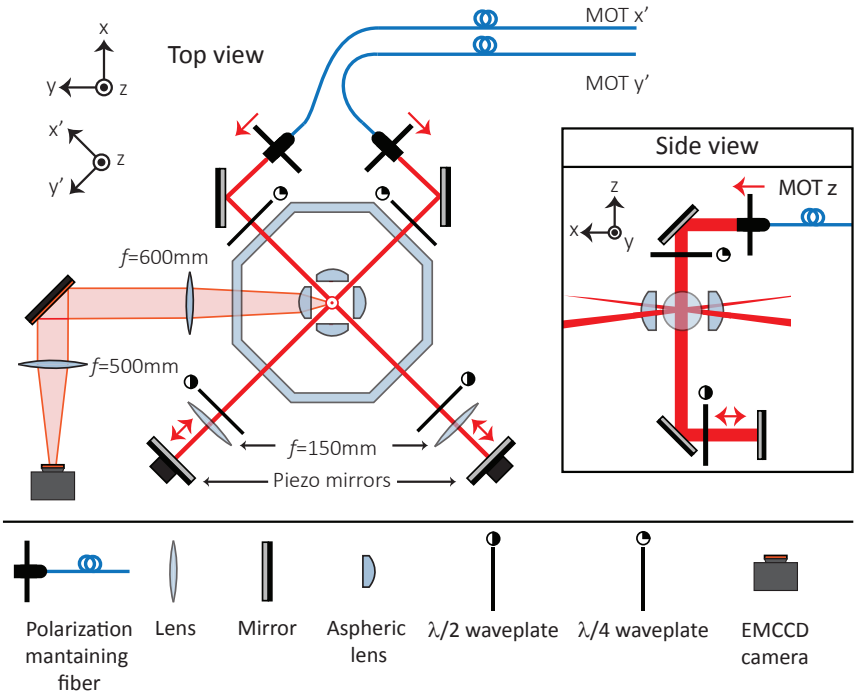

Figure 2.7. *Simplified MOT setup.* Light from the cooling ($F = 2 \rightarrow F' = 2$) and repumping ($F = 1 \rightarrow F' = 1$) transitions comes out of the optical fibers and it is retro-reflected creating the six cooling beams.

When fast switching is not necessary, the light is blocked by self-built loudspeaker mechanical shutters, with a switching time of ~ 5 ms, all of them are controlled by digital channels of the computer card.

MOT setup

Light from the cooling ($F = 2 \rightarrow F' = 2$) and repumping ($F = 1 \rightarrow F' = 1$) transitions is combined and coupled into three polarization maintaining optical fibers[14], which guide the light to the experimental chamber. Each beam is retro-reflected in order to create the six cooling beams required (see Fig. 2.7).

The size of the beams used to generate the MOT is limited by the gap between the aspheric lenses mounted inside the chamber (see Fig.2.2). To create the MOT for the first time, we used elliptical beams for the x' and y' beams with a size of $3\,\text{mm} \times 1\,\text{mm}$ (axis full width) and a round beam of 5 mm in diameter for the z direction. However, stray light generated by these beams severely limits the detection of single atoms, thus in the final setup, we use round beams on the xy plane with a diameter of 0.7 mm and 2 mm for the z beam.

The small waist of the beams along the x' and y' direction have a Rayleigh length of only 0.5 m, leading to a strong divergence. If this is not taken into account, the intensity of the retroreflected beam can be significantly different from the incoming beam at the position of the MOT, which leads to a large optical imbalance. To overcome this problem, a lens with a focal length of 150 mm is placed in a quasi cat's-eye

[14] All optical fibers mentioned in this work are single-mode polarization maintaining. This will be assumed unless something different is stated.

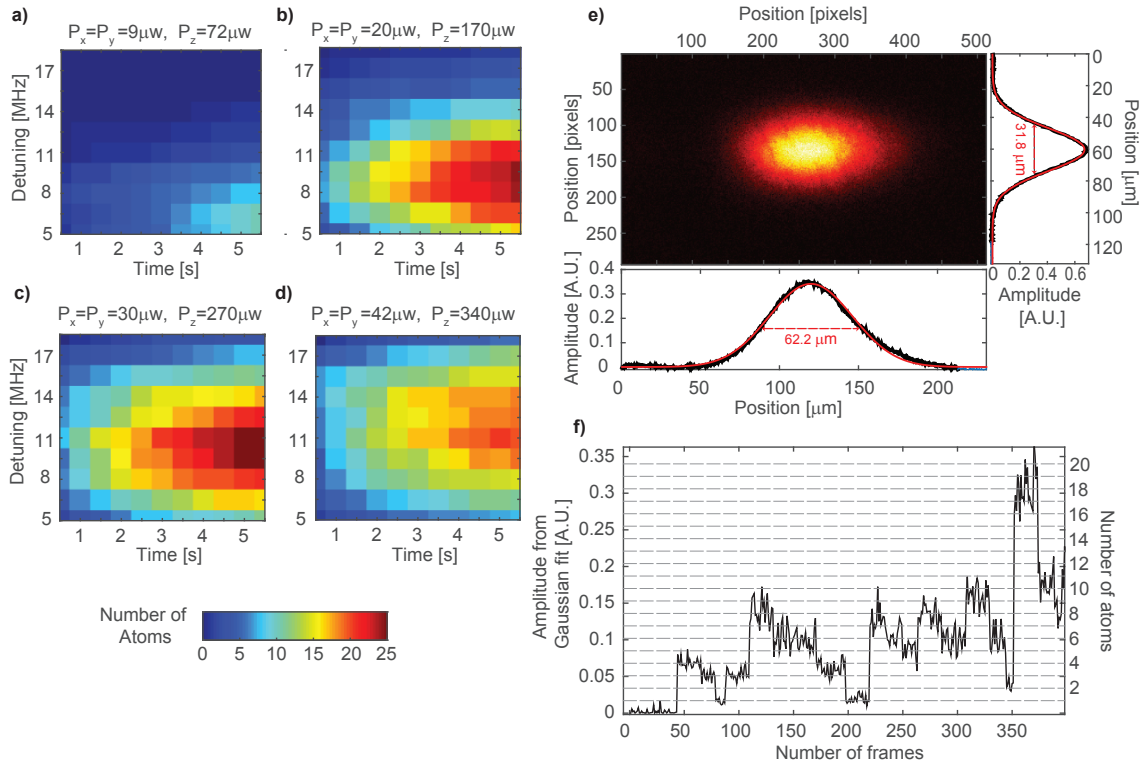

Figure 2.8. *MOT characteristics.* **a-d)** Number of atoms loaded in the MOT for different powers and frequencies. **e)** Image of the MOT acquired by the EMCCD. The plots at the right side and at the bottom show a Gaussian fit to the integrated image and the full width half maximum obtained from the fit. **f)** Variation of the fluorescence in the MOT as a function of time.

configuration such that the waist of the retro-reflected beam is slightly smaller than the original beam in order to compensate for the losses on the windows. The position of the lens was finally optimized by minimizing the variation of the MOT's position when the laser power is changed.

MOT Characteristics

The fluorescence of atoms in the MOT is collected by one of the aspheric lenses and imaged on an Electron Multiplying Charge Coupled Device (EMCCD) camera (see Sec. 2.4.3). The high-NA aspheric lens collects a large number of photons providing a signal to noise ratio enough to distinguish the entrance and exit of a single atom from a trap containing a few atoms [68–70]. This effect can be used to determine the number of detected counts per atom in the trap in order to estimate the total number of atoms contained in the MOT (see Fig. 2.8f).

Fig. 2.8a-d shows the loading characteristics for the MOT using a magnetic gradient of 40 Gauss/cm for different frequency detunings and intensities of the cooling laser. From the recorded data we determine the optimum set of parameters: $P_x = P_y = 30\,\mu\text{W}$ $P_z = 250\,\mu\text{W}$ for the cooling beams with a detuning of $\Delta = -2\pi \times 10\,\text{MHz}$, and a power $P_x = P_y = 6\,\mu\text{W}$ $P_z = 50\,\mu\text{W}$ for the repumper $F = 1 \rightarrow F' = 1$. Fig. 2.8e shows an image of the MOT for the optimum parameters after it has been loaded for 10 s. From

a Gaussian fit to the integrated image of the MOT, a size of $32 \times 62\,\mu m$ is obtained for the FWHM. In the image, the MOT contains $\sim$ 30 atoms.

2.3 Optical dipole trap

Optical dipole traps are powerful and versatile tools used in many laboratories to confine and manipulate ultracold neutral atoms for a large variety of applications, ranging from the control of an individual atom up to hundreds of thousands of atoms [11, 48]. This trapping technique relies on the electric dipole interaction between an atom and a far-detuned light field. A conservative force arises from the dispersive interaction and creates a potential proportional to the light's intensity. The absorptive part of the interaction leads to photon scattering, i.e. an atom absorbs a photon from the light field, which by spontaneous decay is emitted into free space. When the detuning of the light field with respect to the atomic resonance is large, scattering is strongly reduced, creating a quasi-conservative potential. In this section, I will focus on a quantum-mechanical description of a single atom interacting with a single-mode electromagnetic field using the dressed state formalism mainly following Cohen-Tannoudji's book [71]. Later, the experimental implementation and characterization of a tightly-focused 1D optical dipole trap is presented.

2.3.1 Monochromatic light interacting with a two-level atom: the dressed state approach

The interaction of a laser field with an atom is, in general, a complex problem and has been studied for a long time in the literature [72, 73]. To understand this interaction in an easy and useful way, it is convenient to use simplified models. The simplest model for an atom in free space is a two-level system with energy eigenstates $|g\rangle$ and $|e\rangle$, for the ground and excited states respectively, separated by an energy $\hbar\omega_0$. A laser beam can be pictured as a single-mode electromagnetic field inside a lossless resonant cavity containing a large number N of photons with energy $\hbar\omega_L$. The photon number must be large enough such that scattering of a few photons by the atom does not alter the field significantly and can be, therefore, completely neglected. The mode volume V of the cavity has to be large enough such that it does not modify the atomic decay rate. Both quantities photon number and mode volume can be arbitrarily large while keeping energy density $\langle N \rangle / V$ constant. Under these assumptions, the light field can be described using the Fock states $|N\rangle$ [71].

When the two systems, atom and light field, are brought together, it is natural to describe the system by choosing the manifold $\mathcal{E}(N) = \{|g, N\rangle\ ,\ |e, N-1\rangle\}$ where $|i, N\rangle = |i\rangle \otimes |N\rangle$ for $i = e, g$. The manifold $\mathcal{E}(N)$ is commonly refereed as the *bare states* and represents the eigenstates of the system when the atom-light coupling is not considered. The states in $\mathcal{E}(N)$ are separated by an energy $\hbar\Delta$, where $\Delta = \omega_L - \omega_0$ is the detuning from the atomic resonance. $\mathcal{E}(N)$ creates an infinite ladder of pair of states separated by an energy $\hbar\omega_0$ as shown in Fig. 2.9c.

The Hamiltonian describing the two-level atom interacting with a single mode electromagnetic field can be written in the rotating wave approximation (RWA) as

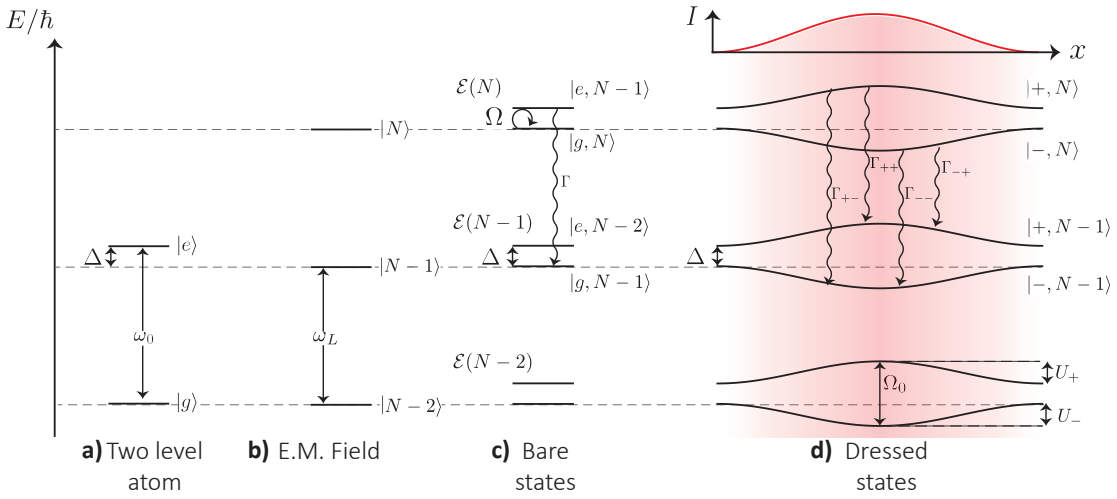

Figure 2.9. *Bare and dressed states basis* . **a)** Two-level atom. **b)** Single-mode EM field detuned by Δ to the atomic transition. **c)** In the bare state picture the atom undergoes Rabi oscillations (circular arrow) until spontaneous decay takes place (wavy line). **d)** In the dressed state picture, an atom remains in its initial state until one of the four allowed decays occurs (Γ_{ij}). When the intensity of EM field is spatially dependent (illustrated in the upper plot) the AC-Stark shift creates an attractive or repulsive potential depending on the internal state.

$$\hat{\mathbf{H}} = \hat{\mathbf{H}}_{\mathrm{A}} + \hat{\mathbf{H}}_{\mathrm{L}} + \hat{\mathbf{H}}_{\mathrm{A\text{-}L}}, \tag{2.1a}$$

$$\hat{\mathbf{H}}_{\mathrm{A}} = \hbar\omega_0 \left|e\right\rangle \left\langle e\right|, \tag{2.1b}$$

$$\hat{\mathbf{H}}_{\mathrm{L}} = \hbar\omega_L \left(\hat{a}^\dagger \hat{a}\right) \tag{2.1c}$$

$$\hat{\mathbf{H}}_{\mathrm{A\text{-}L}} = -\hat{\mathbf{d}} \cdot \hat{\mathbf{E}} \underset{\mathrm{RWA}}{=} \frac{\hbar\Omega_0}{2}\left(\hat{\sigma}^\dagger \hat{a} + \hat{\sigma}\hat{a}^\dagger\right). \tag{2.1d}$$

$\hat{\mathbf{H}}_{\mathrm{A}}$ represents the energy of the atom in free space, $\hat{\mathbf{H}}_{\mathrm{L}}$ is the energy contained in the electromagnetic field where $\hat{a}^\dagger$ and $\hat{a}$ are the rising and lowering operators for the field. The last term $\hat{\mathbf{H}}_{\mathrm{A\text{-}L}}$ represents the atom-light coupling where $\hat{\mathbf{d}}$ is the dipole operator, $\hat{\mathbf{E}} = \mathbf{E}_0\hat{a} + \mathbf{E}_0^*\hat{a}^\dagger$ is the electric field, $\hat{\sigma} = \left|g\right\rangle\left\langle e\right|$ is the atomic lowering operator and Ω_0 is the resonant Rabi frequency that characterizes the strength of the interaction.

For a linearly polarized electric field, the resonant Rabi frequency Ω_0 can be written as [63, 71]:

$$\Omega_0(\mathbf{r})^2 = \left(\frac{2\sqrt{N}\mathbf{d}\cdot\mathbf{E}_0}{\hbar}\right)^2 = \frac{6\pi c^2\Gamma}{\hbar\omega_{\mathrm{L}}^3} I(\mathbf{r}), \tag{2.2}$$

where $I(\mathbf{r})$ is the intensity of the light field and Γ the atomic natural decay rate.

Due to the atom-light coupling via $\hat{\mathbf{H}}_{\mathrm{A\text{-}L}}$ in Eq. (2.1), the bare states $\left|g, N\right\rangle, \left|e, N-1\right\rangle$ are no longer the energy eigenstates of the system. To find the new energy eigenbasis, we diagonalize the Hamiltonian in

Eq. (2.1), which spanned on the bare state basis has a matrix form

$$\hat{\mathbf{H}} = \hbar \begin{bmatrix} N\omega_L & \frac{\Omega_0}{2} \\ \frac{\Omega_0}{2} & N\omega_L - \Delta \end{bmatrix}.$$

The new eigenstates of $\hat{\mathbf{H}}$ are the so-called *dressed states*

$$|+, N\rangle = \sin\theta\,|g, N\rangle + \cos\theta\,|e, N-1\rangle\,, \tag{2.3a}$$
$$|-, N\rangle = \cos\theta\,|g, N\rangle - \sin\theta\,|e, N-1\rangle\,. \tag{2.3b}$$

With their respective eigenenergies

$$E_\pm = N\hbar\omega_L - \frac{\hbar}{2}\Delta \pm \frac{\hbar}{2}\Omega,$$

where the mixing angle is defined by

$$\tan 2\theta = -\frac{\Omega_0}{\Delta}, \quad 0 \le \theta \le \pi,$$

and $\Omega = \sqrt{\Delta^2 + \Omega_0^2}$ is the generalized Rabi frequency.

Spontaneous emission

Photon absorption and spontaneous emission are one of the most basic processes in atom-light interaction, and it will be one of the central parts in this work. It is meaningful to understand how this process can be described from the perspective of the bare and dressed states basis.

In the bare state basis. When an atom interacts with an electromagnetic field, it undergoes Rabi oscillations between $|g, N\rangle$ and $|e, N-1\rangle$. Such oscillations can be understood as a coherent absorption of a photon followed by a stimulated emission into the same mode [71]. When spontaneous emission occurs, a photon is removed from the field and emitted into free space. This is a transition from $|e, N-1\rangle$ to $|g, N-1\rangle$ (see Fig. 2.9c). A spontaneous emission of a photon occurs necessarily from the excited to ground state, i.e. transitions like $|g, N-1\rangle \to |g, N-2\rangle$ are forbidden.

In the dressed stated basis. The states $|\pm, N-1\rangle$ are the eigenstates of the system, which means that in the absence of spontaneous decay any of the dressed states will remain unchanged. However, spontaneous decay is present and the dressed states decay. In this process, a photon is removed from the field and emitted into free space. However, there is an interesting difference on the allowed transitions compared with the bare state case: from the definition of the dressed states in Eq. (2.3), it is evident that both are composed by $|e, N-1\rangle$ and $|g, N\rangle$. In consequence, the four transitions $|\pm, N\rangle \to |\pm, N-1\rangle$ are possible (see Fig. 2.9d).

2.3.2 The secular approximation: steady state solution

The population of the dressed states varies over time depending on the light's frequency and intensity. The evolution of the system can be described using the density matrix formalism by solving the full

master equation for ρ projected in the dressed state basis. Solving these equations is, in general, not a simple problem. However, in the secular approximation, $\Gamma \ll \Omega$, i.e. large detunings or intense fields, it is possible to reduce the problem to a set of rate equations to describe the system [71]

$$\dot{\rho}_{++} = -\Gamma_{+-}\rho_{++} + \Gamma_{-+}\rho_{--} \ , \tag{2.4a}$$

$$\dot{\rho}_{--} = \Gamma_{+-}\rho_{++} - \Gamma_{-+}\rho_{--} \ , \tag{2.4b}$$

$$\rho_{ij} = \sum_N \langle N, j|\rho\,|N, i\rangle \ , \text{ for } i, j = -, +. \tag{2.4c}$$

Here ρ_{ij} are the reduced components of the density matrix [73] that represent the population and coherences of the corresponding dressed states. If the secular condition is fulfilled, the transition rates Γ_{ij} are proportional to the matrix elements of the atomic rising operator $\langle\hat{\sigma}^\dagger\rangle_{ij}$,

$$\Gamma_{ij} = \Gamma\left|\langle\hat{\sigma}^\dagger\rangle_{ij}\right|^2 \text{ for } i, j = -, +, \tag{2.5}$$

and the matrix elements given by

$$\langle\hat{\sigma}^\dagger\rangle_{++} = \langle +, N|\,\hat{\sigma}^\dagger\,|+, N-1\rangle = \sin\theta\cos\theta, \tag{2.6a}$$

$$\langle\hat{\sigma}^\dagger\rangle_{-+} = \langle -, N|\,\hat{\sigma}^\dagger\,|+, N-1\rangle = -\sin^2\theta, \tag{2.6b}$$

$$\langle\hat{\sigma}^\dagger\rangle_{+-} = \langle +, N|\,\hat{\sigma}^\dagger\,|-, N-1\rangle = \cos^2\theta, \tag{2.6c}$$

$$\langle\hat{\sigma}^\dagger\rangle_{--} = \langle -, N|\,\hat{\sigma}^\dagger\,|-, N-1\rangle = -\sin\theta\cos\theta. \tag{2.6d}$$

The system reaches its steady state on time scales on the order of Γ^{-1} leading to steady state populations

$$\rho^{\text{st}}_{++} = \frac{\sin^4\theta}{\cos^4\theta + \sin^4\theta}, \quad \rho^{\text{st}}_{--} = \frac{\cos^4\theta}{\cos^4\theta + \sin^4\theta}. \tag{2.7}$$

Combining Eqs. (2.5), (2.6) and (2.7), we find the photon scattering rate in the steady state associated to each transition

$$R^{ij}_{\text{sc}} = \rho^{\text{st}}_{ii}\Gamma_{ij} \text{ for } i, j = -, +. \tag{2.8}$$

It is important to keep in mind that these results are valid just for the secular approximation, the validity of this approximation relies on a fast decay of the coherence between the dressed states. The decay time must be shorter than the relevant time scales for the external dynamics of a trapped atom, only then $\rho_{\pm,\mp}$ can be completely neglected. I will come back to this point in Chap. 3.

2.3.3 A far-red detuned dipole trap for a two-level system

Now, let us consider the case of a far-red detuned light field ($\Delta < 0, \ \Gamma \ll |\Delta|$). In this case, only one term dominates in the superposition that defines the dressed states in Eqs. (2.3). This means that the dressed states are well approximated by the original bare states

$$|+, N\rangle \approx |e, N-1\rangle \ \ , \ \ |-, N\rangle \approx |g, N\rangle\,. \tag{2.9}$$

However, their energy strongly depends on the intensity of the field

$$E_+ \approx N\hbar\omega_L + \hbar\frac{\Omega_0^2(\mathbf{r})}{4|\Delta|} \quad , \quad E_- \approx N\hbar\omega_L - \Delta - \hbar\frac{\Omega_0^2(\mathbf{r})}{4|\Delta|}. \tag{2.10}$$

This means that the presence of the field is reflected only as a position-dependent AC-Stark shift. For red (negative) detuning, the energy E_- is shifted downwards as the intensity increases, creating an attractive potential U_- for $|-, N\rangle$. The opposite happens for $|+, N\rangle$ where the energy E_+ increases with the intensity creating a repulsive potential U_+ (see Fig. 2.9d),

$$U_-(\mathbf{r}) = -\hbar\frac{\Omega_0^2(\mathbf{r})}{4|\Delta|} \quad , \quad U_+(\mathbf{r}) = \hbar\frac{\Omega_0^2(\mathbf{r})}{4|\Delta|}. \tag{2.11}$$

The number of photons scattered per unit of time can be calculated using Eq. (2.8)

$$R_{\mathrm{sc}}^{++}(\mathbf{r}) = \Gamma\left(\frac{\Omega_0(\mathbf{r})}{2\Delta}\right)^6, \quad R_{\mathrm{sc}}^{+-}(\mathbf{r}) = \Gamma\left(\frac{\Omega_0(\mathbf{r})}{2\Delta}\right)^4, \tag{2.12a}$$

$$R_{\mathrm{sc}}^{-+}(\mathbf{r}) = \Gamma\left(\frac{\Omega_0(\mathbf{r})}{2\Delta}\right)^4, \quad R_{\mathrm{sc}}^{--}(\mathbf{r}) = \Gamma\left(\frac{\Omega_0(\mathbf{r})}{2\Delta}\right)^2. \tag{2.12b}$$

Even though for large detunings the dressed states look very similar to the original bare states, the scattering rates calculated above manifest a strong difference between dressed and bare states. While for the bare states the transition $|g, N\rangle \rightarrow |g, N-1\rangle$ is forbidden, for the dressed states the transition $|-, N\rangle \rightarrow |-, N-1\rangle$ is the main decay channel.

Finally, it is convenient to express the dipole potential for the ground state in Eq. (2.11) and the scattering rate in Eq. (2.12) using the value for the Rabi frequency in Eq. (2.2)

$$U_g(\mathbf{r}) \approx U_-(\mathbf{r}) = \frac{3\pi c^2\Gamma}{2\Delta\omega_0^3} I(\mathbf{r}), \tag{2.13a}$$

$$R_{\mathrm{sc}}(\mathbf{r}) \approx R_{\mathrm{sc}}^{--} = \frac{3\pi c^2\Gamma^2}{2\Delta^2\hbar\omega_0^3} I(\mathbf{r}). \tag{2.13b}$$

The role of the dipole force fluctuation

The four scattering rates in Eqs. (2.12) represent all scattered photons from the dipole trap into free space. For a far-red detuned dipole trap, an atom remains most of the time in the state $|-, N\rangle$, therefore we can just focus on the rates R_{sc}^{--} and R_{sc}^{-+}. For scattering events described by R_{sc}^{-+}, an atom is transferred from an attractive to a repulsive potential, and for the time the atom remains on the state $|+, N\rangle$, the trap exerts a repulsive force on the atom until it decays back to the attractive potential. The random fluctuation from a trapping to a repulsive force creates a diffusion of the atom's total energy that can lead to the loss of the atom. This stochastic process will be referred as the *dipole force fluctuations*. In contrast, for scattering events described by R_{sc}^{--}, an atom scatters a photon but the trapping potential remains the same, i.e. the only energy gained during this process is by photon recoil (see Fig. 2.9d).

In the special case of a far-red detuned dipole trap ($\Omega_0(\mathbf{r})/\Delta \ll 1$), from Eqs. (2.12) it follows that $R_{\mathrm{sc}}^{--} \gg R_{\mathrm{sc}}^{-+}$, i.e. most of the scattered photons do not create any dipole force fluctuation. Therefore the only source of heating is the recoil induced by the absorption and emission process.

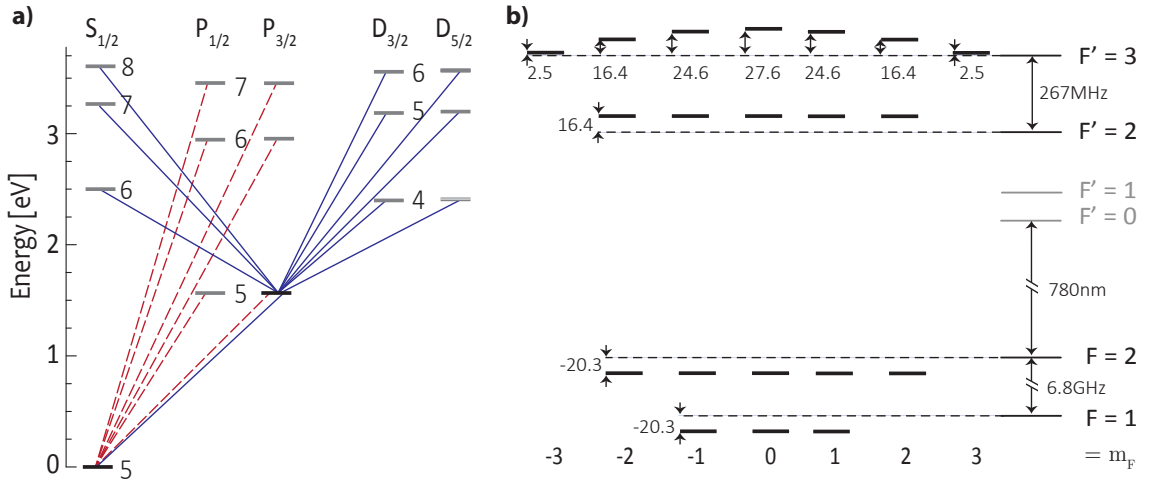

Figure 2.10. *Multilevel effect on the AC-Stark Shift.* **a)** Dipole allowed transitions used for the calculation. The red dashed-lines were used for the $5S_{1/2}$ ground state shift and the blue solid-lines for $5P_{3/2}$ excited state. **b)** The calculated AC-Stark shift for a linear π-polarized dipole trap interacting with ^{87}Rb. Only the relevant excited states are shown, the numbers in the level diagram indicate the AC-Stark shift in units of MHz/mK. For π polarization the shift does not depend on the sign of the m_F level.

2.3.4 AC-Stark shift in a multilevel system

The structure of an atom, ^{87}Rb in this case, is more complex than a simple two-level system. For a real atom, each state of the hyperfine manifold couples to every dipole-allowed transition. When the induced AC-Stark shift is much smaller than the dipole trap detuning, it is a good approximation to assume that the shift induced by the transitions are independent of each other and, therefore, the total AC-Stark shift can be calculated as the sum of all the individual contribution for each allowed transition.

The effect of the multilevel atomic structure affects differently the ground and excited states. For the hyperfine ground states of ^{87}Rb, and π-polarized light for the dipole trap, the main contributions to the AC-Stark shift are the D_1 and D_2 lines. Moreover, the AC-Stark shift for the ground state is independent of the particular m_F quantum number. Therefore, the potential for the ground state and total scattering rate can be written as [11]

$$U_g(\mathbf{r}) = -\frac{3\pi c^2\Gamma}{2\Delta_{\text{eff}}\omega_0^3} I(\tilde{\mathbf{r}}), \quad R_{\text{sc}}(\mathbf{r}) = \frac{3\pi c^2\Gamma^2}{2\Delta_{\text{eff}}^2\omega_0^3\hbar} I(\mathbf{r}), \quad \Delta_{\text{eff}} = \frac{1}{3}\left(\frac{2}{\Delta_{D_2}} + \frac{1}{\Delta_{D_1}}\right)$$

where Δ_{D_1} and Δ_{D_2} are the detunings from the D_1 and D_2 lines and Δ_{eff} is an effective detuning that accounts for the contribution of both lines.

For the manifold in the excited state $5P_{3/2}$, each of the m_F levels is shifted differently. To estimate the AC-Stark shift for each m_F level for $F' = 2, 3$, we follow Ref. [74]. The calculated AC-Stark shift induced by π-polarized light is shown in Fig. 2.10 as well as the transitions used in the calculation. Only the states $F' = 2, 3$ are shown since these are relevant levels for the discussion in the following chapters.

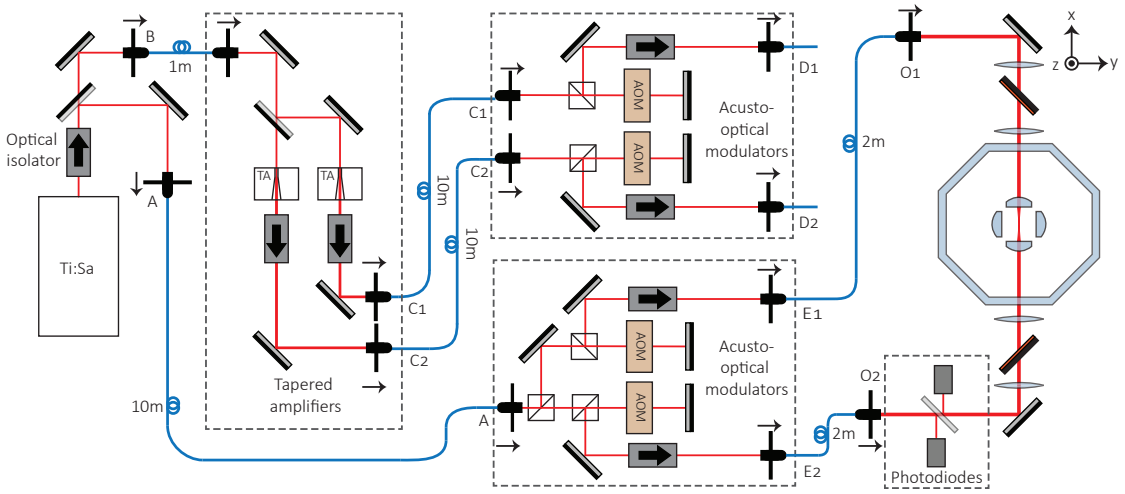

Figure 2.11. *Simplified dipole trap scheme.* Details such as wave plates, lenses and other optical elements are omitted for the sake of simplicity.

2.3.5 Experimental implementation

One of the most common ways to implement an array of optical potentials is by a 1D standing-wave dipole trap. In our system this is created by two counter-propagating linearly-polarized Gaussian beams. The intensity of the created interference pattern is described by

$$I(\mathbf{r}) = I_{\max}\frac{w_0^2}{w^2(x)}\exp\left[-\frac{2\left(y^2+z^2\right)}{w^2(x)}\right]\cos^2(k_{\mathrm{DT}}x)$$

$$w^2(x) = w_0^2\left[1+\left(\frac{x}{x_R}\right)^2\right], \quad x_R = \frac{\pi w_0^2}{\lambda_{\mathrm{DT}}}, \quad I_{\max} = \frac{8P}{w_0^2\pi},$$

where P is the power of each beam (here assumed to be equal), $w(x)$ is the spot size at position x, w_0 is the beam waist, x_R is the Rayleigh length, λ_{DT} and k_{DT} are the wavelength and wave vector and $I_{\max}$ is the peak intensity. This creates trapping potentials proportional to the intensity

$$U(\mathbf{r}) = U_0\frac{w_0^2}{w^2(x)}\exp\left[-\frac{2\left(y^2+z^2\right)}{w^2(x)}\right]\cos^2(k_{\mathrm{DT}}x)$$

$$U_0 = \frac{3\pi c^2 I_{\max}\Gamma}{2\omega_0^3\Delta_{\mathrm{eff}}}, \quad \omega_{\mathrm{axial}} = k_{\mathrm{DT}}\sqrt{\frac{2U_0}{m}} \quad \omega_{\mathrm{radial}} = 2\sqrt{\frac{U_0}{mw_0^2}}$$

where U_0 is the maximum trap depth, ω_{axial} and ω_{radial} are the harmonic oscillation frequencies at the bottom of the trap in the respective directions.

Laser delivery system

To create potentials deep enough to trap neutral atoms, we use a Titanium-Sapphire (Ti:Sa) laser that delivers up to 700 mW at 860 nm from which 80% can be coupled into single-mode polarization-maintaining fibers. The beam is divided into two using a variable beam splitter, from where it is directed into two different fibers as shown in Fig. 2.11. The power of the laser is used in different ways depending on the experiment.

Path I. (A-E-O)[15]:

- A fraction of the Ti:Sa power is coupled into fiber (A). The power can be varied using a variable beam splitter.
- After the optical fiber (A), the beam is separated into two parts, each of them is shifted +160MHz using a pair of AOMs in double pass configuration and the light is then coupled to the fibers (E). With this configuration, a maximum of 130 mW can be transmitted at the end of the fibers (E).
- After the output couplers (O), the light is sent to the experimental chamber.

Path II. (B-C-D-O):

- Using the variable beam splitter, 60 mW of power is transmitted at the output of the optical fiber (B).
- After the optical fiber (B), the light is split into two beams and sent through two tapered amplifiers. Each beam is amplified to a maximum of 2W from which, after the optical elements, 30% of the light can be coupled into the optical fibers (C).
- After the fibers (C), each beam is sent through an AOM which shifts the frequency by -160MHz and then are coupled into the fibers (D). With this configuration, a maximum of 180 mW can be transmitted at the end of the fibers (D).
- If this path is used, the fibers (E) and (D) can be easily interchanged without affecting the alignment after the point (O).

For most of the experiments path I is used since it provides better stability. If a high power is required path II is used.

Dipole trap parameters

After the output couplers (O), the beam has a waist of 0.45 mm and is linearly polarized along the z axis. A beam sampler reflects 10% of the light to a pair of amplified photo-diodes (PD). The PDs, together with the AOMs are used to stabilize the dipole trap intensity by a closed feedback loop using a proportional-integral servo circuit. The power is adjusted by adding an offset voltage to the PDs using the computer control system.

The light transmitted after the pickup plates is sent to the experimental chamber, where it is focused down by the set of aspheric lenses mounted inside the vacuum system. An extra pair of lenses is used to compensate for chromatic aberrations. The physical parameters of the 1D standing wave are summarized in Table 2.1.

[15] The letters A-E indicate the label of the optical fibers used in the path shown in Fig. 2.11, and O indicates the final output.

Table 2.1. One-dimensional standing wave dipole-trap parameters

Quantity	Symbol	Calculated value
Wavelength	λ_{DT}	860 nm
Waist	w_0	5 μm
Rayleigh length	x_{R}	91 μm
Trap depth	U_0	$41.6\,\mu\mathrm{K} \times P\,[\mathrm{mW}]$
Scattering rate	R_{sc}	$1\mathrm{s}^{-1} \times P\,[\mathrm{mW}]$
Axial frequency	ω_{axial}	$2\pi \times 104\ \mathrm{kHz} \times P\,[\mathrm{mW}]^{1/2}$
Radial frequency	ω_{radial}	$2\pi \times 4\ \mathrm{kHz} \times P\,[\mathrm{mW}]^{1/2}$

Although all the experiments mentioned in this work are performed using only the standing wave in the x direction, a second standing wave can be created along the y direction in exactly the same way (not shown in the figure for simplicity). Appendix B shows the configuration used to create a two-dimensional lattice when a high power in the beams is not required.

Experimental measurements

Lifetime measurement. To estimate the lifetime of the atoms in the trap, a few atoms are loaded from the MOT into the dipole trap using a power of 35 mW for each arm. Then 30 images are taken with an exposure time of 100 ms and separated in time by one second. The images are later used to estimate the number of atoms in the dipole trap (details regarding atom counting are explained in Sec. 2.4.4). This measurement was done for two different configurations of the trapping light.

- *Configuration I.* The wavelength of the Ti:Sa laser is adjusted at 880 nm and sent through the path I creating a trap depth of 1.2 mK.
- *Configuration II.* The wavelength of the Ti:Sa laser is adjusted at 860 nm and sent through path II generating a trap depth of 1.5 mK.

Fig. 2.12a shows the survival probability of the atoms trapped the dipole trap for both configurations. From an exponential fit to the measured data, we estimate a lifetime of 49.5 ± 3.6 s for the configuration I and 24.8 ± 0.8 s for configuration II.

AC-Stark shift measurement. To experimentally measure the AC-Stark shift induced by the dipole trap with a wavelength of 860 nm [74], a few atoms are loaded in the standing wave and pumped to the state $F = 2, m'_F = -2$. The power of one arm of the trap is fixed at $P_1 = 18$ mW and the other is adiabatically set to four different values[16] P_2 =21, 41, 84, 127 mW. Then a weak illumination beam, near-resonant to the transition $F = 2, m'_F = -2 \rightarrow F = 3, m'_F = -3$ with an intensity of $\sim 0.1 I_{\mathrm{sat}}$, is turned on for 0.1 ms using different frequencies for each value of P_2. The scattered fluorescence is recorded by the EMCCD camera. By fitting a Lorentzian curve to the recorded fluorescence spectrum, we obtain the

[16] Only one arm is changed in order minimize the intensity variation at the bottom of the trap, by not creating a full-contrast interference pattern for the standing wave.

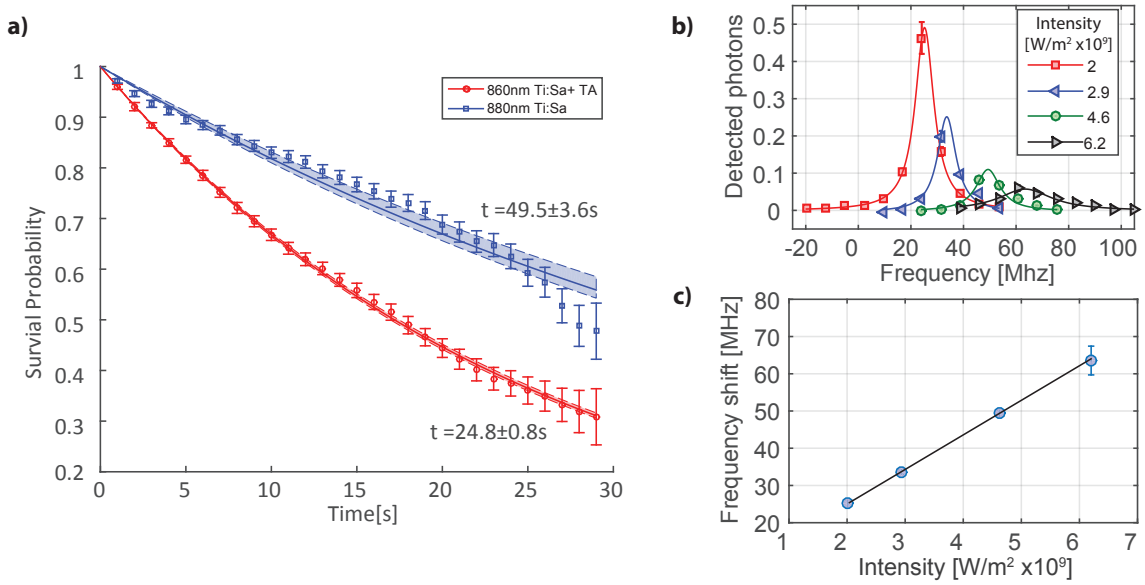

Figure 2.12. *Atomic lifetime in the dipole trap and AC-Stark shift.* **a)** Two sets of data are shown, the blue squares were measured using the Ti:Sa laser at 880 nm with 35 mW for each beam (trap depth of 1.2mK). Red circles using the Ti:Sa at 860 nm + tapered amplifiers with the same power for each beam, (trap depth = 1.5mK). The lines are a fit to an exponential function and the shaded area represents a 95% confidence interval. **b)** AC-Stark shift spectrum for 4 different powers of the dipole trap, the values in the legend corresponds to the respective dipole trap intensity. **c)** Linear fit to frequency shift obtained for different intensities in the dipole trap. For **b** and **c** the error bars represent one standard deviation obtained by bootstrap resampling.

resonance frequency of the AC-Stark shifted atoms for each value of P_2 (see Fig. 2.12b). From the fit, we estimate an AC-Stark shift of $2\pi \times 9.2 \pm 0.1 \times 10^9$ MHz W^{-1} m^2, where we have assumed a waist of 5 µm for the dipole trap[17]. This value for the AC-Stark shift is close to a theoretical expectation of $2\pi \times 9 \times 10^9$ MHz W^{-1} m^2 calculated following Ref. [74].

2.4 Fast detection of individual atoms by fluorescence imaging

To study and manipulate neutral atoms trapped in an optical lattice, it is necessary to first obtain basic information about the atomic ensemble, for instance, the number of atoms in the trap and their position in the lattice. One way to retrieve such information is by illuminating the atoms with near-resonant light in a molasses configuration in order to create an image using the EMCCD camera. Then by analyzing the image, extract the desired information. This imaging technique has already been implemented in our research group [66, 75], as well as in other laboratories [21, 22]. In such systems, atoms are illuminated for $\sim$ 1 s using a low intensity molasses in order to minimize hopping of the atoms to adjacent lattice sites. With this technique, it is possible to determine the position of the atoms in the lattice with high accuracy. However, it is desirable to reduce the image acquisition time, for example to implement fast feedback loops. The exposure time, which is limited by either a low detection efficiency (<1%) [66, 75]

[17] In Chap. 5, a measurement of the trapping frequency leads to a smaller waist of 4.75 µm, using this value for the dipole trap beams we obtain an AC-Stark shift of $2\pi \times 8.1 \pm 0.1 \times 10^9$ MHz W^{-1} m^2 which is also close to the theoretical expectation.

or by atom hopping in a shallow trap (U_0 ~0.3 mK) [21, 22, 75], can be reduced by using a large NA objective to image atoms in a deep trap.

This section presents the experimental characterization of the fast detection of individual atoms in a tightly-focused 1D standing wave. We start with a brief introduction to the position determination problem (Sec. 2.4.1), a description of the imaging setup (Sec. 2.4.2), and a detailed characterization of EMCCD camera (Sec. 2.4.3). Then we analyze the quality of the imaging system and determine the line spread function of the optical system (Secs. 2.4.4 and 2.4.5). Finally, the line spread function is used to determine the position of the atoms in the lattice and the accuracy of the position determination is quantified (Sec.2.4.6).

2.4.1 Localization of single atoms in an optical lattice

The position of an atom in an optical lattice can be determined using fluorescence images. The accuracy of this position depends on the quality of the image generated, which can be deteriorated by different mechanisms. For example: optical diffraction by the imaging optics, which leads to the formation of an Airy pattern at the image plane that blurs the image and limits the optical resolution; the finite size of the pixels on the CCD, which creates a spatial filter that averages out the small structures of an image; and image contamination by stray light and electronic noise during the readout process.

The localization precision is, therefore, limited by the characteristics of the imaging system. If the noise sources are minimized and the effect of the CCD is negligible, the generated image will still be limited by light diffraction due to the finite aperture of the lens used to collect the atomic fluorescence. However, it has been shown that the position determination of atoms in a 1D lattice can surpass the diffraction limit [38, 76]. Furthermore, the localization precision of a single atom in a one-dimensional lattice can be estimated by [76, 77]

$$(\Delta x)^2 = \frac{\mathrm{RMS}_{\mathrm{PSF}}^2 + \Delta_p^2/12}{N} + \frac{4\sqrt{\pi}\mathrm{RMS}_{\mathrm{PSF}}^3\sigma_b^2 n_{\mathrm{v}}}{\Delta_p N^2}, \tag{2.14}$$

where $\mathrm{RMS}_{\mathrm{PSF}}$ is the width of the Gaussian function that best approximates the point spread function, Δ_p is the size of the pixel in the object plane, σ_b is the RMS background noise, n_{V} is number of vertically integrated pixels and N is the mean number of detected photons.

In the remaining part of this chapter, we will show that by choosing an adequate magnification of the optical system, reducing the noise sources, and using adequate parameters for the illumination light, the position of atoms trapped in a one-dimensional lattice can be determined with an accuracy of a few tens of nanometers from an image acquired in only 20 ms.

2.4.2 Imaging optics

The set of aspheric lenses described in Sec. 2.1.2 is used to collect light from the MOT and to detect individual atoms in the dipole trap (see in Fig. 2.13a). A pair of aspheric lenses (3 and 4) is used to create the standing wave dipole trap while the other pair (lenses 1 and 2) is used to collect the atomic fluorescence. To guarantee a diffraction limited performance of the optical system, the light collected with lens 1 is slightly divergent when leaving the glass cell (see Sec. 2.1.2) then it is collimated with

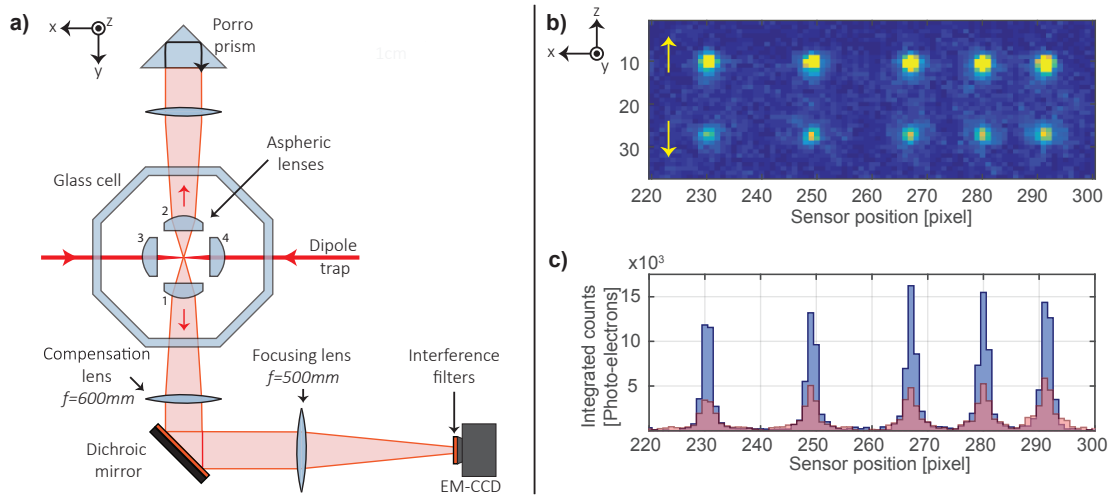

Figure 2.13. *Single atom imaging.* **a)** Sketch of the imaging optics. **b)** Image taken with the EMCCD camera. The upper row of atoms is the "normal" image, and the lower row is the image obtained using the reflected light. The reflected image is mirrored along the x axis as illustrated by the arrows. **c)** Integrated number of counts along the vertical direction for the normal and reflected images.

a compensation lens (f=600mm) and finally focused on the EMCCD camera using a lens with a focal length of 500 mm. A pair of interference filters[18] are placed in front of the camera to reduce background light. The light collected with lens 2 is reflected back using a Porro prism[19] and then focused on the EMCCD sensor detecting up to 50% more light. Fig. 2.13b shows an example of the direct and the reflected image. The difference in amplitude between two images is expected due to additional losses originating from the retroreflected path ($\sim$ 20%); furthermore, while in the direct imaging path lens 1 images a point source, in the reflected path lens 1 images an Airy disk (due to diffraction in lens 2), which contains at most 85% of the light in the central peak.

The Porro prism was aligned in all directions such that the position of the reflected image coincides with the position of the original image. In Fig. (2.13)b both signals appear separated by a few pixels, this was done only for illustration purposes. From now on, we will refer to the image created by lens 1 (with no prism) as the "direct" image, and the combination of the reflected and the direct signal as the "combined" image.

One must note that the light reflected by the Porro prism is mirrored along the x axis (illustrated by the arrows in Fig. 2.13b). The atoms move along the radial direction (along z and y) over distances larger than the illumination wavelength, therefore any possible interference effects are not visible since they are averaged out.

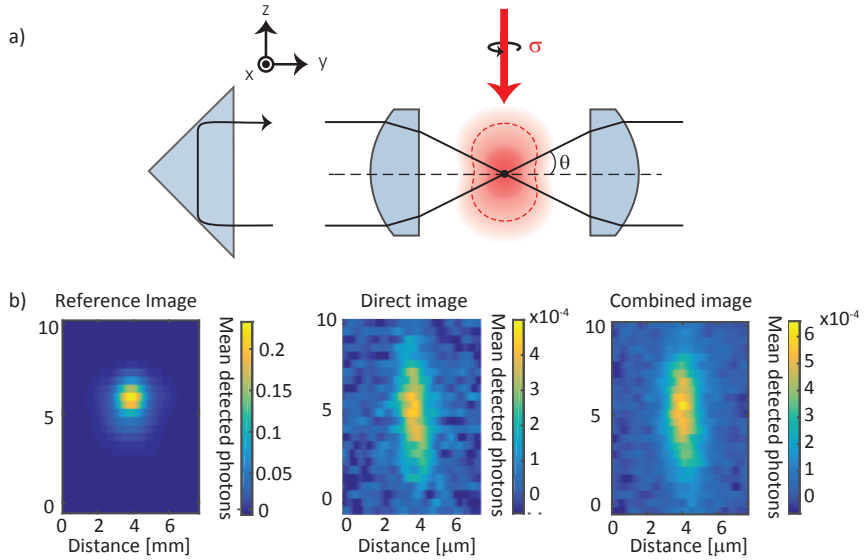

Figure 2.14. *Collection efficiency.* **a)** Dipole emission for σ light illumination. **b)** Stacking result for reference images (left), fluorescence collected with only one lens (middle), and fluorescence collected using also the Porro prism (right).

Measuring the collection efficiency

All the information that we obtain from the atoms trapped in the lattice comes from the photons detected by the EMCCD camera. For a quantitative understanding of the photon scattering process, it is necessary to estimate the total number of scattered photons from the small fraction that is detected. It is possible measure the detection efficiency by illuminating the atoms with an intense resonant beam as illustrated in Fig. 2.14a, and then compare the number of detected photons with a theoretical expectation.

When an atom is illuminated with polarized light, the photon emission is described by a dipole pattern [78], which needs to be taken into account to correctly estimate the number of detected photons. For example, illuminating an atom with σ polarized light reduces slightly the number of collected photons in comparison with the spherical emission case (see Fig. 2.14a). The percentage of photons detected when illuminating with σ polarized light, i.e. the Collection Efficiency (CE), is given by the integration of the dipole pattern over the solid angle subtended by the lens.

$$\mathrm{CE}_\sigma = \int_{\theta=\theta_0}^{\theta=\theta_f} \int_{\phi=-\phi_0}^{\phi=\phi_0} \frac{3}{8\pi} \left(\cos^2\theta + 1\right) \sin\theta d\theta d\phi \tag{2.15}$$

$$\phi_0 = \arcsin\left[\sqrt{\frac{\mathrm{NA}^2}{\sin^2\theta} - \frac{1}{\tan^2\theta}}\right], \quad \theta_i = \frac{\pi}{2} - \arcsin(\mathrm{NA}), \quad \theta_f = \frac{\pi}{2} + \arcsin(\mathrm{NA}).$$

[18] Semrock, 780 nm MaxLine ® laser clean-up filter.

[19] Porro prism from Precision Optical, a clear aperture diameter of 0.5", 180° beam deviation < 2 arc seconds and AR coating reflecting approximately 6.2% at 780 nm. We have observed that the edge quality of the prism plays an important role. In our first attempt, we have used a corner cube retro-reflector but it was not possible to observe the reflected image. The problem was solved by using a Porro prism with knife edge quality.

From a separate measurement (see Sec. 2.4.5), we estimate that the aspheric lens used to collect the atomic fluorescence has a NA= 0.43, thus it subtends 4.9% of the total solid angle. Using the measured NA, Eq. (2.15) leads to a $CE_\sigma = 3.8\%$ for a single lens. Some of the collected light is lost due to the optical elements used to guide the collected fluorescence and due to the quantum efficiency of the camera. Taking into account all possible losses[20], we expect to detect 51 ± 13% of the collected photons, leading to a theoretical detection efficiency of 1.9 ± 0.5% of the scattered photons.

To experimentally measure the detection efficiency, a few atoms are loaded in the dipole trap and an image is taken. The trap is adiabatically reduced to 200 μK and then it is switched off. A strong resonant beam is turned on for $t_{\text{probe}} = 10\,\mu\text{s}$ while the camera is exposing. The resonant beam propagates along the z direction, with an intensity of 21 I_{sat} and is resonant with the cycling transition $F = 2, m_F = -2 \rightarrow F' = 3, m_F = -3$. At the same time, we use a strong repumper resonant with the $F = 1 \rightarrow F' = 1$ transition and an intensity of 14 I_{sat}. We assume that the atom scatters photons like an ideal two-level system at a rate

$$R_{\text{sc}} = \left(\frac{\Gamma}{2}\right) \frac{s}{1 + 4\,(\Delta/\Gamma)^2 + s}, \tag{2.16}$$

where s is the saturation parameter and Δ the detuning of the illumination light from the atomic resonance. Assuming an uncertainty of 10% on the power of the resonant beam and $\pm 2\pi \times 2.5$ MHz on its frequency, using Eq. (2.16) we estimate that the number of emitted photons is $R_{\text{sc}} t_{\text{probe}} \approx 182^{+0.8}_{-20}$. During the illumination time, an atom displaces a distance $d \approx \frac{\hbar k \Gamma}{4m} t^2 < 5\,\mu\text{m}$ and remains within the field of view of the camera.

The detection efficiency is measured for the direct image (without the Porro prism) and for the combined image (with the Porro prism). For the direct image we obtain a detection efficiency of $1.97^{+0.11}_{-0.25}\%$, which agrees with the theoretical expectation, and for the combined image we obtain[21] $2.87^{+0.07}_{-0.32}\%$. To obtain the CE of the direct image, we used 3300 single and for the combined image we used 10^4 atoms. To confirm that the atom did not move a distance bigger than the field of view during the illumination process, the position of the atoms in the reference image is determined[22] and used to stack all images containing the signal of just a few photons of the detected fluorescence. With this procedure, it is possible to obtain an image of the atoms as they fall while being illuminated (see Fig. 2.14)b.

2.4.3 EMCCD camera

To detect the weak atomic fluorescence, we use an EMCCD camera from Andor technology, model Ixon 3 DU-897-BV with 512×512 pixels of 16 μm × 16 μm and a quantum efficiency of ~ 75% for a wavelength of 780 nm. The EMCCD works as a usual CCD with the addition of an Electronic Multiplication (EM) gain register before the readout process (for more details regarding the operation of an EMCCD see Refs. [79, 80]). Due to its low electronic noise, it is capable of single photon detection when operated at high EM gain, making it ideal for single atom imaging. This section presents the characterization of the EMCCD as well as the determination of the mean number of counts detected per photon.

[20] 6 mirrors R=99.4 ± 0.4%, 3 lenses T=99.25 ± 0.25%, 1 glass cell window T=97 ± 1%, camera QE=75 ± 5%, 2 Interference filters T = 96.5 ± 1.5%, 1 Dichroic B.S. R = 95.0 ± 2.5%. Light collected in the cropped ROI 93.5 ± 3.5%.

[21] The error was estimated using Gaussian error propagation accounting for the camera photon to electron conversion error (see Sec. 2.4.3) as well as power and frequency estimations, the statistical error in the measurement was estimated by bootstrap resampling.

[22] Details regarding the position determination are presented in Sec. 2.4.6.

Electronic noise characteristics

In a conventional CCD, even when no photoelectrons are generated on the sensor, undesired charges are created during the readout process, mostly due to the conversion from the analog to a digital signal. The number of generated electrons during this process is described by a normal distribution [80]

$$P_{\text{read}}(n, \mu, \sigma) = \frac{1}{\sqrt{2\pi\sigma}} \exp\left(-\frac{(n-\mu)^2}{2\sigma^2}\right) \tag{2.17}$$

where μ is an electronic offset added to the output signal and σ is the width of the noise distribution.

To overcome such readout noise, in an EMCCD the signal is amplified before the readout process. To this end, the charges are shifted through an EM gain registers where a charge generates a second one with a small probability p_0 by impact ionization (usually $p_0 \approx 1\%$). Even though the probability is quite small, after several hundreds of amplifications steps (536 for our system [79]) this results in a large gain.

One disadvantage of the EM process is that for a single photoelectron on the CCD, the number of charges generated after the EM process is described in a probabilistic way. If a photoelectron enters the gain register, the resulting number of electrons n after the amplification process is described by an exponential distribution [80, 81]

$$P_{\text{EM}}(\gamma, n) = \frac{1}{\gamma} \exp(-n/\gamma)\, \eta(n) \tag{2.18}$$

where $\eta(n)$ is the step function, $\gamma = (1 + p_0)^N$, N is the number of amplification stages, and γ can be interpreted as the mean number of generated electrons per detected photon.

Besides the readout noise, there are other sources of noise that originate in different parts of the image transfer process. These are:

- *Clock induced charges (CIC):* charges that originate on the CCD when the pixels are shifted. These charges undergo amplification on the EM register.
- *Dark current:* thermally generated charges in the sensor whose number is proportional to the exposure time. To reduce these charges, we operate the camera at -80°C for short exposure times (5-100 ms). These charges undergo full EM amplification; however, compared to other noise sources these charges are negligible.
- *Serial clock-induced charges (sCIC):* charges generated by pixel shifting in the gain register, therefore they do not undergo full amplification. An electron generated in the kth stage undergoes just $(N - k)$ amplification steps. Assuming an equal probability for an electron to be generated at any stage, the total number of generated electrons due to serial CIC is [80]

  $$P_{\text{sCIC}}(n) = \sum_{k=1}^{N} \frac{1}{\gamma_{N-k}} \exp(-n/\gamma_{N-k})\, \eta(n) \tag{2.19}$$

  where $\gamma_{N-k} = (1 + p_0)^{N-k}$.
- *Non-uniform photo response:* due to manufacturing imperfections such as pixel geometry, the photo-response can vary at different positions on the sensor, these can be fixed by pre-calibrating the sensor.

Table 2.2. Low noise camera settings

Acquisition Mode:	Kinetics
Trigger Mode:	External Start
Vertical Shift Speed [μs]:	0.5
Pixel Readout Rate [MHz]:	10
Baseline Clamp:	ON
Clock Amplitude:	2
EM Gain level:	1000
Pre-Amplifier Gain:	×5

When a low number of photoelectrons are generated on the sensor (less than one per pixel), the number of charges after the entire multiplication and readout is a combination of the processes described above. Therefore, the probability to generate n counts can be written as [80]

$$P(n) = (1 - a - Nb)\, P_{\text{read}}(n, \mu, \sigma) + \left[aP_{\text{EM}}(\gamma, n) + bP_{\text{sCIC}}(\gamma, n)\right] * P_{\text{read}}(n, \mu, \sigma), \tag{2.20}$$

where a and b are the probabilities for the generation of CIC and sCIC respectively. One must be aware that the last two terms corresponding to the sCIC and CIC are convoluted with the readout noise.

The camera can be operated in a different variety of modes according to the specific application. In our case, we are interested on detecting a few photons in time intervals of 20 ms. We have observed that the CICs strongly depend on the trigger mode the camera is operated (see Ref. [82]). The trigger mode that produces the lowest contamination by CICs is the *external start* mode. In this mode, once the camera receives a trigger it begins to take a given number of pictures with a fixed exposure time in well defined time periods. This limits the experiment flexibility since the time between exposures cannot be changed and consequently, the experimental sequences need to be adapted to such constraints. Nevertheless, these settings are preferred since for most experiments presented in this thesis, we detect only a few tens of photons per atom (see Chap. 4). For this reason, the camera is operated using the settings that we have found to create the lowest number of CIC which are shown in Table 2.2 (for more details see Ref. [82]).

Camera response and noise characterization

A photon detected by the EMCCD camera is transformed (after the EM process) into a given number of charges in a probabilistic way. This process is characterized by the mean number of electrons generated per photon, i.e. the value γ in Eq. (2.21). To experimentally measure this value, it is necessary to generate a very small number of charges on the sensor, which means either detecting single photons or no light at all. Since the CIC cannot be distinguished from charges generated by photons hitting the CCD, it is enough to model the camera response using "dark" images, i.e., images where no light hits the CCD. Using such dark images, one can also characterize the noise of the readout process. To this end, use 2×10^3 dark images to create a histogram of the number of generated charges per pixel, which is shown

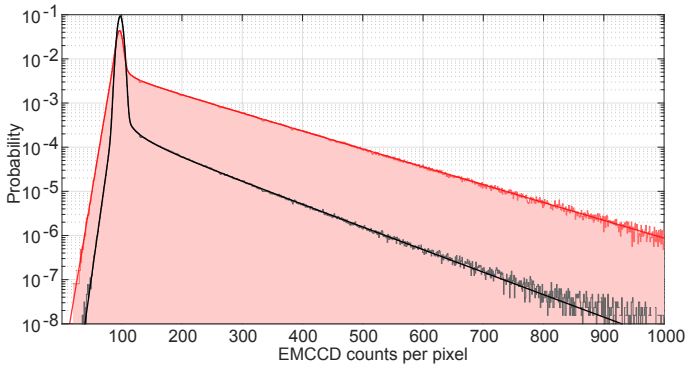

Figure 2.15. *Noise histograms*. Normalized histogram for the detected counts per pixel using the EMCCD camera for dark images (black lines and transparent area) and stray light from illumination (red lines and shaded area). The dark lines are fits to Eq. (2.21).

in Fig. 2.15 using a total of $\sim 6 \times 10^8$ individual pixels. To record the histogram, we use the settings listed in Table. 2.2 and an exposure time of 20 ms.

The count histogram shown Fig. 2.15 has three characteristic regions: a dominant Gaussian peak, which comes from the readout process; an exponential tail to the right side, which originates from the EM gain process; and we also observe an exponential tail to the left side, which is not included in Eq. (2.20). We attribute the latter effect to a non-perfect baseline (or bias level), which is an electronic offset added to the output signal from the EMCCD sensor to ensure that the displayed signal level is always a positive number of counts. We include the small effect of this tail to the noise description in Eq. (2.20) by adding an extra term, i.e.,

$$P(n) = (1 - a - Nb - c)\, P_{\text{read}}(n, \mu, \sigma) + \left[a P_{\text{EM}}(\gamma, n) + b P_{\text{sCIC}}(\gamma, n) + c P_{\text{c}}(\gamma', n)\right] * P_{\text{read}}(n, \mu, \sigma) \tag{2.21}$$

where, $P_{\text{c}}(\gamma', n) = \gamma'^{-1} \exp(n/\gamma')\eta(-n)$. From a fit of Eq. (2.21) to the histogram in Fig. 2.15, we obtain a value of $\gamma = 87 \pm 2$ electrons generated per detected photon and a probability to generate CIC of 0.012 ± 0.001 per pixel.

In addition to the electronic noise sources intrinsic to the camera, additional contamination occurs due to variation background light during the illumination process [76]. To characterize the contamination due to the background light, we proceed in the same way as described before, but now using images acquired in the presence of illumination light (with parameters listed below). The histogram for the detected counts per pixel is shown in Fig. 2.15. From the histogram, we obtain the probability to generate a photoelectron per pixel $P_{\text{BG}} = 0.49 \pm 0.01$, and a standard deviation (RMS of background noise) $\sigma_b = 0.98\ \text{ph.e}^-/\sqrt{\text{pixel}}$.

2.4.4 Position-dependent AC - Stark shift: atom counting using the EMCCD

The imaging system depicted in Fig.2.13a is used to generate images of atoms trapped in the optical lattice with a trap depth of 1.5 mK. To this end, the atoms are illuminated with an optical molasses for 20 ms, typical powers for the molasses light are 40 µW for the x and y direction and 350 µW for the z direction. The light is near-resonant to the $F = 2 \rightarrow F' = 3$ transition with a free space detuning of -4 Γ. The repumping laser propagates along the z direction with a power of 30 µW and is resonant with the $F = 1 \rightarrow F' = 1$ transition. A typical image of atoms in the dipole trap acquired with these settings is shown in Fig. 2.16a.

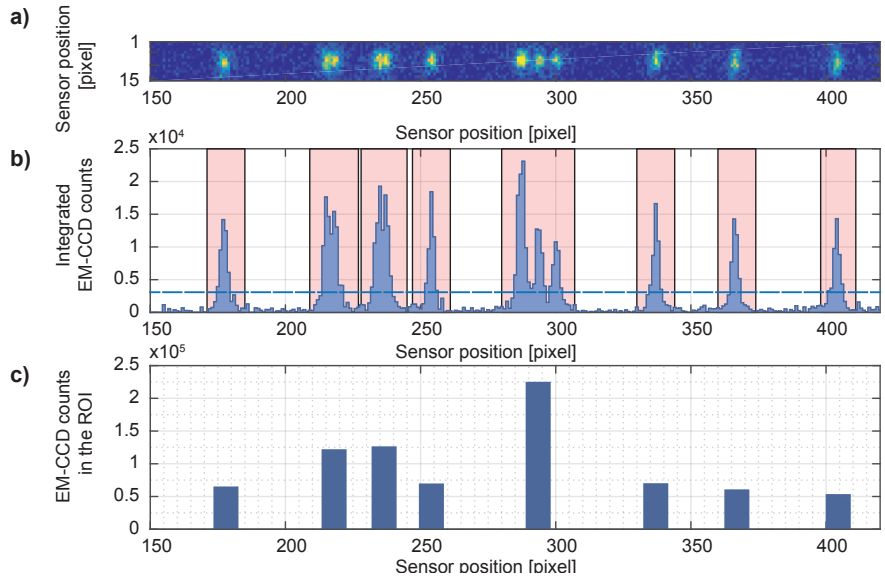

Figure 2.16. *Determining the region of interest.* **a)** Image acquired using the EMCCD with an exposure time of 20ms. The image also includes the reflected light using the Porro prism. **b)** Integrated profiles. The readout offset has been already subtracted. The horizontal dashed line is the initial threshold and the shaded areas represent the regions of interest. **c)** Total number of counts in each region of interest.

The atoms are trapped in a tightly focused standing wave dipole trap which has a waist of 5 µm and a Rayleigh length of 90 µm. This creates a significant variation of the AC-stark shift at different positions along the axial direction. To give a quantitative approximation, one can assume that an atom scatters photons like an ideal two-level system. For a trap depth of 1.5 mK, Eq. (2.16) indicates that due to the different AC-Stark shift, the scattering rate at a distance of one Rayleigh length is approximately two times larger than the rate at the center of the trap.

In addition to this AC-Stark shift, other physical constraints such as a limited field of view, clipping on mirrors, the influence of interference filters, the finite aplanatic region, imperfections in the sensor [76], also create a dependence of the number of detected photons at different positions on the sensor. Such effects must be considered for a correct estimation of number and position of atoms.

Defining the region of interest

To count the number of atoms in the standing wave, it is convenient to divide the image into small Regions of Interest (ROI) that include just a few atoms for two reasons: first to minimize the effect of background noise and second to use only few atoms in each region, which reduces the width of the detected counts distribution. To define the ROI, the image is integrated along the vertical direction and a ROI is defined as all the consecutive points of the integrated profile with values larger than a given threshold. Each region is extended by 5 pixels to each side and the overlapping ROIs are merged. The total number of counts in a ROI is obtained by integrating the counts and subtracting the readout offset (see Fig. 2.16).

Re-scaling atom fluorescence

To characterize the variation of the integrated fluorescence, a histogram of the total number of counts is created using 2.7×10^5 ROI at different positions. This is shown in Fig. 2.17a together with the expected

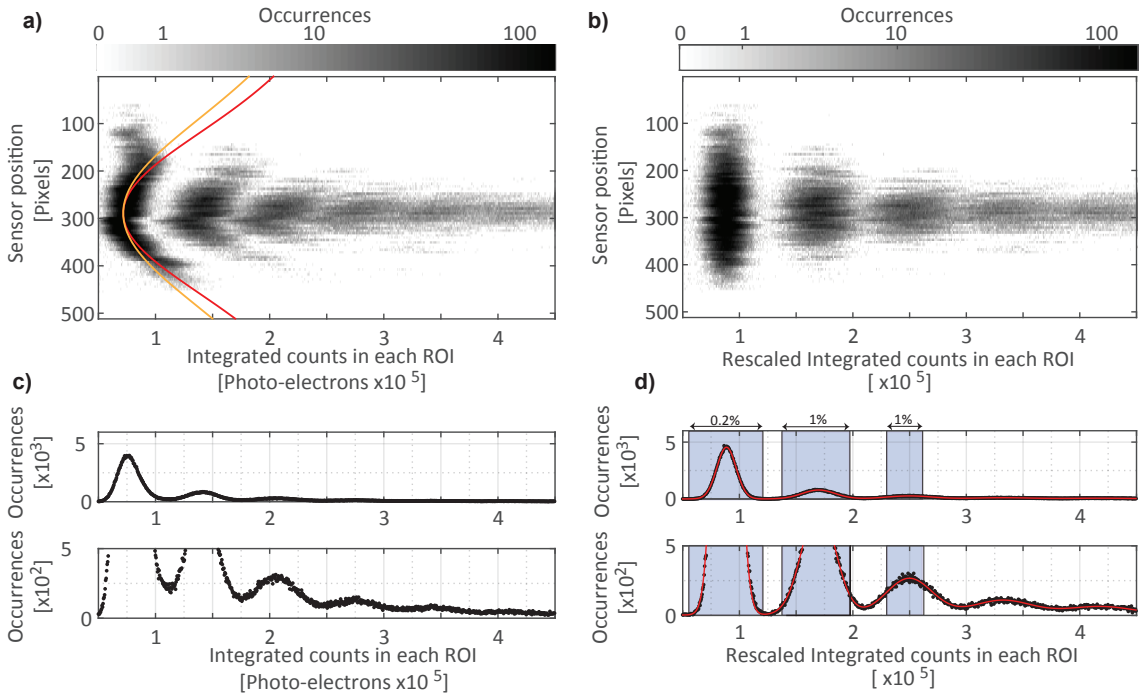

Figure 2.17. *Atomic fluorescence at different positions on the EMCCD.* **a)** Colored histogram for the number of counts in a ROI at different positions. The two curves are the expected change on the atomic fluorescence for a dipole trap with a waist of 5 µm (yellow) and 4.7 µm (red) **b)** Colored histogram for the number of counts in a ROI at different positions after re-scaling procedure. **c)** Histogram for the number of counts in a ROI at all positions. The lower curve is a zoom into the lower number of occurrences. **d)** Same as in **c** but for the EMCCD counts after the re-scaling procedure and the fit to five Gaussian curves. The acceptance intervals are indicated as the blue-shaded rectangles, the numbers at the top are the percentage of wrongly detected events inside the acceptance interval.

variation of the fluorescence due to the AC stark shift induced by a dipole trap with a waist of 5 µm and 4.7 µm[23]. In the histogram, the regions for one, two and three atoms can be easily distinguished. However, as expected, it is not uniform through the entire sensor. To estimate properly the number of atoms regardless the position on the sensor we fit a high order polynomial function to the part of the histogram containing only single atoms. The result of the fit is used to re-scale the detected number of counts for each position. Fig. 2.17b shows the histogram for the number of detected counts after the re-scaling procedure.

Counting atoms

To determine the number of atoms in a ROI that contains total number counts c, we define an acceptance interval $I(k) = [c_{\text{low}}(k), c_{\text{up}}(k)]$ and assume that the ROI contains k atoms if $c \in I(k)$. To quantify the precision of the inferred number of atoms in a ROI, we define the function

$$F(c) = B + \sum_{i=1}^{n} G_i(c), \quad G_i(c) = A_i \exp\left(-\frac{(c-\mu_i)^2}{2\sigma_i^2}\right), \tag{2.22}$$

[23] The trap was designed to have a waist of 5 µm at 880 nm, but after changing the wavelength to 860 nm we estimated a waist of 4.7 µm from Raman sideband spectroscopy (see Chap 5).

Table 2.3. Acceptance intervals for atom counting

No. atoms	Acceptance interval	ROIs in the acceptance interval, $N(k)$	Wrong number of atoms, Err(k)
1	$4\,\sigma_1$	99.994%	0.2%
2	$2.15\,\sigma_2$	97%	1%
3	$0.8\,\sigma_3$	58%	1%

being $G_i(c)$ Gaussian distributions and B a general offset. We fit the function $F(c)$ to the integrated counts histograms (see Fig. 2.17d), and use the results of the fit to determine the probability that the number of atoms in a ROI was wrongly determined by

$$\mathrm{Err}(k) = \frac{\int_{c_{\mathrm{low}}(k)}^{c_{\mathrm{up}}(k)} \left[\sum_{i=1, i\neq k}^{n} G_i(c) + B\right] \mathrm{d}c}{\int_{c_{\mathrm{low}}(k)}^{c_{\mathrm{up}}(k)} \left[\sum_{i=1}^{n} G_i(c) + B\right] \mathrm{d}c}. \tag{2.23}$$

For example, for ROIs containing a single atom ($k = 1$), an acceptance interval of $4\,\sigma_1$ leads to Err(1) = 0.2%. In a similar way, the probability that a ROI containing k atoms is correctly assigned to the acceptance interval $I(k)$ is given by

$$N(k) = \frac{\int_{c_{\mathrm{low}}(k)}^{c_{\mathrm{up}}(k)} G_i(c)\mathrm{d}c}{\int_{-\infty}^{\infty} G_i(c)\mathrm{d}c}. \tag{2.24}$$

For example, an acceptance interval of $4\,\sigma_1$ leads to $N(1) = 99.994\%$, i.e. only 0.006% of the ROIs containing a single atom are outside the acceptance interval $I(1)$.

In most of the measurements that will be presented in this work, we use ROIs containing only one atom. In this case we define the acceptance interval as $4\,\sigma_1$. For ROIs containing more than one atom, the acceptance interval must be smaller since the accuracy for determining the number of atoms reduces as the number of atoms increases. To guarantee that the atom number is determined properly, for ROIs containing two and three atoms, the acceptance region is restricted to an error of 1% (see table 2.3 and Fig. 2.17d).

To determine the number of atoms in ROIs containing more than three atoms, it is necessary to use longer illumination times in order to separate better the count histograms in Fig. 2.17d. In such case, the number of photons a pixel detects before it saturates can be a limitation. This problem can be solved by using a larger magnification to distribute the photons over more pixels [75].

2.4.5 Characterization of the optical system

Counting the number of atoms in the dipole trap is the most elemental information that can be retrieved from the system. To take full advantage of the fluorescence image and determine the exact position of the atom in the lattice, it is necessary to know the characteristics of the optical system. In this section, the characterization of the line spread function for the imaging system is presented.

Line Spread Function

When the light emitted from an object is collected using an optical system, it is unavoidable that diffraction occurs at the edge of the lenses due to their finite clear aperture. Such diffraction blurs the image created and imposes a physical limitation on its resolution. For the special case that the object is a point-like source, the created image is known as the Point Spread Function (PSF), which for a perfect lens system is the well known circular Airy pattern.

The image $i(x, z)$ of an arbitrary object located at the focal plane ($y = 0$) is smeared out by the PSF. This effect can be calculated by the convolution of the object $o(x, z)$ and the PSF(x, z),

$$i\,(x,z) = (o * \mathrm{PSF})\,(x,z) = \int_{-\infty}^{\infty}\int_{-\infty}^{\infty} o\,(x,z)\,\mathrm{PSF}\,(x-x', z-z')\,dx'dz'.$$

In practice, the integration limits can be restricted to the actual size of the image surface. When this condition holds, it is convenient to work on the Fourier space where, by the convolution theorem, their Fourier transforms are related by a simple product

$$I\,(u,v) = O\,(u,v)\,H\,(u,v)\,.$$

The capital letters represent the Fourier transform of the respective functions and $H\,(u,v) = \mathcal{L}\,\{PS\,F\,(x,z)\}$ is known as the Optical Transfer Function (OTF) that can be in general written as

$$H\,(u,v) = \mathrm{MTF}\,(u,v)\exp\left[-i\Theta\,(u,v)\right], \tag{2.25}$$

where $\mathrm{MTF}\,(u,v) = |H\,(u,v)|$ is known as the modulation transfer function and $\Theta\,(u,v)$ is the phase transfer function. The Fourier representation is convenient when analyzing an imaging system which is composed of n individual systems. In this case, the convolution theorem allows us to write the total response of the system as $H(u,v) = H_1(u,v)\cdot H_1(u,v)\cdot ...\cdot H_n(u,v)$, where $H_i(u,v)$ is the OTF of each individual system.

As mentioned earlier, to determine the position of atoms trapped in a 1D lattice it is convenient to simplify the problem by integrating the full image along the vertical direction (see Fig. 2.16). In this case, the spatial resolution of the integrated image is limited by the integrated PSF known as the Line Spread Function (LSF).

$$\mathrm{LSF}\,(x) = \int_{-\infty}^{\infty} \mathrm{PSF}\,(x,z)\,dz.$$

The LSF and the MTF for an ideal lens with a NA=0.43 are shown in Fig. 2.18.

In reality, a lens system is never perfect and aberrations can reduce the image quality by broadening the PSF. A common way to quantify the quality of the imaging system is by the Strehl ratio which compares the peak of the PSF for a real system to an ideal PSF. However, throughout this work, we will quantify the quality of the optical system using the analogous of the Strehl ratio for the LSF

$$S = \frac{\mathrm{LSF}\,(0)}{\mathrm{LSF}_{\mathrm{Ideal}}\,(0)}. \tag{2.26}$$

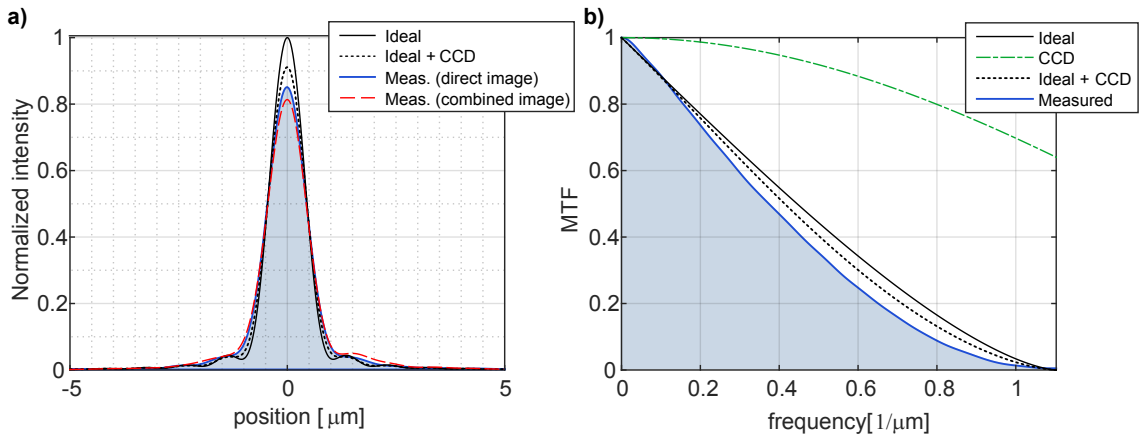

Figure 2.18. *Line Spread Function in the aplanatic region.* **a)** Ideal LSF (black solid line), effect of the CCD on the ideal LSF (dotted black), LSF for the direct image (shaded area and solid blue line) and the LSF for the combined image (dashed red). **b)** Modulation transfer function of an ideal airy function (solid black), MTF of the CCD sensor (dash-dotted green line), and the combination of both (dotted dark line). The shaded area and blue line is the calculated MTF of the measured LSF for the direct image.

Effect of the CCD sensor

To create an image with a high signal to noise ratio using the EMCCD camera, it is convenient to use as few of pixels as possible in order to reduce the influence of the background noise. However, there is a minimum number of pixels that must be used in order to prevent information loss due to the spatial averaging of the CCD. The Nyquist-Shannon sampling theorem [83] shows that the PSF must be imaged onto more than two pixels, i.e. $(\lambda/2\mathrm{NA}) > 2\Delta_p$, where Δ_p is the pixel size on the object plane. Writing $\Delta_p = L_{\mathrm{pix}}/M$, with M being the magnification and L_{pix} the pixel size, we find a direct condition on the magnification

$$M > \frac{4\mathrm{NA}L_{\mathrm{pix}}}{\lambda} \approx 35, \tag{2.27}$$

where we have used a NA = 0.43.

When an image is projected on a CCD, the device creates a discretized image that is sampled with the periodic structure of the sensor. The discretized image is a convolution between the original image and the pixel response function $H_{\mathrm{CCD}}(u)$ [76]. For a sensor with square pixels and a uniform response, the pixel response function is given by [84]

$$H_{\mathrm{CCD}}(u) = \mathrm{sinc}(\Delta_p u), \tag{2.28}$$

where $\mathrm{sinc}(x) = \sin(\pi x)/\pi x$. The MTF corresponding to Eq. (2.28) is shown in Fig. 2.18b using a (measured) magnification of $M = 35.4$ and the effect of $H_{\mathrm{CCD}}(u)$ on the ideal LSF is shown in Fig. 2.18a. There one can see that the CCD reduces the amplitude of the LSF down to ~ 0.91. However, this represents a good trade-off since, according to Eq. (2.28), no information is lost due to the spatial filtering of the CCD.

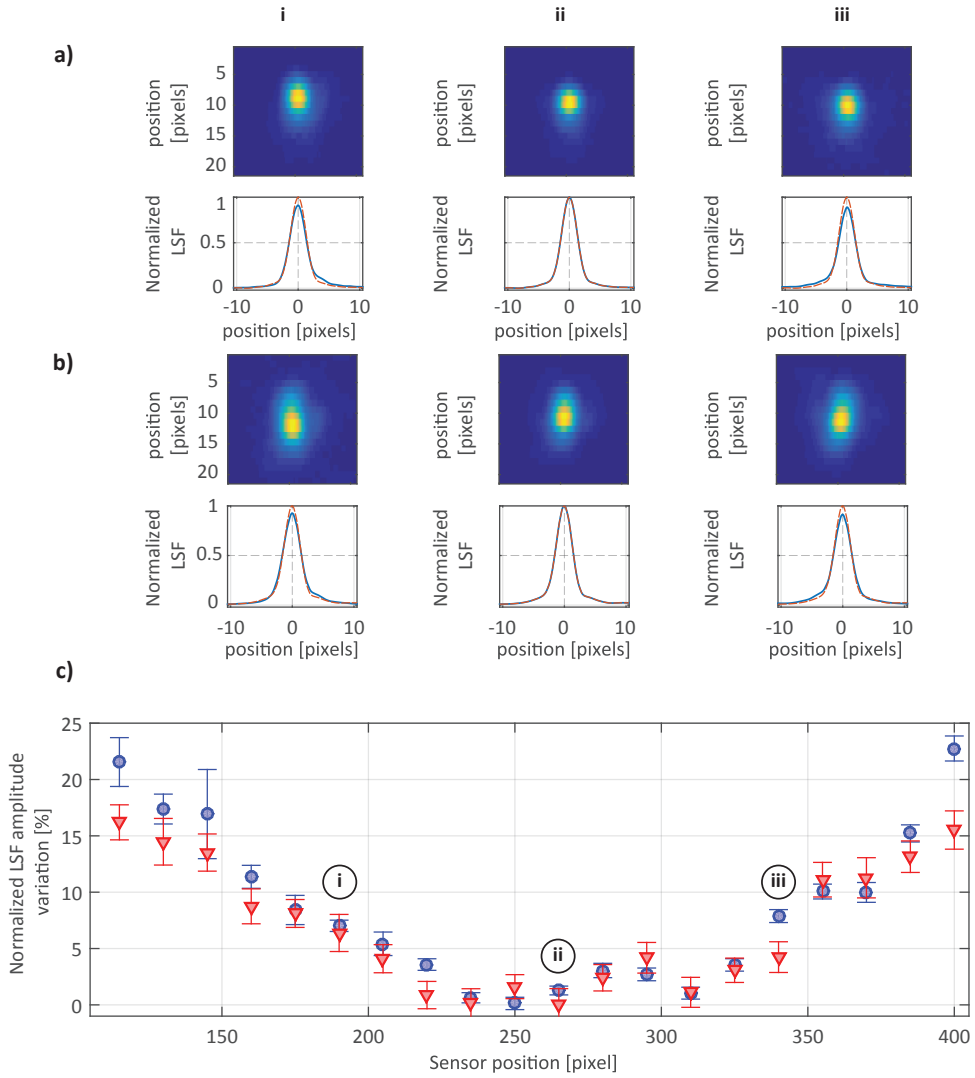

Figure 2.19. *Position-dependent line spread function*. **a)** Images obtained after the stacking procedure for single atoms at different positions on the sensor (top), and their corresponding LSF (solid line) together with the central LSF as a reference (dashed line). **b)** Same as **a** but using the combined images (i.e. with retro-reflector). **c)** Amplitude variation of the LSF at different positions on the sensor. The triangles represent the data for the direct image and the circles for the combined image.

Measurement of the LSF using individual atoms

Using the optical system depicted in Fig.2.2a, we observe atoms trapped in the 1D lattice along 230 µm. This field of view is a large area and we expect that the quality of an image varies in this region. To determine the quality of the optical system, we use the images of individual atoms in order to estimate the LSF at different positions on the CCD.

The LSF is obtained using the following algorithm:

1. The ROI are defined in the same way as in sec 2.4.4. But now, 30 extra pixels to each side are used

instead of 5 to guarantee that the long wings of the LSF are included.

2. Only ROI containing single atoms are considered. Then a Gaussian curve is fitted to the integrated profiles of single atoms. The fit gives as a result the atomic position with sub-pixel accuracy.

3. Each integrated profile is interpolated to increase the number of points; every pixel is divided into 16 subpixels and the profile is interpolated using cubic spline interpolation. Then an average profile is obtained by stacking all individual atoms centered at the same position. The result is a first approximation to the real LSF.

4. The new LSF is used to fit integrated profile to obtain the position of the single atoms once more. Then the same stacking procedure, described in step 3, is repeated to obtain a new LSF. This process is repeated 5 times, each time using the new LSF to find the atom's position.

Fig. 2.19 shows the variation of the amplitude for the LSF (normalized to its area) at different positions on the sensor[24]. The analysis was done for the direct image (no retro-reflected light) and for the combined image. In both cases the amplitude varies less than 5% in the interval from pixel 220 to 325, which corresponds to an aplanatic region of 55 μm. From now on, we use only atoms within the aplanatic region, which is necessary for a proper determination of an atom's positions by fitting the image using a common LSF.

The LSF, and its corresponding MTF, obtained using only single atoms in the aplanatic region are shown in Fig. 2.18. From the cutoff frequency of the MTF for the direct image, $\nu_c \approx 1.1\,\mu m^{-1}$, we estimate a NA of [85]

$$\mathrm{NA} = \frac{\nu_c \lambda}{2} = 0.43 \tag{2.29}$$

which is smaller than the expected value (NA= 0.5). This reduction may be due to an aperture that is located in the imaging path which is used to reduce the stray light. From the measurement of the LSF, we estimate an amplitude of $S = 0.85$ for the normal image, and $S = 0.81$ for the combined image (see Fig. 2.18).

There are different possible reasons that can explain the reduction of the LSF's amplitude, for example.:

Atomic motion in the radial direction. Following Refs. [75, 86] we estimate a reduction of less than 3% of the Strehl ratio due to the atomic motion.

Atoms-lens decentration. If the atoms are not aligned with the optical axis of the aspheric lens, aberrations in the optical path will lead to a reduction of the Strehl ratio. By simulating the optical system with a decentration of 100 μm, we expect a reduction of 20% on the Strehl ratio[25].

2.4.6 Position determination in the lattice

In the previous sections, we have shown that it is possible to determine the number of trapped atoms with good accuracy by taking images with an exposure time of only 20 ms and we have determined the LSF of the optical system. In this section, we use the LSF obtained in Sec. 2.4.5 to estimate the atom's position in the lattice and we quantify the accuracy of the position determination.

[24] Only atoms at the indicated position ±1pixel are used.
[25] Without taking into account the effect of the CCD.

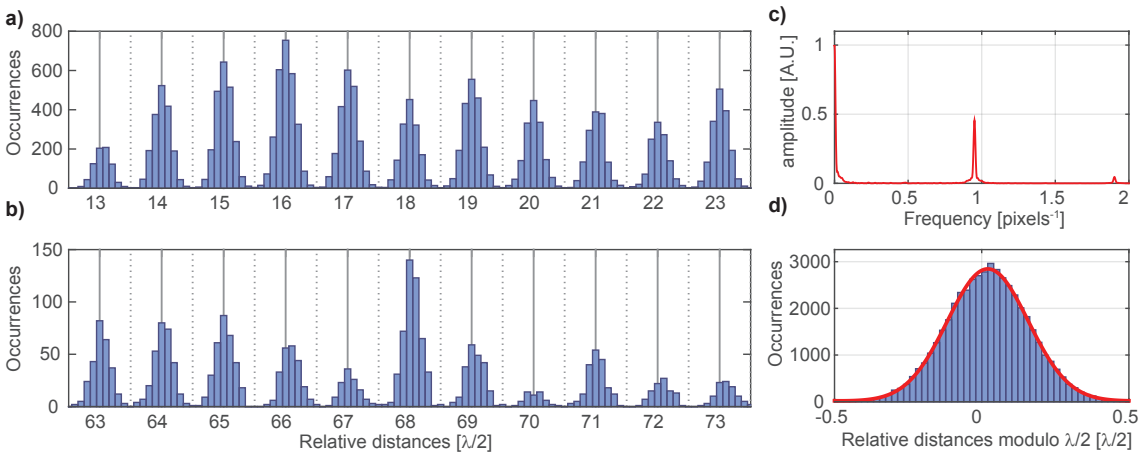

Figure 2.20. *Relative distances.* **a,b)** Histogram for relative distance between two single atoms in different ROIs. **c)** Fast Fourier transform of the self convolution for the distance histogram shown in **a,b**. **d)** Reduced histogram for the relative distance between two atoms in different ROIs.

Single atom case

To estimate the position of well resolved single atoms, we use only regions of interest within the aplanatic region that contain a single atom. The position of the atom in the ROI is obtained by a least-square fit of the LSF to the integrated profile. In order to quantify the accuracy of the position determination, the location of $4.8{\times}10^4$ single atoms is determined and the relative distance between all atoms that belong to the same image is calculated. Fig. 2.20a shows the histogram for the relative distances between single atoms. In this histogram, the periodic structure of the lattice is clearly visible.

The magnification of the optical system can be calibrated using the periodicity of the positions. To this end, we calculate the fast Fourier transform of the auto-correlation function for the histogram shown in Fig. 2.20a,b. The frequency is estimated with good accuracy by fitting the peak to the Fourier spectrum (see Fig. 2.20c) obtaining a value of 1.051 ± 0.002 pixels per lattice site which corresponds to a magnification of 35.4.

Although no information about the lattice structure was used in the fitting procedure, it is clear from the histograms that the position of the atoms is well determined. In order to quantify the accuracy of the position determination, a "reduced" histogram is created by taking the relative distances modulus the lattice constant, i.e. $\tilde{d} = \mathrm{mod}(d + \lambda/2, \lambda/2)$ (see Fig. 2.20d). The reduced histogram is fitted with the function

$$f(n,\mu,\sigma) = A\exp\left[-\frac{(n-\mu)^2}{2\sigma^2}\right] + \underbrace{A\left(\exp\left[-\frac{(n-\mu-\lambda/2)^2}{2\sigma^2}\right] + \exp\left[-\frac{(n-\mu+\lambda/2)^2}{2\sigma^2}\right]\right)}_{g(n,\mu,\sigma)} + B, \qquad (2.30)$$

where the first part corresponds to the central Gaussian, the second part ($g(n,\mu,\sigma)$) accounts for neighboring Gaussian curves whose tails enter this region, and B is a general offset. From a fit to Eq. (2.30) we obtain a width of $\sigma = 0.133 \pm 0.006\,\lambda/2$ from which we can determine the accuracy of the fitting procedure $\Delta x = \sigma/\sqrt{2} = 40 \pm 2$ nm. The measured precision is, up to a factor of two, in good agreement with the theoretical expectation $\Delta x_{\mathrm{theo}} = 23$ nm obtained by using Eq. (2.14) where $\mathrm{RMS}_{\mathrm{PSF}} = 0.5\,\mu$m,

$\Delta_p = 0.45\,\mu\text{m}$, $\sigma_b = 0.98\text{ph.e}^-/\sqrt{\text{pixel}}$, $n_\text{V} = 16$ and $N = 600$, which were obtained in different sections of this chapter.

Using Eq. (2.30), it is also possible to estimate the fraction of atoms whose position is determined on a wrong lattice site by

$$\text{Error} = \frac{\int_{-\lambda/4}^{+\lambda/4} g(n,\mu,\sigma)}{\int_{-\lambda/4}^{+\lambda/4} f(n,\mu,\sigma)}, \tag{2.31}$$

giving, as a result, an error for the determination of the lattice site in only 0.8% of the cases.

Two atom case

If two atoms are inside the same region of interest, then two LSFs, with their relative distance as a free parameter, are fitted to the integrated profile (see Fig. 2.21). From the relative distance of each atom pair a histogram is created (see Fig. 2.22a). In the histogram, it is clear that for separations larger than two lattice sites, the position is determined with a good accuracy. In the same fashion as described above, by fitting Eq. (2.30) to the reduced histogram (see Fig. 2.22b), we obtain $\sigma = 0.139 \pm 0.008\,\lambda/2$, leading to an accuracy of 42 ± 2 nm on the position determination, and using Eq. (2.30) we estimate a wrong determination of the lattice site in 0.6% of the cases.

For the case of small separation ($d < 2.5\,\lambda/2$), however, by fitting two LSFs to the integrated profile we cannot resolve properly the distance between the atoms. In some cases the fitting procedure even converges to zero distance, which is not possible due to light-induced collisions [45]. The problem for the small distances can be easily solved by using an average position obtained from different images of the same atoms. For example, Fig. 2.22c shows the relative distance using the average position obtained from two images. Taking into account that the acquisition time for each picture is only 20 ms, doubling the number of pictures extends the image acquisition time, but remains fast compared to previous implementations [66, 75].

2.5 Summary and conclusions

This chapter provides the description of the experimental system used to cool, trap, and detect a small number of ^{87}Rb atoms. Small ensembles of atoms are loaded in a small magneto-optical trap from the background gas and transferred into a tightly-focused standing wave dipole trap created by a set of aspheric lenses mounted inside the vacuum chamber. The same aspheric lenses, together with a Porro prism, are used to collect the atomic fluorescence and direct it to an EMCCD camera in order to image the trapped atoms. The Porro prism used to increase the number of detected photons does not alter significantly the imaging quality of the system. The combination of the aspheric lenses and the prism leads to a measured detection efficiency of $2.87^{+0.07}_{-0.32}\%$.

The tightly focused dipole trap creates a position-dependent AC-Stark shift, which is corrected on the recorded images in order to properly count the number of atoms in the dipole trap. Furthermore, the large collection efficiency of the optical system allows a fast determination of the position of atoms in the trap, with an accuracy of 42 ± 2 nm using images acquired in ~ 20 ms.

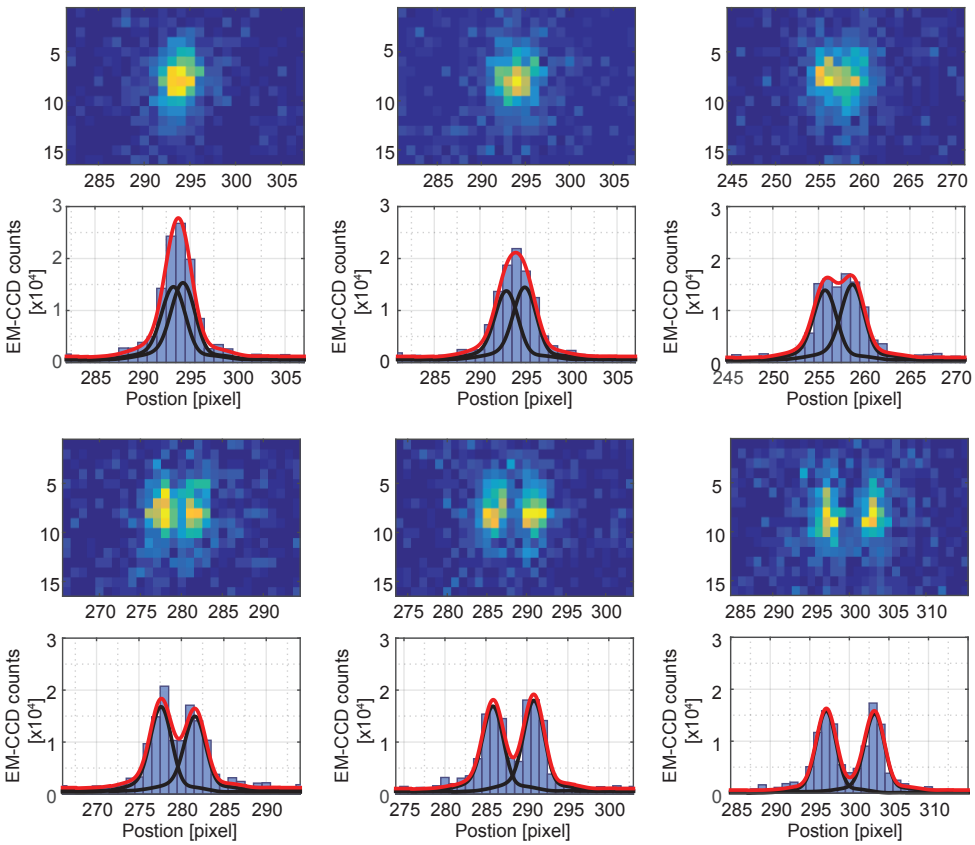

Figure 2.21. *Fitting atom pairs.* LSF fit for two atoms in the same region of interest separated by 1,2,3,4,5 and 6 lattices sites. The images were taken including the retro-reflected light.

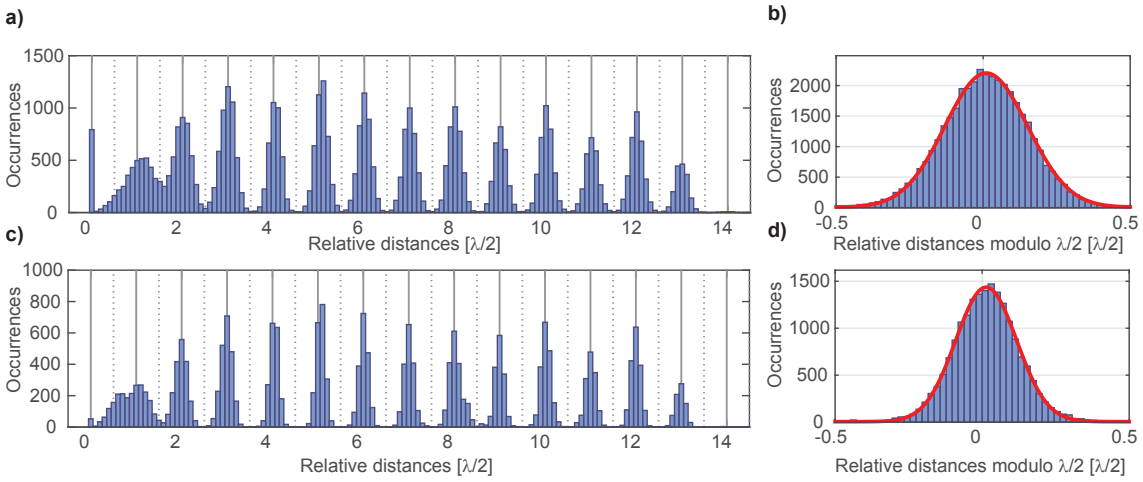

Figure 2.22. *Relative distances.* **a)** Histogram for the relative distance of two atoms in the same ROI. The sharp peak at zero distance comes from a wrong convergence of the fitting algorithm. **b)** Reduced histogram for the relative distance between two atoms in the same ROI. **c)** Histogram for the relative distance using the average position obtained from two successive images. **d)** Reduced histogram for the relative distance using the average position obtained from two successive images (for $d > 2.5\lambda/2$).

The constructed experimental system allows for an efficient usage of both the trapping light and the collected fluorescence. A deep optical trap is created with a relatively low power, due to the tight focusing of the light by the aspheric lenses mounted inside the vacuum system. The chosen magnification for the imaging system distributes optimally the light over the minimum number of pixels necessary to preserve spatial information. This minimizes the influence of the background noise and, combined with the large detection efficiency, reduces the image acquisition time by a factor of 50 compare to previous experimental implementations [66, 75]. The fast imaging on this system can be used for a real-time position determination of atoms in the lattices [87], which opens the possibility for real-time feedback.

CHAPTER 3

Resonance fluorescence of neutral atoms in optical dipole traps

Spatially resolved imaging of optically trapped neutral atoms is an important feature of many cold atom experiments in the field of quantum simulation and quantum information processing. Optical microscopes with high numerical aperture make it possible to detect with high fidelity the presence of atoms in individual sites of two-dimensional optical lattices by resolving fluorescence light under near-resonant illumination [21, 22]. The ability to resolve and address single lattice sites is an important tool for cold atom simulators of quantum many-body physics and could offer a route towards scalable quantum information processing with cold atoms.

The balance of heating and cooling due to photon recoil, the differences in the trap potentials of ground and excited states, Doppler, and sub-Doppler effects determine the time until atoms are lost from the optical trapping potentials as well as the number of scattered photons during the illumination process. It is known that by choosing adequate parameters for the illumination light in a 3D Molasses configuration it is possible to reduce the temperature of an optically trapped atom leading to long storage times [88], which has indeed been used in the previous chapter of this work.

For a precise manipulation and determination of the internal and external states of a trapped atom, it is necessary to have a well-controlled system. In particular, for a quantitative study of the interaction between an optically trapped atom and a Near-Resonant Field (NRF), it is required to have a good control on the NRF's parameters, for instance, polarization and intensity. Although a molasses illumination is useful to cool the atoms in a dipole trap, the polarization of the light fields is not well defined. Moreover, the counterpropagating beams create standing waves, which lead to undesired spatial intensity variations. Therefore, for a precise control on the near-resonant illumination, it is essential to use a single beam with a well-defined polarization and an homogeneous intensity.

The interaction of an optically trapped atom with a single near-resonant beam, unlike an optical molasses, can lead to strong heating effects. Even though in the literature many studies exist for different cooling mechanism such as Raman [89], cavity [90–95] and EIT cooling [96, 97], only a few comprehensive theoretical models have investigated the dynamics of atoms trapped in optical potentials interacting with a near-resonant illumination field [98, 99]. Nevertheless, a quantitative understanding of the heating dynamics in such a system is crucial in order to find useful parameters for the NRF which can allow us to obtain information on the trapped atom without removing the atom from the trap.

One way to study the dynamics of optically trapped atoms, pioneered by Gordon and Ashkin [72] and Dalibard and Cohen-Tannoudji [73], is by using a semiclassical model to determine the momentum diffusion coefficient, which can be used to describe the evolution of the system, e.g. by the Fokker-Planck equation. However, using only the momentum diffusion coefficient it is not possible to quantify atom losses. The losses can be quantified by, instead of momentum, calculating the total energy diffusion constant. This constant can be used to model the evolution of the atom's energy and determine when the energy exceeds the trap depth, i.e. when the atom is lost [100]. However, the determination of this constant for a neutral atom trapped in a sinusoidal potential is impossible. The harmonic approximation for the trap is not valid for a hot atom and the strong dependence among all internal and external degrees of freedom makes a numerical calculation intractable. Therefore, the development of alternative methods to describe the dynamics of an optically trapped atom under near-resonant illumination is necessary.

This chapter is dedicated to studying the heating dynamics of a neutral atom trapped in a standing wave dipole trap interacting with a NRF. The analysis is presented for two different regimes. First, in Sec. 3.1 the heating induced by a weak resonant beam is presented. In this regime, we will show that heating processes are well described by a series of quantum jumps between the atomic internal states creating dipole force fluctuations, which can strongly heat up the trapped atom. Later in Sec. 3.2, the case for a strong and non-resonant field is addressed using the *dressed state* formalism. In this case, the problem is mapped to a series of quantum jumps between the dressed state potentials, which for large detunings leads to a strong reduction of heating by the dipole force fluctuations. In both sections, a validation with experimental data is presented.

3.1 Heating induced by weak near-resonant illumination

A weak NRF and a strong far-detuned dipole trap interacting with a neutral atom contribute in a different way to the internal and external dynamics. On the one hand, the weak NRF drives the internal state of the atom; on the other hand, the far-detuned dipole trap creates a potential that determines the atomic motion, but this potential depends on the atom's internal state. Therefore, the simultaneous interaction with these two fields couples the internal and external degrees of freedom. The problem of photon absorption in such configuration has been studied by Cohen-Tannoudji and Reynaud [71, 101]. However, we are interested not only in the absorption process but also in the mechanical effects that this process entails.

The external dynamics strongly depends on the internal atomic state and, therefore, these two degrees of freedom cannot be in general treated independently. In this section, we will find conditions for a weak NRF for which the internal and external degrees of freedom can be decoupled. Finally, a semi-classical description of the atomic motion is presented and compared with experimental data.

3.1.1 Neutral atom interacting with two light fields

Let us start the discussion by building the Hamiltonian for the experimental system. In the experimental setup, atoms are confined in an optical dipole trap along the x axis, optically pumped to the state $F = 2, m_F = -2$, and later illuminated by a weak beam which propagates along the z axis and is near-resonant with the cycling transition. Only a single illumination beam is used in order to have a well-defined polarization and a uniform intensity. A simplified scheme of the experimental setup is depicted in Fig. 3.1a,b.

In Sec. 2.3.1, we have shown that for an optical trap with a large detuning, it is a good approximation to assume that Dipole Trap (DT) dressed-states are well approximated by the normal bare states

$$|\tilde{g}\rangle \equiv |-, N\rangle_{\mathrm{DT}} \approx |g, N\rangle\,, \quad |\tilde{e}\rangle \equiv |+, N\rangle_{\mathrm{DT}} \approx |e, N\rangle\,, \tag{3.1}$$

and that the dominant effect of the dipole trap is a position-dependent AC-Stark shift for the ground and excited states. Therefore, the Hamiltonian for the trapped atom can be approximated by

$$\hat{\mathbf{H}}_{\mathrm{A_{DT}}} = \frac{p^2}{2m} + [\hbar\omega_0 + U_e(\mathbf{r})]\,|\tilde{e}\rangle\langle\tilde{e}| + U_g(\mathbf{r})\,|\tilde{g}\rangle\langle\tilde{g}|\,, \tag{3.2}$$

where ω_0 is the atomic resonance in free space and $U_{g,e}(\mathbf{r})$ are the potentials induced by the dipole trap for the ground and excited states.

The coupling of the extra NRF is included in the same manner as in Eq. (2.1) described in Sec. 2.3.1, i.e. the Hamiltonian describing the full system in the RWA is

$$\hat{\mathbf{H}} = \hat{\mathbf{H}}_{\mathrm{A_{DT}}} + \hat{\mathbf{H}}_{\mathrm{NR}} + \hat{\mathbf{H}}_{\text{A-NR}}, \tag{3.3a}$$

$$\hat{\mathbf{H}}_{\mathrm{NR}} = \hbar\omega_{\mathrm{NR}}\left(\hat{a}^\dagger_{\mathrm{NR}}\hat{a}_{\mathrm{NR}}\right), \tag{3.3b}$$

$$\hat{\mathbf{H}}_{\text{A-NR}} = \frac{\hbar\Omega_{0,\mathrm{NR}}}{2}\left(\hat{\sigma}^\dagger\hat{a}_{\mathrm{NR}} + \hat{\sigma}\hat{a}^\dagger_{\mathrm{NR}}\right). \tag{3.3c}$$

where $\hat{a}^\dagger_{\mathrm{NR}}$, $\hat{a}_{\mathrm{NR}}$ are the creation and annihilation operators, ω_{NR} is the angular frequency, and $\Omega_{0,\mathrm{NR}}$ is the resonant Rabi frequency, all of them for the NRF.

3.1.2 Internal dynamics

The Hamiltonian $\hat{\mathbf{H}}$ in Eq. (3.3) describes the evolution of the system in the absence of spontaneous emission. However, to model the internal dynamics it is necessary to include the effects of the spontaneous decay of the excited state. For simplicity, we first assume that the atom is infinitely heavy and we do not consider the external degrees of freedom. The NRF is a single mode of electromagnetic field, which is identified by its wave vector $\mathbf{k}_{\mathrm{NR}}$ and polarization $\varepsilon_{\mathrm{NR}}$, containing N_{NR} photons with frequency $\omega_{\mathrm{NR}} = k_{\mathrm{NR}}c$, and near-resonant with the AC-Stark shifted atomic transition. If an atom is initially in its ground state, then the initial state of the system is

$$|\phi_i\rangle = |\tilde{g}, N_{\mathrm{NR}}\mathbf{k}_{\mathrm{NR}}\varepsilon_{\mathrm{NR}}, 0\rangle\,,$$

where the zero represents all empty modes. The interaction Hamiltonian $\hat{\mathbf{H}}_{\text{A-NR}}$ couples the initial state $|\phi_i\rangle$ to a final state $|\phi_f\rangle = |\tilde{e}, (N_{\mathrm{NR}}-1)\mathbf{k}_{\mathrm{NR}}\varepsilon_{\mathrm{NR}}, 0\rangle$. The final state $|\phi_f\rangle$ is, however, not only coupled to $|\phi_i\rangle$, but it is also coupled to all vacuum modes; the state $|\phi_f\rangle$ can decay by spontaneously emitting a photon to a previously empty mode $\mathbf{k}\varepsilon$, i.e. it is coupled to a continuum of states $|\phi_g\rangle = |\tilde{g}; (N_{\mathrm{NR}}-1)\mathbf{k}_{\mathrm{NR}}\varepsilon_{\mathrm{NR}}, \mathbf{k}\varepsilon\rangle$.

The temporal evolution of the state $|\phi_i\rangle$ can be easily understood in two extreme cases. If the state $|\phi_f\rangle$ is only coupled to the state $|\phi_i\rangle$ (no spontaneous decay), then this two-level system continuously undergoes Rabi oscillations. In contrast, if $|\phi_f\rangle$ were only coupled to the continuum (no stimulated emission), it would decay exponentially with a lifetime $\tau = \Gamma^{-1}$. The two limiting cases correspond to $\Omega_{\mathrm{NR}} \gg \Gamma$ and $\Omega_{\mathrm{NR}} \ll \Gamma$ where $\Omega_{\mathrm{NR}} = \sqrt{\Omega^2_{0,\mathrm{NR}} + \Delta_1^2}$ and Δ_1 is the detuning of the NRF to the AC-Stark shifted atomic transition. In the first case (intense field or large detunings), the dynamics is dominated by the

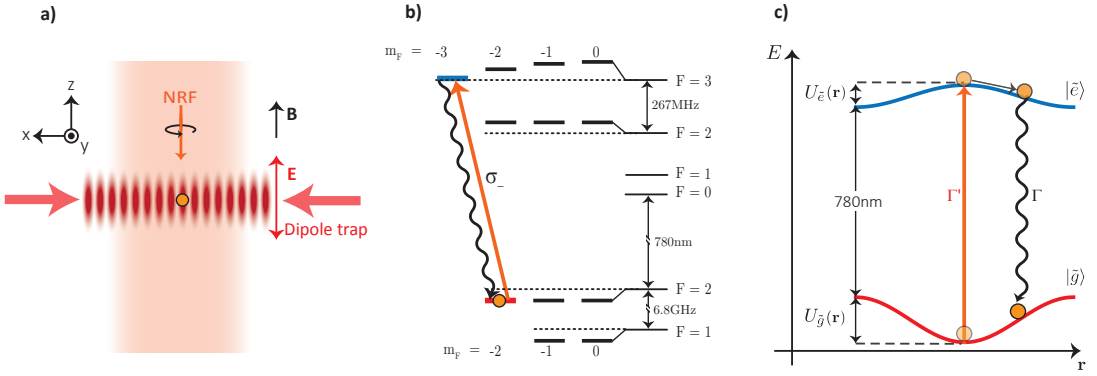

Figure 3.1. *Weak resonant field.* **a)** Simplified experimental scheme. **b)** Relevant ^{87}Rb spectrum including the AC-Stark shift. The Zeeman levels with positive m_F behave symmetrically around zero and are not shown. The arrow represents the NRF and the wavy line the spontaneous emission on the cycling transition. **c)** Dipole trap dressed-state model reduced to a two-level system with position-dependent AC-Stark shift for the cycling transition. The arrows illustrate the absorption and emission jumps leading to dipole force fluctuation.

Rabi nutation and it is not possible to describe the dynamics in terms of a transition rate or an absorption cross section [71]. In the second case (weak NRF), the coupling of $|\phi_f\rangle$ to the continuum $|\phi_g\rangle$ is much stronger than the coupling of $|\phi_f\rangle$ to $|\phi_i\rangle$, and if an atom is excited, then it will always spontaneously emit a photon into free space. Therefore, for a weak NRF we can neglect the coupling of $|\phi_f\rangle$ to $|\phi_i\rangle$ and describe the internal dynamics as a series of photon absorption and emission processes where a photon is absorbed at rate [71]

$$\Gamma' = \frac{\Gamma}{2}\frac{s}{1+s+4\Delta_1^2/\Gamma^2} \approx \frac{\Omega_{0,\mathrm{NR}}^2}{\Gamma}, \tag{3.4}$$

and spontaneously emitted at the natural decay rate Γ. It is important to keep in mind that this absorption-emission interpretation makes sense only for $\Omega_{\mathrm{NR}} \ll \Gamma$, otherwise stimulated emission induced by the NRF is not negligible any more.

3.1.3 Dipole force fluctuation: jumping regime

Describing the interaction between a two-level atom and a weak NRF as a series of quantum jumps between the ground and excited states allows us to simplify the description for the motional dynamics using a semi-classical model. The extension of the wave function of an atom trapped in the standing wave is small compared with the dimension of the trap, e.g., for the ground state in a trap with a depth of 3.46 mK, the axial extension is $x_{\mathrm{axial}} = \sqrt{\hbar/\omega_{\mathrm{axial}} m_{\mathrm{Rb}}} \approx 10\,\mathrm{nm}$. Furthermore, the temperature of the atoms in the trap is significantly higher than the ground state energy and thus. It is, therefore, a good approximation to describe the motion in a classical way. When the atom is in its ground (excited) state, the external dynamics is determined by the potential $U_{\tilde{g}}$, ($U_{\tilde{e}}$), position and momentum are obtained by solving the classical equation of motion. This process is schematically depicted in Fig. 3.1c.

Dipole force fluctuation in the Harmonic approximation

To understand how the jumping process increases the temperature of a trapped atom, we use a simple model and focus only on the dynamics for the axial component. The axial direction is the strongest confinement and its characteristic time scale is much faster than for the radial component. To further simplify the problem, the excited state potential is set to zero, thereby neglecting its anti-confinement. This is a reasonable assumption since, as described in Sec. 2.3.4, for the cycling transition and $\lambda_{\mathrm{DT}} = 860\,\mathrm{nm}$, $U_e \approx |U_g|/10$.

We start the description for an atom in its ground state that is initially at a position x with momentum p and has an total initial energy

$$E_i = U_g(x) + \frac{p^2}{2m}. \tag{3.5}$$

When the atom is excited it travels at a constant speed (since $U_e = 0$) for a distance $\Delta x = \frac{p}{m}t$ during the time it remains excited. When it decays back to its ground state, the energy changes due to the small displacement by an amount

$$\Delta E = U_g(x + \Delta x) - U_g(x). \tag{3.6}$$

To quantify the energy change it is convenient to re-write $U_g(x + \Delta x)$ in Eq. (3.6) as a Taylor series, leading to

$$\Delta E = \sum_{n=1}^{\infty} \frac{1}{n!} U_g^{(n)}(x) \left(\frac{p}{m}t\right)^n. \tag{3.7}$$

Eq. (3.7) represents the energy change for an atom that was initially at position x with a momentum p and has been exited for a finite time t. However, we are not interested in a single realization but in an average over every possible outcome; therefore, we must average over all possible times and positions. To average over time, we consider that the random time an atom spends in the excited state is described by an exponential distribution with the natural decay time Γ^{-1}. Averaging Eq. (3.7) we obtain

$$\langle \Delta E \rangle_t = \sum_{n=1}^{\infty} U_g^{(n)}(x) \left(\frac{p}{\Gamma m}\right)^n, \tag{3.8}$$

where $<>_t$ denotes the average over time.

When an atom moves in a one-dimensional conservative potential, it crosses every point in the forward and backward direction. This means that for a given position x, there are two possible values for the momentum with the same magnitude but opposite direction $\pm p$. Therefore, when averaging Eq. (3.8) over momentum using a symmetric momentum distribution, all the odd terms in the expansion cancel and only the even powers remain[1]

$$\langle \Delta E \rangle_t = \sum_{n=1}^{\infty} k_{\mathrm{DT}}^{-2n} U_g^{(2n)}(x) \left(\frac{k_{\mathrm{DT}}\, p}{\Gamma m}\right)^{2n}. \tag{3.9}$$

Here we have introduced the wave vector $k_{\mathrm{DT}} = 2\pi/\lambda_{\mathrm{DT}}$ which contains information about the characteristic length of the trap. For small velocities, which holds for atoms in the dipole trap, it is satisfied that

[1] Note that the average over momentum has not been performed, we have just used the symmetry of the distribution to cancel the odd terms in the sum. To calculate the average over momentum, the explicit form of the density distribution is necessary, but it depends on the exact shape of the potential and, therefore, a general expression cannot be provided.

$\frac{k_{\mathrm{DT}}\, p}{\Gamma m} \ll 1$ and hence only the first term in Eq. (3.9) plays an important role

$$\langle \Delta E \rangle_t \approx U_g''(x) \left(\frac{p}{\Gamma m} \right)^2 . \tag{3.10}$$

Eq. (3.10) means that, on average, the net heating induced by the Dipole Force Fluctuation (DFF) is generated only by the curvature of the potential and not by the gradient. Furthermore, positive curvature leads to heating but a negative curvature reduces the total energy.

In the harmonic approximation for the standing wave potential, it is straightforward to calculate the average value for Eq. (3.10) over position

$$\langle \Delta E \rangle_{t,x} \quad = \quad \int \rho_{\mathrm{HO}}(x, E) \, \langle \Delta E \rangle_t (x) \, \mathrm{d}x = \frac{2 U_0 k_{\mathrm{DT}}^2 E}{m \Gamma^2}, \tag{3.11}$$

where $\rho_{\mathrm{HO}}(x, E) = 1/\pi \sqrt{x_{\mathrm{max}}^2 - x^2}$ is the position distribution probability for a harmonic oscillator, with x_{max} being the turning points for an atom with total energy $E = \frac{p^2}{2m} + U_g(x)$ [102].

The expression in Eq. (3.11) provides the mean energy change per scattering event due to the DFF. To get an idea about its magnitude, we compare it with the energy gained by the recoil due to photon emission.

$$\frac{\langle \Delta E \rangle_{t,x}}{E_{\mathrm{rec}}} = \frac{4 \lambda_{\mathrm{Rb}}^2 U_0 E}{\lambda_{\mathrm{DT}}^2 \Gamma^2 \hbar^2}, \tag{3.12}$$

For a numerical example, we use an energy $E = k_{\mathrm{B}} \times 50\,\mu\mathrm{K}$, corresponding to a typical initial temperature of the molasses-cooled trapped atoms, obtaining

$$\frac{\langle \Delta E \rangle_{t,x}}{E_{\mathrm{rec}}} \approx 2 \times U_0[\mathrm{mK}], \tag{3.13}$$

where the value for the trap depth must be written in millikelvin. For deep traps, the induced heating can be stronger than the heating induced by photon recoil and, furthermore, it increases exponentially with time. The effect becomes even larger when including the repulsive potential U_e.

To find the trap depth at which the DFF is always smaller than the recoil energy, we consider that the maximum temperature of an atom in the trap is $E = U_0$. Therefore, from Eq. (3.12) the heating induced by the DFF is always smaller than the photon recoil heating when

$$U_0 < \frac{\lambda_{\mathrm{DT}} \Gamma \hbar}{2 \lambda_{\mathrm{Rb}}} \approx 300\,\mu\mathrm{K}\, k_{\mathrm{B}}. \tag{3.14}$$

Experimental implementation

To experimentally observe the heating induced by the DFF, we perform a simple experiment. We start by loading a few atoms in the dipole trap and optically pumping them to the state $F = 2, m_F = -2$. The trap depth is then adiabatically changed to a value U_{set} and a weak NRF, orthogonal to the dipole trap, is turned on for a time t. The weak field is near-resonant with the cycling transition of the AC-Stark shifted atom at the bottom of the trap. From the experiment, we determine the number of atoms that remain

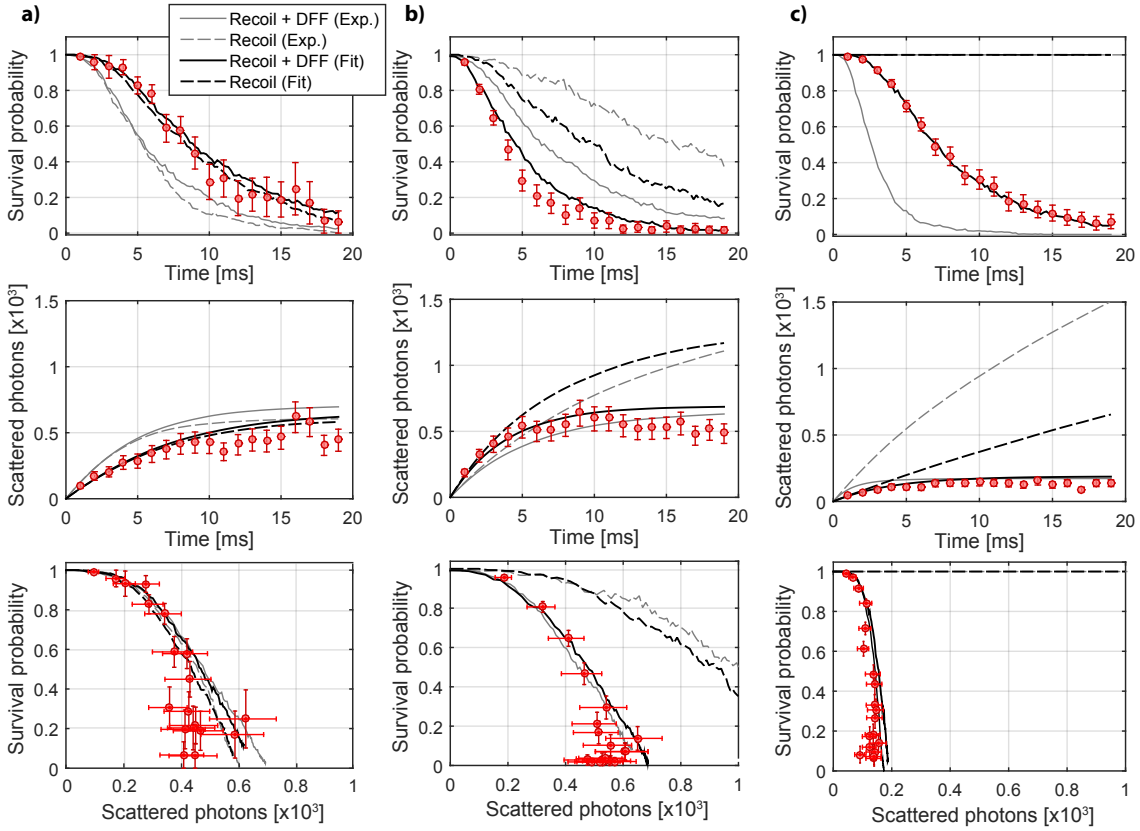

Figure 3.2. *Experiment and theory for heating by a weak near-resonant field.* In the upper graphs, the survival probability for a trapped atom under resonant illumination. The middle plots show the estimated number of scattered photons for different illumination times. The lower plots show the survival probability after scattering a given number of photons. In all plots, the red circles are the experimental data and the solid and dashed lines correspond to the Monte Carlo simulations using the measured (gray lines) and adjusted parameters (black lines) for both models (see text). The data was recorded for **a)** U_{set} =0.28 mK, **b)** U_{set} = 0.7 mK and **c)** U_{set} = 3.46 mK. The error bars represent the 95% confidence interval.

trapped after the illumination time and the number of scattered photons. For more details regarding the experimental sequence see Sec. 4.1.2.

In the experiment, the depth of the dipole trap was set to three different values, $U_{\text{set}} = 0.28, 0.7, 3.46$ mK, which create an AC-Stark shift of $\Delta_{\text{AC}}/2\pi = 6,\ 15,\ 79$ MHz. For the measurements, we use a NRF with an intensity of $0.015\, I_{\text{sat}}$ detuned by $\Delta_{\text{NR}}/2\pi = 9, 17, 79$ MHz with respect to the free space resonance respectively. The experimental data is shown in Fig. 3.2 together with two different theoretical models which are explained below.

Dynamics model

To understand the experimental data presented in Fig. 3.2 two different Monte Carlo simulations are presented. The first uses is a simple model that considers only the effect of the photon recoil, and the

second one includes also the effect of the DFF.

Heating by photon recoil. In this model, we neglect the time that the atoms spends in the excited state. Therefore, the atom is always trapped and the dynamics is always described by the ground state potential. In this case, the only heating source is the recoil induced by the photon absorption-emission process (no DFF is present). The photon absorption events are chosen randomly according to the photon scattering rate Γ' in Eq. (3.4) and the spontaneous emissions by the natural decay rate Γ. For each absorption event, the photon recoil is added in the propagation direction of the NRF and for each spontaneous emission, the momentum recoil is added in a random direction according to the dipole radiation distribution (for details regarding the simulation see Appendix C). The results of the Monte Carlo simulation are presented as the dashed lines in Fig. 3.2.

Heating by dipole force fluctuation. In this case, when the atom is in the ground state, its motion is determined by the ground state potential, but after each photon absorption, the atom remains in the excited state for a short time t_{exc} and during this time it feels a repulsive potential. The time t_{exc} is chosen randomly from an exponential distribution $\rho(t) = \Gamma \exp(-\Gamma t)$, and the photon recoil is added in the same manner as in the previous case. This model recreates the heating process due to the photon recoil and the DFF, the results of the simulation are shown as the solid line in Fig. 3.2.

For each of the models, two simulations are shown. The first simulation uses the values for the trap depth, illumination intensity and frequencies as measured in the experiment. These are shown as light gray lines. In the second simulation, the values are adjusted (within the experimental uncertainties) to better fit the data[2], these are shown as black lines; from now on, we just focus on this simulation for the discussion of the results.

At the lowest value for the trap ($U_{\mathrm{set}} = 0.28\,\mathrm{mK}$) we expect that the DFF does not play an important role since its effect is smaller than photon recoil heating (cf. Eq. 3.14). This can be appreciated in Fig. 3.2a, where both models (solid-black and dashed-black lines) give the same result and agree with experimental data. However, as the trap depth increases it is expected that the DFF increases, leading to a heating stronger than the recoil heating. This effect is already visible for $U_{\mathrm{set}} = 0.7\,\mathrm{mK}$ and it becomes strong for $U_{\mathrm{set}} = 3.46\,\mathrm{mK}$. For such a deep trap, if only the photon recoil were present (no DFF), it would allow an atom to scatter $\sim 5 \times 10^3$ photons before it is expelled from the trap. However, the measurements show that an atom is lost after scattering less than 200 photons, which reveals the significance of the DFF.

The deviation of the experimental data with respect to the simulation using the measured values in the experiment (gray lines) comes from the fact that small variations on the experimental parameters modify the resonance frequency leading to larger or smaller scattering rates. Therefore, by a small adjustment of these parameters, one finds a better agreement for both the survival probability and number of scattered photons as a function of time (black lines). Most importantly, however, is that these small adjustments on the experimental values just change the rate at which the atom scatters a photon, but the total gain of energy per scattered photon is insensitive to the exact values of the experimental parameters. This effect is visible when plotting the survival probability as a function of the number of scattered photons (see the third row of plots in Fig. 3.2). In these plots, both simulations (adjusted and not adjusted parameters) lead to the same result and agree well the experimental data.

[2] For the simulations we use the following values in the Monte Carlo simulation in Fig. 3.2: a) $U_{\mathrm{sim}} = 0.97U_{\mathrm{exp}}$, $I_{\mathrm{sim}} = 0.87I_{\mathrm{exp}}$, $\Delta_{\mathrm{sim}} = \Delta_{\mathrm{exp}} + 1\,\mathrm{MHz}$, $T = 20\,\mu\mathrm{K}$ b) $U_{\mathrm{sim}} = U_{\mathrm{exp}}$, $I_{\mathrm{sim}} = 1.13I_{\mathrm{exp}}$, $\Delta_{\mathrm{sim}} = \Delta_{\mathrm{exp}} - 1\,\mathrm{MHz}$, $T = 60\,\mu\mathrm{K}$ c)$U_{\mathrm{sim}} = 0.97U_{\mathrm{exp}}$, $I_{\mathrm{sim}} = 0.87I_{\mathrm{exp}}$, $\Delta_{\mathrm{sim}} = \Delta_{\mathrm{exp}} + 1\,\mathrm{MHz}$, $T = 140\,\mu\mathrm{K}$.

From the recorded data and its agreement with the Monte Carlo simulation, we conclude that for optical dipole traps with weak confinement (e.g. in running wave traps), the effect of the DFF is not visible and can be neglected. However, in traps with tight confinement (e.g. in deep standing wave lattices), the DFF can lead to strong heating effects much larger than the photon recoil heating. This is an important finding which indicates that for weak resonant illumination the mean number of photons that an atom can scatter before it is lost cannot be arbitrarily increased by using deeper traps and, indeed, it reduces for very deep traps

Even though the DFF limits the number of photons that can be scattered from the weak field at resonance by a trapped atom, in the next section we will show that the effect of the DFF can be suppressed by choosing adequate parameters for the NRF.

3.2 Heating induced by off-resonant illumination

When the illumination beam is not weak and resonant ($\Omega_{\mathrm{NR}} \not\ll \Gamma$), then the internal and external degrees of freedom cannot be decoupled as in the previous section, and the simple absorption and emission picture is not valid anymore. One way to include the coherent coupling between the atom and the NRF is to consider the dressing effect induced by this field in addition to the dipole trap dressing. However, dressing a two-level atom simultaneously by two light fields is mathematically complex problem [103]. In order to describe the system in a simple way, the same approximations as in Sec. 3.1.1 can be made, i.e. we assume that the effect of the dipole trap is reflected only as a position-dependent AC-Stark shift for the atomic transition and, therefore, we use the same Hamiltonian in Eq. (3.3) to describe the system.

3.2.1 Additional dressing by a near-resonant field

To study this problem, first we find the NRF-dressed state basis. To this end, we diagonalize the Hamiltonian in Eq. (3.3), which spanned in the bare state basis $\{|\tilde{g}, N_{\mathrm{NR}}\rangle, |\tilde{e}, N_{\mathrm{NR}} - 1\rangle\}$ has a matrix form

$$\hat{\mathbf{H}} = \hbar \begin{bmatrix} N_{\mathrm{NR}}\omega_{\mathrm{NR}} + \frac{U_g(\mathbf{r})}{\hbar} & \frac{\Omega_{0,\mathrm{NR}}}{2} \\ \frac{\Omega_{0,\mathrm{NR}}}{2} & N_{\mathrm{NR}}\omega_{\mathrm{NR}} - \left(\Delta_{\mathrm{NR}} - \frac{U_e(\mathbf{r})}{\hbar}\right) \end{bmatrix}, \tag{3.15}$$

where $\Delta_{\mathrm{NR}} = \omega_{\mathrm{NR}} - \omega_0$ is the detuning of the NRF from the atomic transition of the untrapped atom. The eigenstates for (3.15) are

$$\begin{aligned} |+, N_{\mathrm{NR}}\rangle &= \sin(\theta_{\mathrm{NR}}(\mathbf{r}))\,|\tilde{g}, N_{\mathrm{NR}}\rangle + \cos(\theta_{\mathrm{NR}}(\mathbf{r}))\,|\tilde{e}, N_{\mathrm{NR}} - 1\rangle, \\ |-, N_{\mathrm{NR}}\rangle &= \cos(\theta_{\mathrm{NR}}(\mathbf{r}))\,|\tilde{g}, N_{\mathrm{NR}}\rangle - \sin(\theta_{\mathrm{NR}}(\mathbf{r}))\,|\tilde{e}, N_{\mathrm{NR}} - 1\rangle, \end{aligned} \tag{3.16}$$

where the mixing angle is defined by

$$\begin{aligned} \tan(2\theta_{\mathrm{NR}}(\mathbf{r})) &= -\frac{\Omega_{0,\mathrm{NR}}}{\Delta_1(\mathbf{r})}, \qquad 0 \le \theta_{\mathrm{NR}} < \pi, \\ \Delta_1(\mathbf{r}) &= \Delta_{\mathrm{NR}} + \frac{U_g(\mathbf{r}) - U_e(\mathbf{r})}{\hbar}. \end{aligned} \tag{3.17}$$

$\Delta_1(\mathbf{r})$ represents the total detuning of the NRF at position $\mathbf{r}$ that takes into account the AC-Stark shift induced by the dipole trap (see Fig. 3.3a). The eigenenergies corresponding to the new dressed states in

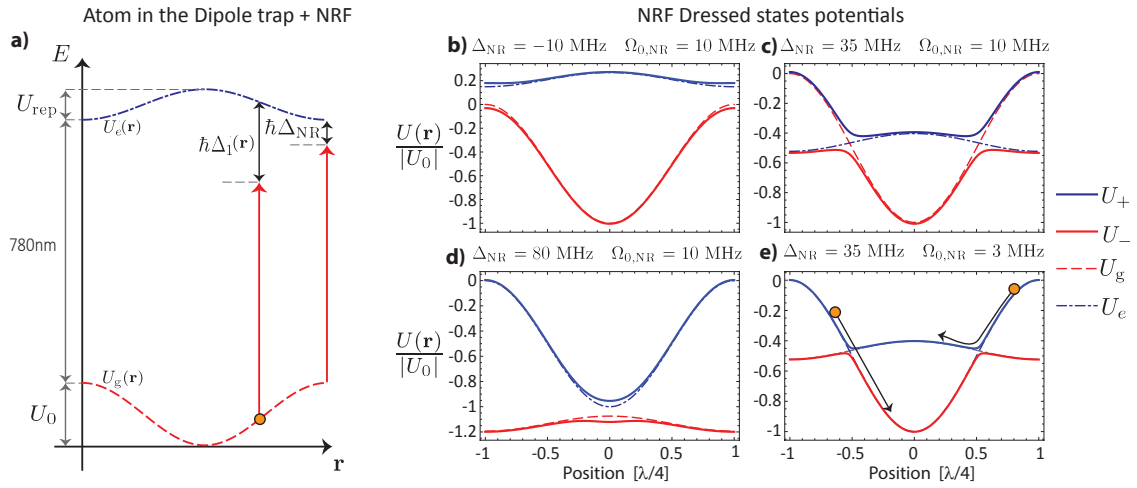

Figure 3.3. *Dressing by a near-resonant field.* **a)** Two-level atom in the dipole trap. **b)** NRF-dressed states potentials (solid lines) and DT-potentials (dashed lines) for red-detuning. **c)** Same as **b** but for a NRF resonant at $\lambda/4 = \pm 0.5$ where an anti-crossing is present. **d)** Same as **b** but for Blue-detuning for the NRF. **e)** Same as **c** but for weaker NRF. Adiabatic (right arrow), and non adiabatic (left arrow) following trajectories. In all plots $U_0 = 3.46\,\mathrm{mK}$ and $U_{\mathrm{rep}} = 0.4\,\mathrm{mK}$.

Eq. (3.16) are

$$\begin{aligned} E_{\pm,\mathrm{NR}} &= N\hbar\omega_{\mathrm{NR}} + U_g(\mathbf{r}) + \frac{\hbar}{2}\left(-\Delta_1(\mathbf{r}) \pm \Omega_{\mathrm{NR}}(\mathbf{r})\right), \\ \Omega_{\mathrm{NR}}(\mathbf{r}) &= \sqrt{\Delta_1^2(\mathbf{r}) + \Omega_{0,\mathrm{NR}}^2}, \end{aligned}$$

where $\Omega_{\mathrm{NR}}(\mathbf{r})$ is the generalized Rabi frequency. We can now identify the potentials for the NRF-dressed states

$$U_\pm(\mathbf{r}) = U_g(\mathbf{r}) + \frac{\hbar}{2}\left(-\Delta_1(\mathbf{r}) \pm \Omega_{\mathrm{NR}}(\mathbf{r})\right). \tag{3.18}$$

For large detunings (red or blue) the NRF-dressed state potentials are almost identical to the bare state potentials (see Fig. 3.3b,d), but close to the resonance an anti-crossing is present and it strongly modifies the curvature of the potential (see Fig. 3.3c,e).

3.2.2 Transient regime and the role of dressed state coherences

In the description of the NRF-dressed-states above, from now on just referred to as *Dressed States* (DS), the effect of spontaneous decay has so far not been included. Even though the DS are the eigenstates of the Hamiltonian in Eq. (3.3), when an atom decays due to the spontaneous emission of a photon, it is projected to ground state $|\widetilde{g}, N_{\mathrm{NR}}\rangle$. First, let us have a look into the implications of this projection.

For the sake of argument we assume, for a short moment, that there is no position dependence in the detuning $\Delta_1(\mathbf{r}) = \Delta$. We start our analysis with an atom that has spontaneously decayed at $t = 0$;

therefore, the initial state of the system is $|\psi(t=0)\rangle = |\widetilde{g}, N_{\mathrm{NR}}\rangle$, after a finite time t the state evolves and it is described by a superposition of both DS given by

$$|\psi(t)\rangle = \sin\theta_{\mathrm{NR}}\,|+, N_{\mathrm{NR}}\rangle\, e^{-i\frac{\Omega_{\mathrm{NR}}t}{2}} + \cos\theta_{\mathrm{NR}}\,|-, N_{\mathrm{NR}}\rangle\, e^{i\frac{\Omega_{\mathrm{NR}}t}{2}}. \tag{3.19}$$

In the special case of resonance, $\Delta = 0$ one recovers the usual Rabi flopping. For the non-resonant case, only one of the dressed states dominants the superposition in Eq. (3.19), which translates into the fact that full population transfer between $\widetilde{g}$ and $\widetilde{e}$ is not possible. The continuous evolution of the state in Eq. (3.19) relies on the fact that the coherence between the two dressed states is maintained. However, this is not the case for arbitrary large times. The coherence is maintained just for a small transient time until the system reaches its steady state, which is one of the DS, and after this time all coherences are damped.

Here an interesting problem appears. When an atom is in either of the dressed-states, then the dynamics is dictated by its well-defined potential, e.g. if the system is in the state $|+, N_{\mathrm{NR}}\rangle$, the dynamics is described by the potential U_+. However, during the transient regime, an atom is in a superposition of DS and it experiences two different forces. While the first term on the right side in Eq. (3.19) is subjected to the potential U_+ the last term is affected by U_-, leading to a splitting of the wave-packet. One possible way to model the dynamics of this system is by using quantum trajectories and quantum jump methods [104–106], which have proven to be useful in describing the dynamics of an atom in a state-dependent potential under near-resonant illumination [99]. However, these techniques are not directly applicable to our system since a delocalization of the wave-packet is not considered in these methods. This effect complicates the analysis of this problem and a numerical implementation of the full quantum mechanical description of the 3D system becomes computationally challenging and, we do not know of any numerical method that can reduce the computational complexity of the problem.

Even though an exact solution for this problem is difficult to obtain, if the secular approximation is fulfilled (large detunings or intense fields), then the decay time for the coherences is much faster than the motional dynamics in the trap and the effect the wave-packet splitting can be neglected. This will be addressed in the next section.

3.2.3 Reduction to rate equations

We start by describing the system using the Optical Bloch Equations (OBE) in the dressed-state basis. A general description in this basis, however, turns out to be more complicated than for the bare state case. Fortunately, in the secular limit, $\Omega_{\mathrm{NR}} \gg \Gamma$, the OBE in the DS basis can be written in a relatively simple form [71]

$$\dot{\rho}_{++} = -\Gamma_{+-}\rho_{++} + \Gamma_{--}\rho_{--}, \tag{3.20a}$$

$$\dot{\rho}_{--} = -\Gamma_{--}\rho_{--} + \Gamma_{+-}\rho_{++},$$

$$\dot{\rho}_{+-} = -\left(i\Omega_{0,\mathrm{NR}} + \Gamma_{\mathrm{coh}}\right)\rho_{+-}, \tag{3.20b}$$

$$\Gamma_{\mathrm{coh}} = \Gamma\left(\frac{1}{2} + \cos^2\theta_{\mathrm{NR}}\sin^2\theta_{\mathrm{NR}}\right). \tag{3.20c}$$

Here $\rho_{ij} = \sum_N \langle i, N_{\mathrm{NR}}| \rho |j, N_{\mathrm{NR}}\rangle$, where $i \in \{+, -\}$ are the reduced populations and coherences, and the transition rates[3] between the dressed states are given by

$$\Gamma_{++} = \Gamma \sin^2 \theta_{\mathrm{NR}} \cos^2 \theta_{\mathrm{NR}}, \tag{3.21a}$$

$$\Gamma_{-+} = \Gamma \sin^4 \theta_{\mathrm{NR}}, \tag{3.21b}$$

$$\Gamma_{+-} = \Gamma \cos^4 \theta_{\mathrm{NR}}, \tag{3.21c}$$

$$\Gamma_{--} = \Gamma \sin^2 \theta_{\mathrm{NR}} \cos^2 \theta_{\mathrm{NR}}. \tag{3.21d}$$

In Eqs. (3.20), Γ_{coh} represents the decay rate for the coherences of the DS. If the time it takes for the coherences to decay is much smaller than the time an atom needs to move a significant distance, then we can assume that the coherences decay instantaneously at every position and hence, they do not play an important role. For a one-dimensional standing wave, this condition reduces to

$$4\omega_{\mathrm{axial}} \ll \Gamma \left(\frac{1}{2} + \cos^2 \theta_{\mathrm{NR}} \sin^2 \theta_{\mathrm{NR}} \right). \tag{3.22}$$

The factor of 4 comes from the fact that for a quarter of the oscillation period, the atom has moved from the top to the bottom of the trap. Condition in Eq. (3.22) is very restrictive since, for ^{87}Rb in a standing wave potential, it is fulfilled only for traps with an oscillation frequency $\omega_{\mathrm{axial}} \ll \frac{\Gamma}{8} = 2\pi \times 0.76\,\mathrm{MHz}$ which imposes a strong limitation on the trap depth.

A second mechanism that reduces the influence of the coherences is the fact that Eqs. (3.20) do not couple coherences and populations. This means that if at $t = 0$ one of the next conditions is satisfied

$$|\rho_{\pm\mp}(t = 0)| \ll \rho_{++}, \tag{3.23a}$$

$$|\rho_{\pm\mp}(t = 0)| \ll \rho_{--}, \tag{3.23b}$$

then it is satisfied at every time and the effect of coherences can be always neglected.

We can rewrite Eq. (3.23) in a slightly different way by estimating the contribution of each dressed state in the superposition created after the spontaneous emission of a photon described by Eq. (3.19). To this end we define

$$D(\mathbf{r}) = 1 - \left| \cos^2 \theta_{\mathrm{NR}}(\mathbf{r}) - \sin^2 \theta_{\mathrm{NR}}(\mathbf{r}) \right|. \tag{3.24}$$

This quantity measures the contribution of each dressed state in Eq. (3.19), $D = 1$ means that both terms contribute equally (50-50 superposition), and $D = 0$ means that only one term is present. Using the definition for $D(\mathbf{r})$, inequalities (3.23) can be rewritten as

$$D(\mathbf{r}) \ll 1. \tag{3.25}$$

The latter condition must be satisfied in addition to the secular approximation $\Gamma \ll \Omega_{\mathrm{NR}}(\mathbf{r})$. If these conditions are fulfilled, then the effect of the coherences can be neglected and the problem is reduced to a set of rate equations described by Eq. (3.20). Therefore, we can model the dynamics of the system as a set of quantum jumps between the dressed states where each jump is accompanied by the emission and absorption of a photon from the NRF and the external dynamics of the atoms is determined by the dressed state potentials $U_{\pm}(\mathbf{r})$ in Eq. (3.18). This is schematically depicted in Fig. 3.4.

[3] The deduction for this equations is the same as described in Sec. 2.3.3.

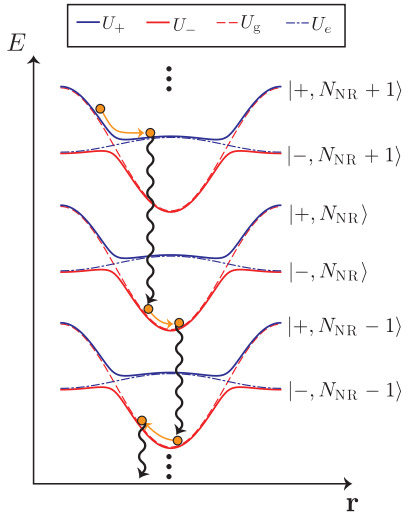

Figure 3.4. *Photon scattering in the near-resonant field dressed-states picture.* An atom is trapped in a dressed state potential and it jumps to another one by removing one photon from the near-resonant field and emitting it into free space.

The condition in Eq. (3.25) is fulfilled if and only if

$$\left|\frac{\Omega_{0,\mathrm{NR}}}{\Delta_1(\mathbf{r})}\right| \ll 1, \tag{3.26}$$

which means that the NRF must be always far-detuned with respect to the AC-Stark shifted transition.

3.2.4 Far detuning $\Omega_{0,\mathrm{NR}} \ll |\Delta_1(\mathbf{r})|, \Gamma \ll |\Delta_1(\mathbf{r})|$: suppression of the dipole force fluctuation

To understand the implications of the condition (3.26), let us consider a NRF with a large detuning with respect to the AC-Stark shifted resonance ($\Omega_{0,\mathrm{NR}} \ll |\Delta_1(\mathbf{r})|, \Gamma \ll |\Delta_1(\mathbf{r})|$) which can be either red or blue, but keeping in mind that the atomic resonance is shifted at every position in the trap and the large detuning condition must be fulfilled for every position. If this is the case, then the dressed state potentials in Eq. (3.18) are

$$U_\pm(\mathbf{r}) \approx U_g(\mathbf{r}) + \frac{\hbar}{2}\left(-\Delta_1(\mathbf{r}) \pm |\Delta_1(\mathbf{r})| + \frac{\Omega_{0,\mathrm{NR}}^2}{2|\Delta_1(\mathbf{r})|}\right). \tag{3.27}$$

For the case of a red detuning ($\Delta_{\mathrm{NR}} < 0$), from Eq. (3.27) we obtain $U_- \approx U_g$ and $U_+ \approx U_e$, as illustrated in Fig. 3.3b. Using the Eq. (3.21) one finds the transition rate between the two dressed states.

$$\begin{aligned} \Gamma_{++} &\approx \Gamma\left(\frac{\Omega_{0,\mathrm{NR}}}{2\Delta_1(\mathbf{r})}\right)^2 & \Gamma_{-+} &\approx \Gamma\left(\frac{\Omega_{0,\mathrm{NR}}}{2\Delta_1(\mathbf{r})}\right)^4 \\ \Gamma_{+-} &\approx \Gamma, & \Gamma_{--} &\approx \Gamma\left(\frac{\Omega_{0,\mathrm{NR}}}{2\Delta_1(\mathbf{r})}\right)^2. \end{aligned}$$

In this case, the largest decay rate is Γ_{+-} and, therefore, most of the population is in state $|-, N_{\mathrm{NR}}\rangle$, in which the dominant decay is Γ_{--}. This is a very interesting effect. It indicates that in every scattering process the most probable scenario is that after the emission or absorption of a photon, the atom remains in the potential U_-, i.e. there is no change in the trapping force and hence no DFF.

For a NRF that is always blue detuned, all the results are the same as for the red case, but the role of the

dressed states is interchanged, i.e., $U_- \approx U_\mathrm{e}$ and $U_+ \approx U_\mathrm{g}$ and the subscripts of the decay rates must be exchanged $+ \leftrightarrow -$.

3.2.5 Landau-Zener crossings

If the NRF is resonant with the AC-Stark shifted atom at some position inside the trap, then avoiding crossings appear (see Fig. 3.3c). When the detuning $\Delta_1(\mathbf{r})$ is swept slowly across the resonance (and natural decay is ignored), the atom remains in its initial DS and follows its respective potential. However, for higher motional speeds, the atom can make a transition to the other dressed state in a non-adiabatic way, this situation is illustrated in Fig. 3.3e. The probability P_NA that an atom does not follows adiabatically an avoided crossing was calculated by Landau [107], Zener [108], and Stückelberg [109], and can be written in general as [110]

$$P_\mathrm{NA} = \exp\left(-\frac{\pi\Omega_0^2}{2\left|\frac{\partial}{\partial t}\Delta\right|}\right) \tag{3.28}$$

where Ω_0 is the resonant Rabi frequency, and the derivative over time represents the sweep speed of the detuning Δ. The atom's motion in the trap sweeps the NRF frequency through the resonance and the speed of the sweep is directly related to the speed of the atom. To calculate the maximum non-adiabatic population transfer, we consider an atom moving with its maximum speed, i.e., $U_\mathrm{Kinetic} = U_0$. We can then find an upper bound for the time derivative in Eq. (3.28) and write an upper limit for the probability of non-adiabatic transfer

$$P_\mathrm{NA} \leq \exp\left(-\frac{\pi\Omega_{0,\mathrm{NR}}^2}{2\Delta_\mathrm{max}\omega_\mathrm{axial}}\right). \tag{3.29}$$

Here Δ_max denotes the maximum AC-Stark shift induced by the dipole trap and ω_axial is the trap's axial frequency.

The potential for the DS for a set of experimentally accessible parameters is illustrated in Fig. 3.3c. These are $\Omega_{0,\mathrm{NR}} = 2\pi \times 10\,\mathrm{MHz}$, $\Delta_\mathrm{NR} = 2\pi \times 35\,\mathrm{MHz}$, $\omega_\mathrm{axial} = 2\pi \times 0.9\,\mathrm{MHz}$. For these parameters the maximum non-adiabatic transfer is less than 10%. However, when the strength of the NRF is reduced to $\Omega_{0,\mathrm{NR}}/2\pi = 3\,\mathrm{MHz}$ (see Fig. 3.3e) this bound is 80%, meaning that non-adiabatic crossings are not negligible any more.

3.2.6 Experimental implementation

To experimentally explore the heating induced by the interaction with the NRF, we perform measurements for a range of parameters for the NRF. The experimental sequence and setup are the same as described in Sec. 3.1.3 with few differences. Here the trap depth is adiabatically set to 3.46 mK, and for this value, two sets of data were recorded. First, for 8 different frequencies from $\Delta_\mathrm{NR}/2\pi = -12\,\mathrm{MHz}$ to $+39\,\mathrm{MHz}$ using a NRF with an intensity of $4\,I_\mathrm{sat}$ and illumination times from 1 to 10 ms in steps of 1 ms; the second set of data was recorded for 11 different frequencies from $\Delta_\mathrm{NR}/2\pi = +38\,\mathrm{MHz}$ to $+132\,\mathrm{MHz}$ and illuminations times from 1.5 to 15 ms in steps of 1.5 ms with an intensity of $0.6\,I_\mathrm{sat}$ for the NRF. The results of the measurement are shown in Fig. 3.5.

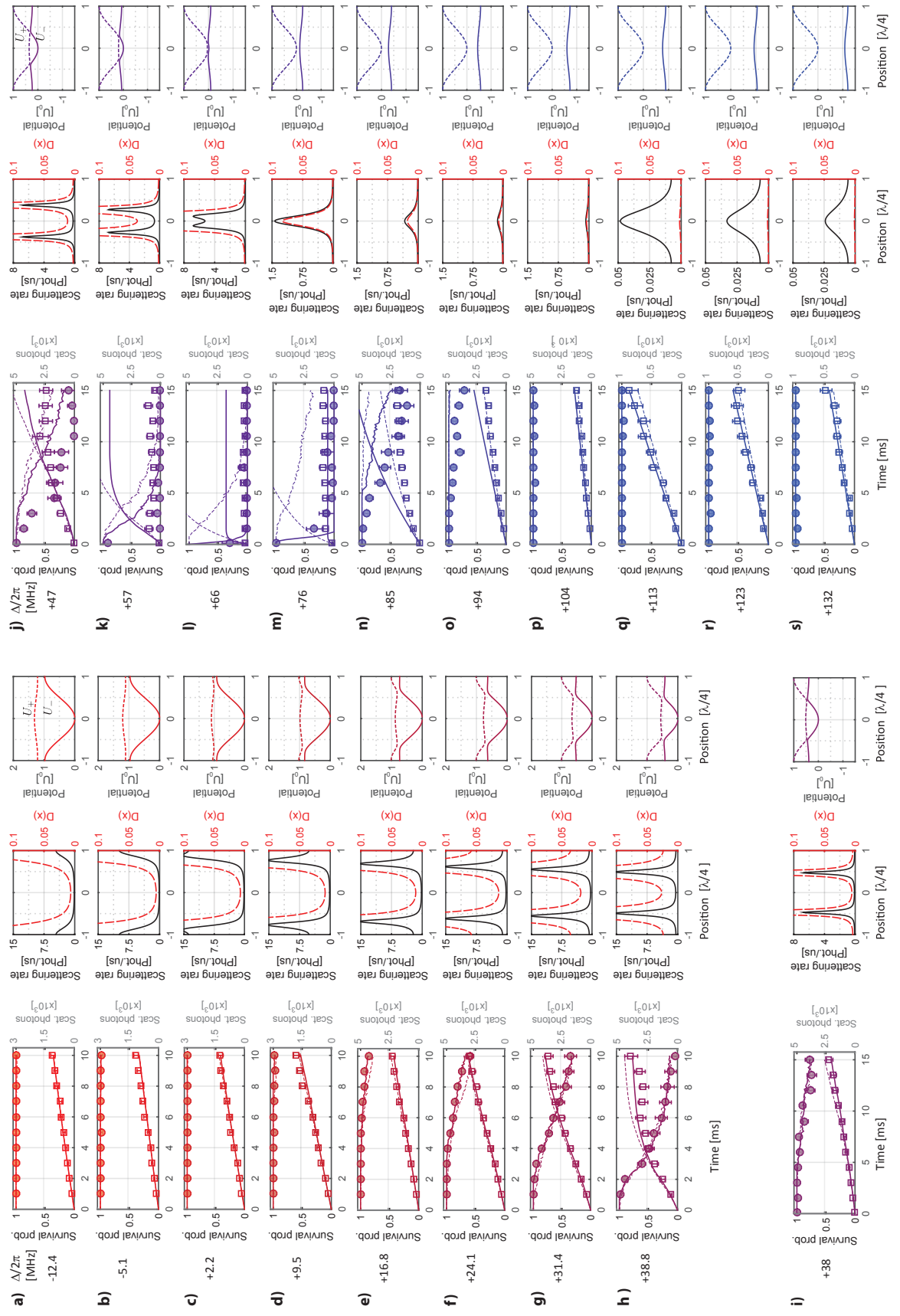

Figure 3.5. *Photon scattering and atom survival for different illuminations.* **a)-h)** Using $\Delta_{\mathrm{NR}}/2\pi = -12$ to $+39$ MHz, and $I_{\mathrm{NR}} = 4I_{\mathrm{sat}}$. **i)-s)** For $\Delta_{\mathrm{NR}}/2\pi = +38$ MHz to $+132$ MHz using $I_{\mathrm{NR}} = 0.6I_{\mathrm{sat}}$. In each case three plots are shown. *Left:* survival probability (circles) and number of scattered photons (squares) as a function of time, and Monte Carlo simulation for the dressed state model (solid lines), and pure photon recoil model described in Sec. 3.1.3 (thin dashed lines). The error bars represent 95% confidence level. *Middle:* Total scattering rate (solid line) and the parameter $D(\mathbf{r} = (x, 0, 0))$, defined in Eq. (3.24), (long-dashed line). *Right:* Potentials for the dressed states $U_-(\mathbf{r} = (x, 0, 0))$ (solid line) and $U_-(\mathbf{r} = (x, 0, 0))$ (short-dashed line).

On top of the experimental data, two Monte Carlo simulations are presented. In the first simulation, the three-dimensional equation of motion is solved for the atoms in the DS potentials in Eq. (3.18). The jumps between the DS are chosen randomly according to the photon scattering rates in Eq. (3.21). For each scattering event a photon recoil is added in the same direction as the NRF (absorption) and another one in a random direction (emission) according to the dipole radiation distribution (for more details regarding the simulation see Appendix C). The second simulation considers just heating by recoil from photon absorption and emission as described in Sec. 3.1.3.

In the simulation some parameters were adjusted to best fit the data, but all of them within the experimental uncertainties. For the first set of data: $P_{\text{sim}} = 0.8\,P_{\text{exp}}$, $\Delta_{\text{sim}} = \Delta_{\text{exp}}$, $U_{0,\text{sim}} = 0.96\,U_{0,\text{exp}}$ and an initial temperature (in the deep trap) of $T = 140\,\mu\text{K}$. For the second set of data[4]: $P_{\text{sim}} = 0.83\,P_{\text{exp}}$, $\Delta_{\text{sim}} = \Delta_{\text{exp}} + 1\,\text{MHz}$, $U_{0,\text{sim}} = 0.96\,U_{0,\text{exp}}$ and $T = 140\,\mu\text{K}$. The reduction of the trap depth can be explained by the AC-Stark shift induced at different positions in the trap. It is estimated that the trap has a waist of $w_0 = 4.75\,\mu\text{m}$ and for the analysis of the experimental data we have used atoms in a region of $\pm 22\,\mu\text{m}$ around the center of the trap; at $22\,\mu\text{m}$ away from the center, the dipole trap spot size is $w' = 1.034 w_0$ which reduces the trap depth by $\sim 6\%$ at the sides.

In addition to the acquired experimental data, two more figures are included for each parameter. The first one shows the total scattering rate as a function of the position on the trap. In the same plot the parameter $D(\mathbf{r})$, defined in Eq. (3.25), is plotted. This parameter is presented here since it provides a criteria ($D(\mathbf{r}) \ll 1$) to determine in which cases the model used in the Monte Carlo simulation is valid. The second plot includes the DS potentials for the respective parameters.

For the first set of data (Fig. 3.5a-h), the simulation agrees well with the measurement, even though at some regions the condition (3.25) is not fulfilled. This agreement is mainly due to the fact that the atoms scatter most of the photons when they are at the bottom of the trap where $D(\mathbf{r}) \ll 1$.

In the second set of data (Fig. 3.5i-s), it is visible that for frequencies closer to resonance (expected at 79 MHz) the measurement strongly disagrees with the simulation (Fig. 3.5k-n). A disagreement is expected since the atoms scatter most of the photons at the bottom of the trap, where $D(\mathbf{r}) \approx 1$ invalidating the approximation used. As the frequency increases ($\Delta_{\text{NR}}/2\pi > 94\,\text{MHz}$), the value for $D(\mathbf{r})$ decreases and, as expected, the simulation shows a better agreement. In all cases where $D(\mathbf{r}) \ll 1$, the dressed state model is very close to the pure recoil model, which indicates that the DFF is suppressed (see Fig. 3.5a-i, p-s).

The strong heating observed close to the resonance is related to the DFF. In the measurement, we use an intensity of only $0.6\,I_{\text{sat}}$. In this regime it is expected that resonant scattering events lead to a change in the trapping potential. A Monte Carlo simulation using the weak resonant excitation model (described in Sec. 3.1) is shown in Fig. 3.6 focusing on the data close to resonance. It is clear that the DFF creates significant heating that can explain the observed losses. Even though the AC-Stark shifted resonance is expected at $\Delta/2\pi = 79\,\text{MHz}$[5], strong heating already occurs at $\Delta/2\pi = 66\,\text{MHz}$. Furthermore, at this point the weak resonant model, that predicts a strong DFF, agrees very well with the recorded data (see Fig. 3.5l).

For the experimental data shown in Fig. 3.6, most of the scattering events occur when Ω_{NR} is on the order of Γ and for this regime, we do not have a valid approximation . However, the models describing

[4] To record this data an extra AOM was added to increase the frequency scan and the data was recorded with five days difference.

[5] In the simulation we have used $U_{\text{sim}} = 0.96 U_{\text{exp}}$ therefore according to the simulation the resonance is expected at $\Delta/2\pi = 75\,\text{MHz}$.

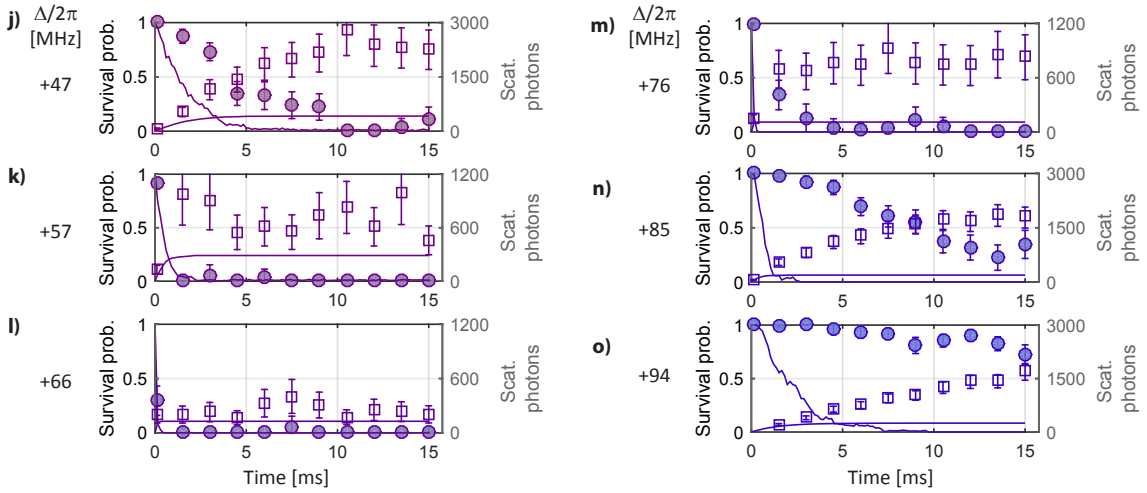

Figure 3.6. *Photon scattering and atom survival for near-resonant illumination.* **j-o)** Survival probability (circles), number of scattered photons (squares) and Monte Carlo simulation (solid lines) close to the AC-Stark shifted resonance at the bottom of the trap (~ 79 MHz) using the weak resonant illumination model (see Sec. 3.1.3). The error bars represent 95% confidence level. The same experimental data is shown in Fig.3.5 with the same indices.

two different regimes can be used for a qualitative understanding of this scenario and explain why strong heating occurs when the NRF is slightly red-detuned and not only on resonance with the AC-Stark shifted atom.

On the one hand, assuming that every scattering event changes the trapping potential (weak resonant model), Eq. (3.10) indicates that the largest amount of heating occurs for scattering at the bottom of the trap; on the other hand, only near-resonant events change the trapping potential. If the NRF is resonant at the bottom of the trap, then an atom is only resonantly excited at the center of the trap. But when the atom is hot, it spends more time close to its turning points (far from the center), where it can off-resonantly scatter a photon without changing the trapping potential. However, when the NRF is resonant slightly to the side of the center (see e.g. Fig. 3.5l), then there are two resonant points in the trap and, therefore, the time that an atom interacts with resonant light increases, leading to higher chance of a resonant excitation close to the center, where the heating is maximized. For this reason, strong heating is observed for $\Delta/2\pi = 66\,\text{MHz}$ while for $\Delta/2\pi = 85\,\text{MHz}$ is not.

From the experimental data and the simulations presented in Figs. 3.5 and 3.6, we conclude that heating dynamics of an atom interacting with an illumination beam that is near-resonant with the AC-Stark shifted atom at the bottom of the trap the is a mixture of different types of scattering, some events change the trapping force while others only create heating by photon recoil. However, as discussed in this chapter, a full quantitative description in this regime must consider the effect of the coherences for the dressed states, as well as the non-adiabaticity of the Landau-Zener crossing, which so far have been neglected.

3.3 Summary and conclusion

We have explored the heating dynamics of a neutral atom trapped in a standing wave dipole trap illuminated with a near-resonant field. A theoretical description and its experimental implementation were provided for two different regimes:

- For a weak near-resonant beam, $\Omega_{\mathrm{NR}} = \sqrt{\Omega_{0,\mathrm{NR}}^2 + \Delta_{\mathrm{NR}}^2} \ll \Gamma$, we have shown that for deep traps the fluctuations of the dipole force leads to strong heating. This heating is well described by a series of quantum jumps between the trapping and the anti-trapping potentials induced by the dipole trap. Theoretical and experimental results show that for deep traps, the number of photons that an atom scatters before it is expelled from the trap decreases with an increasing trap depth. This effect sets a limit on the deepness of the trap, and therefore, to the maximum amount of scattered photons.
- For an off-resonant field, $\Omega_{\mathrm{NR}} = \sqrt{\Omega_{0,\mathrm{NR}}^2 + \Delta_{\mathrm{NR}}^2} \gg \Gamma$, the illumination light creates an additional dressing to the optically trapped atom. In this case, Eq. (3.25) provides a condition in which the effect of the coherences between the double dressed states is negligible. In this regime, the dynamics of a trapped atom is well described by series of quantum jumps between the dressed state potentials. Moreover, for the case of a large detuning, $|\Delta_1(\mathbf{r})| \gg \Gamma$ the quantum jumps do not change the trapping potential leading to a strong suppression of the DFF. This result is independent of the trap depth and, therefore, atoms trapped in deep potentials scatter more photons before they are lost since the only source of heating is the recoil by the photon absorption and emission processes.

The settings for the illumination light that allows the scattering of a large number of photons by an optically trapped atom, provided in this chapter, are of a particular relevance when it is necessary to obtain knowledge from a confined atom by near-resonance fluorescence. It provides a tool to retrieve information from the system generating just a small amount of heating, this of particular interest in the next chapter.

CHAPTER 4

Non-destructive and spatially-resolved internal state detection of neutral atoms

The prospect of quantum information science to solve tasks that are out of reach for classical information technology has motivated impressive efforts in the field of physics over the last two decades. Trapped atomic particles are arguably among the most advanced physical platforms that are currently considered for quantum information devices. Pioneering experiments with trapped ions, for example, have opened up the field of few-body quantum simulation [111–113] and computation [114] by making use of a high-fidelity quantum optics toolbox for state preparation, single and many-qubit gates and state detection [89]. In order to increase the size of atomic quantum devices from its current limit on the order of 10 qubits, the scalability of all aspects of atomic qubit control will be crucial.

One of the promising candidates for systems with hundreds of qubits and beyond are arrays of optically trapped neutral atoms. Based on the favorable scaling properties of light potentials [115] and the possibility to optically address individual atoms through high-resolution microscopes [21, 22], an increasing number of techniques are explored with the goal of a complete quantum optics toolbox for scalable quantum information science with neutral atoms. The studied capabilities include the deterministic filling, operation of parallel quantum gates [116] and single site manipulation of atoms in standing wave lattices as well as the controlled loading [23, 30, 117], lossless (re-)cooling, and two-atom quantum gates in dipole traps and optical microtrap arrays.

The simultaneous and non-destructive readout of many atomic qubits is another essential feature that is needed for scalable quantum information science based on neutral atoms. In the past, spatially resolved state detection of many atoms has relied on a technique [39] where atoms in one quantum state are intentionally pushed out from the optical trap by resonant light. Although this method can achieve high fidelities for large arrays of neutral atoms, it is intrinsically destructive and, therefore, inefficient in quantum information routines. Efficient readout without losing atoms from their optical trap potential has previously been achieved for atoms coupled to high-finesse optical cavities [40–42]. More recently non-destructive readout has been demonstrated for single atoms in optical traps using state-selective fluorescence detection in free-space [43, 44].

This chapter is divided into two parts. Sec. 4.1 presents the experimental implementation and characterization of the non-destructive state detection of ^{87}Rb atoms trapped in an optical lattice by using near-resonance state-dependent fluorescence. In Sec. 4.2, the information of the experimental system is added in order to estimate the internal state of an atom in an optimal manner by Bayesian methods.

This information includes the properties of the imaging system, the EMCCD characteristics and the statistics of the photon scattering process. Finally, I show that the Bayesian methods developed in this work represent a scalable method that can be extended for systems containing a large number of atoms in one and two-dimensional optical lattices.

4.1 Hyperfine state readout by resonance fluorescence

To determine the internal state of an atom that has two well-separated ground states, we can use resonant illumination which addresses only one ground state. During the illumination process, one state appears *bright* (it scatters photons) while the other remains *dark* (it does not scatter photons). If an ideal photon detector is used, the detection (or no detection) of a photon provides information on the internal state.

In reality, photon detectors are not ideal and there is always background noise present, which can lead to confusing an atom in the dark state as being bright. In addition, the Poissonian nature of the photons emitted by an atom in the bright state creates an uncertainty in the number of detected counts. These effects, among others, broaden the distribution of the detected counts from atoms in any of these states. For a high-fidelity state-determination, it is necessary that the distribution of detected counts for both states are statistically well separated. This state detection scheme is widely used for trapped ions reaching very high fidelities [89].

Our goal is to implement such a state detection scheme to distinguish between the two hyperfine ground states, $F = 1$ and $F = 2$, of ^{87}Rb with a high fidelity. For alkali atoms, unlike trapped ions, there is no electron shelving technique that protects against undesired state transfer, which makes the implementation of a state detection based on resonance fluorescence more challenging. The idea behind our implementation is to use illumination near-resonant with the transition $F = 2 \rightarrow F' = 3$ [43, 44]. In this case, an atom in the state $F = 2$ is bright while an atom in the state $F = 1$ is dark.

In addition to the high fidelity requirement, we impose the condition that the atoms remain trapped in the optical lattice after the state readout. As shown in Chap. 3, the amount of energy imprinted by a photon onto an atom during the illumination process strongly depends on the parameters of the illumination light. Therefore, for an optimal state detection, it is necessary to find conditions of near-resonant illumination for which the count distributions for the bright and dark states are well-separated and the heating induced by the illumination light is minimized.

In this section, we find optimal settings for the illumination light that allows for a high-fidelity and non-destructive state detection. Sec. 4.1.1 presents the experimental characterization of different effects that create an undesired state transfer and how they are suppressed. In Secs. 4.1.2 and 4.1.3 we find the settings for the illumination light that fulfills the required conditions for a non-destructive state detection. Finally, Sec. 4.1.4 presents a quantitative analysis of the detection fidelity.

4.1.1 Improving the cycling transition: reducing the transfer to a dark state

Using molasses illumination, an atom can be cooled in the optical lattice. For the molasses configuration, six beams, which are detuned by Δ_{NR} to the transition $F = 2 \rightarrow F' = 3$, are used to reduce the energy in all spatial directions. The same configuration can be used, in principle, to determine the state of the atom

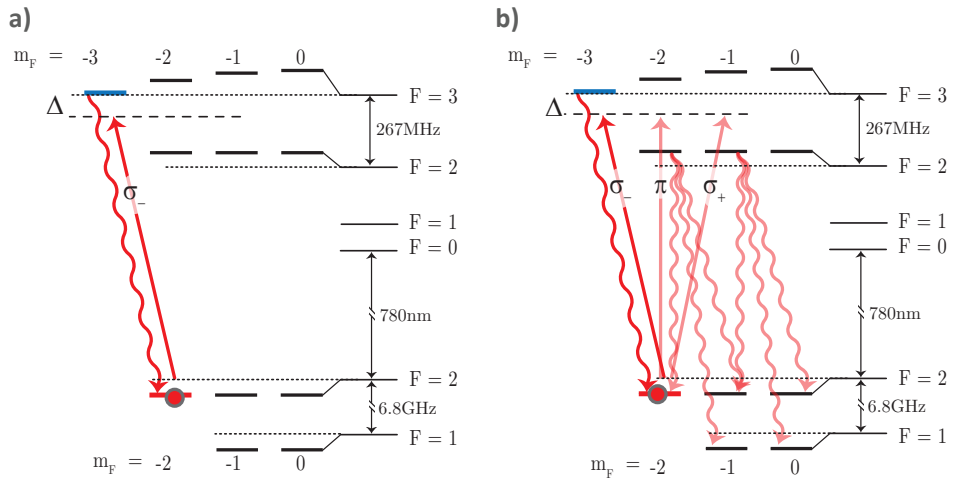

Figure 4.1. *Cycling transition for* ^{87}Rb. **a)** Ideal closed cycling transition for ^{87}Rb trapped in an optical dipole trap. Just the relevant hyperfine levels and part of the Zeeman spectrum are shown. **b)** Effect of polarization contamination on the closed transition

since the state $F = 2$ is bright and the state $F = 1$ is dark. However, the polarization of the molasses light is not well defined and there is a probability of exciting the atom to the state $F' = 2$ given by

$$P = \frac{\mathrm{R}_{\mathrm{sc},2\to2}(\Delta_{\mathrm{NR}})}{\mathrm{R}_{\mathrm{sc},2\to2}(\Delta_{\mathrm{NR}}) + \mathrm{R}_{\mathrm{sc},2\to3}(\Delta_{\mathrm{NR}})} \approx \frac{1}{2}\frac{1 + s + 4\Delta_{\mathrm{NR}}^2}{1 + s + 2(\Delta_{\mathrm{NR}} + \Delta_{\mathrm{sep}})^2 + 2\Delta_{\mathrm{NR}}^2}, \tag{4.1}$$

where $\Delta_{\mathrm{sep}} \approx 44\,\Gamma$ is the splitting between the excited states $F' = 2$ and $F' = 3$. For example, $\Delta_{\mathrm{NR}} = -4\Gamma$ leads to $P \approx 1/100$. This means that, on average, for every hundred scattering events, the atom is excited to the state $F' = 2$, from which it can decay to $F = 1$. This undesired state transfer limits the number of scattered photons and, therefore, the fidelity. The probability in Eq. (4.1) is minimized at resonance ($\Delta_{\mathrm{NR}} = 0$). However, this is not necessarily an optimum configuration for the illumination light since, as shown in Chap. 3, these settings can lead to strong heating in the trap and larger detunings are preferable.

The undesired population transfer can be reduced by using a well-defined circular polarization for the illumination light in order to drive just the cycling transition. Using this closed transition, excitations to the state $F' = 2$ are suppressed (see Fig. 4.1a). To create light that is circularly polarized, it is necessary to use a single illumination beam which propagates along a well-defined quantization axis.

Polarization purity is essential to drive a closed cycling transition. However, experimental imperfections, such as bad polarization or non-ideal magnetic or electric fields create polarization contamination that removes the atom from its cycling transition (see Fig. 4.1b). In our case, we use the cycling transition $F = 2, m_F = -2 \to F' = 3, m_{F'} = -3$ for which σ_- polarized light is required. Throughout this work, unless stated differently, I will always refer to this transition as the *cycling transition*.

Polarization circularity

Creation of circular light with high purity is experimentally challenging and, in practice, there is always a certain degree of ellipticity. Such ellipticity can be decomposed into two parts: the desired perfect circular light and a small component of opposite circularity, which contaminates σ_--polarized light with a σ_+ component for example.

To create σ - polarized light a laser beam is sent through a linear polarizer[1] and circular polarization is created by a set of $\lambda/4$, $\lambda/2$, $\lambda/4$ retarders. The light circularity is optimized by sending the light through a second linear polarizer and minimizing the intensity variation when rotating the second polarizer. After optimization of the retarder orientation, we determine[2] a ratio of $\sigma_+/\sigma_- \approx 1 \times 10^{-4}$.

Magnetic field axis alignment

The effect of polarized light on an atom is decided by the direction of the atom's quantization axis. This axis can be defined either by a bias magnetic field that breaks the degeneracy of the Zeeman manifold or by the electric field, i.e. the polarization, in the dipole trap. If the direction of propagation of the near-resonant light is not perfectly parallel with the quantization axis, it creates not only contamination of the opposite circularity but also a π-polarized component.

In the experimental setup, the quantization axis is created by a bias magnetic field along the z direction using the z compensation. Since the coil axes are not perfectly aligned with the propagation direction of the NRF, further adjustment of the magnetic field axis by the x and y compensation coils is required, which is optimized by the following procedure. A small number of atoms are loaded into a dipole trap with a depth of 1 mK and pumped into the state $F = 2, m_F = -2$. Then the σ_--polarized beam resonant with the transition $F = 2 \rightarrow F' = 2$ is turned on for 30 ms with an intensity of $0.7 I_s$. In this configuration, the state $F = 2,\ m_F = 2$ is a dark state, whereas any polarization impurity transfers the atoms to $F = 1$. This allows us to measure the number of transferred atoms after the illumination by using a push-out beam to remove the atoms that remain in state $F = 2$. The optimum values for the currents of the x and y compensation coils were experimentally optimized by minimizing the survival probability such that only 13(3)% of the atoms are transferred to $F = 1$. This corresponds to a fraction smaller than 1.3×10^{-3} of the total power in undesired polarization components. In a separate measurement, we have determined that the polarization is contaminated mostly by a π component. For details regarding this measurement see Appendix D.

Dipole trap and magnetic field misalignment

When a neutral atom interacts with two fields at the same time, it is important to align the fields in the same direction such that they give rise to a single well-defined quantization axis. For neutral atoms trapped in an optical dipole trap, it is convenient to use a bias magnetic field to define the quantization axis. When the atom is in its ground state, the magnetic field breaks the degeneracy of the hyperfine Zeeman levels, while the dipole trap creates a uniform AC-shift for all of them, therefore the magnetic field will define the quantization axis. However, for the excited state manifold of $F' = 3$, the dipole trap also breaks the degeneracy of the $m_{F'}$ states. Furthermore, the AC-Stark shift can be much larger than the

[1] CODIXX, IR 950 BC4 CW02.
[2] From the measured variation of the transmitted power when rotating the second polarizer.

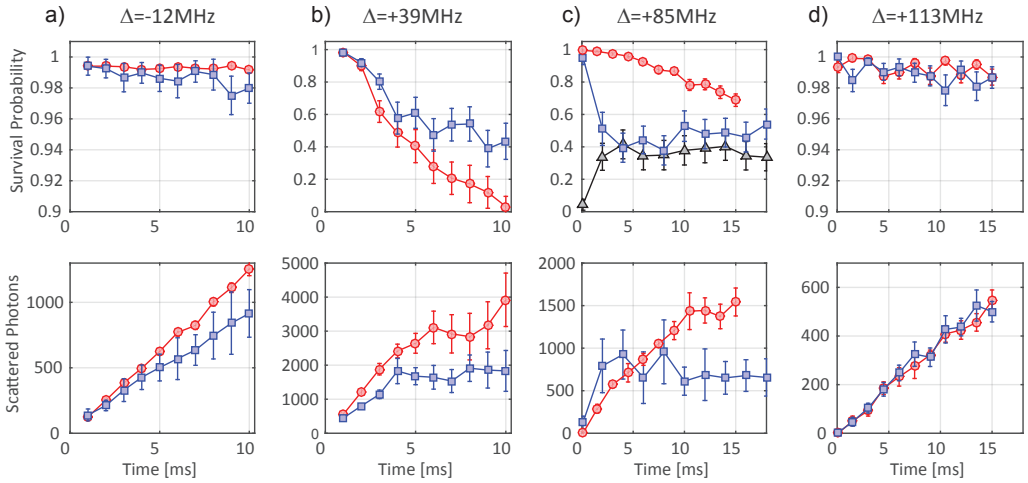

Figure 4.2. *Dipole trap tilt effect.* Survival probability and mean number of scattered photons for atoms illuminated for different times in the dipole trap. The blue squares are the measurement before the tilt correction and the red circles after the correction. The experimental data was acquired using different free-space detunings and intensities for the illumination beam. **a)** $\Delta/2\pi = -12\,\mathrm{MHz}$, $I = 4\,I_{\mathrm{sat}}$, **b)** $\Delta/2\pi = -39\,\mathrm{MHz}$, $I = 4\,I_{\mathrm{sat}}$, **c)** $\Delta/2\pi = 85\,\mathrm{MHz}$, $I = 0.6\,I_{\mathrm{sat}}$, **d)** $\Delta/2\pi = 113\,\mathrm{MHz}$, $I = 0.6\,I_{\mathrm{sat}}$. The top plot in **c** includes the survival probability when a push-out beam is applied after the interaction with the near-resonant field (black triangles).

Zeeman splitting induced by the bias magnetic field and in such case, the atomic energy eigenstates in the magnetic field basis do not necessarily correspond to the energy eigenstates in the dipole trap basis.

If the bias magnetic field is misaligned with the polarization of the dipole trap by an angle Θ, then any change from the ground to the excited state, leads to a mixture of the Zeeman sub-levels. For example, an atom that is excited to the state $|F', m_{F'}\rangle$ (in the magnetic field eigenbasis) can be expressed as a superposition of eigenstates in the dipole trap basis $|F'_{\mathrm{DT}}, m_{\mathrm{DT},F'}\rangle$

$$\left|F', m_{F'}\right\rangle = \sum_{-m_{\mathrm{DT},F'}}^{m_{\mathrm{DT},F'}} c_{m_{\mathrm{DT},F'},m_{F'}}(\Theta)\left|F', m_{\mathrm{DT},F'}\right\rangle .$$

The coefficients for the expansion are explicitly given in Ref. [110, 118]. Since the energy eigenstates of the excited atom are now defined by the dipole trap, the atom can decay from any state $|F'_{\mathrm{DT}}, m_{\mathrm{DT}}, F'\rangle$ with a probability $|c_{m_{\mathrm{DT},F'},m_{F'}}(\Theta)|^2$. This effect increases the undesired probability to transfer the atom to the dark state.

As expected from the theoretical arguments above, it was found experimentally that a misalignment of ~ 5 degrees on the dipole trap was related to an increased transfer rate into the dark state. This effect is more severe for illumination frequencies closer to AC-shifted resonance as can be seen from the set of measurements shown in Fig. 4.2. The experimental data was obtained by loading a few atoms into a trap with a depth of 3.46 mK depth (creating an AC-Stark shift of $2\pi\times 79\,\mathrm{MHz}$ at the bottom). The atoms are pumped to $F = 2, m_F = -2$ and a beam near-resonant with the cycling transition illuminates the atoms for different times.

In the data obtained for $\Delta/2\pi = 85\,\mathrm{MHz}$ before the correction of the tilt (blue squares in Fig. 4.2c), after

5 ms the number of scattered photons does not increase anymore and the survival probability remains constant, which indicates that the atom has been transferred to the dark state. This transfer to the dark state was verified by a separate measurement where a push-out beam is used after the near-resonant illumination to remove atoms in $F = 2$ (black triangles in Fig. 4.2c). The results from this measurement indicate that the atoms are indeed transferred to the state $F = 1$. After the correction of the tilted dipole trap, the effect was strongly reduced.

4.1.2 State-dependent fluorescence: experimental implementation and characterization

The improvement of the polarization purity reduces the undesired transfer of bright atoms to the dark state but this is just the first step towards a high-fidelity state detection. To achieve a high fidelity, it is necessary that the count distribution for the dark and bright states are well-separated. Ideally, to find optimum values for the NRF, it is necessary to record the count distribution for different illumination settings, which is experimentally demanding and, in practice, impossible. Nevertheless, if the undesired state transfer is neglected, to separate the count distributions it is sufficient to minimize the background noise and to increase the number of photons scattered by a bright atom. Therefore, as a first step, we use the mean number of scattered photons and the survival probability as figures of merit in order to find optimum values for the NRF.

To this end, a large range of frequencies for different illumination intensities of the NRF has been experimentally explored. Before describing the details of the experimental sequence, some of the most the relevant experimental settings are listed below:

- *EMCCD camera:* Usually only a few tens of photons are detected from an atom in the bright state. Therefore, it is important to reduce the electronic noise created in the detection process. For this reason, the camera is operated in *kinetic* and *external trigger start* mode[3]. In this operation mode, a trigger is sent to the camera, after which it acquires a series of N_{exp} images with an exposure time of 20 ms every 35 ms.

- *Reference image:* It is necessary to determine with high accuracy the position of atoms in the optical lattice. For this reason a high signal to noise Reference Image (RI) is required. The atoms are loaded in a trap with a depth of 1.5 mK and illuminated with an optical molasses. The illumination parameters are: $P_x = P_y = 21\,\mu\text{W}$, $P_z = 190\,\mu\text{W}$, free space detuning $\Delta/2\pi = -27$ MHz, repumper $F = 2 \rightarrow F' = 2$ with $P = 37\,\mu\text{W}$. The molasses also cools down the atoms to about 80 µK.

- *The near-resonant field:*. This single beam is used for the state readout. It is detuned from the transition $F = 2, m_F = -2 \rightarrow F' = 3, m_F = -3$ by a variable amount Δ. It is σ_- polarized along the z direction, which is defined as the quantization axis by a magnetic bias field of 1.5 Gauss (see Fig. 4.3). The power of the NRF is different depending on the chosen detuning. The beam has a waist of only 300 µm, which is ideal to reduce the required power in order to minimize stray light.

- *Imaging optics:* The atomic fluorescence is collected by the set of aspheric lenses together with the Porro prism (see Fig. 4.3) leading to a detection efficiency of $2.87^{+0.07}_{-0.32}\%$ (see Sec. 2.4.2). The images are created with a magnification that corresponds to 1.05 ± 0.01 pixel per lattice site.

[3] These settings lead to the lowest number of clock-induced charges, for more details see Ref. [82].

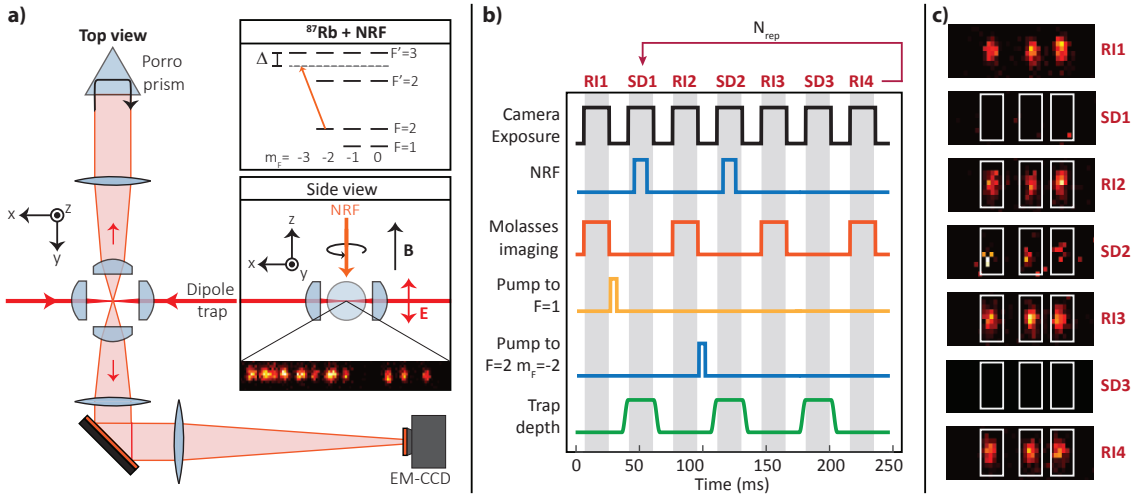

Figure 4.3. *State detection sequence.* **a)** Experimental setup and configuration of the near-resonant field (NRF). **b)** Simplified diagram of the sequence used to characterize the state detection. Reference images (RI) and state detection images (SD) are acquired alternately. **c)** Typical sequence of reference images and state detection images acquired with the EMCCD camera in one iteration of the experimental sequence.

Experimental sequence

With the parameters described above, we implement the following experimental sequence to record the number of emitted photons for atoms in the dark ($F = 1$) and bright ($F = 2, m_F = -2$) states for different settings of the near-resonant illumination. The experimental setup, as well as a schematic representation of the sequence, are presented in Fig. 4.3.

- Few atoms are loaded in the MOT and transferred into the dipole trap of 1.5 mK. To avoid strong variations of the atomic fluorescence due to the AC-Stark shift, a compression sequence is performed as described in Chap. 5 in order to place the atoms at the center of the trap. Then a trigger is sent to the camera and the image acquisitions starts.
- **RI1.** Reference image.
- **SD1.** The atom is optically pumped to the hyperfine state $F = 1$. The dipole trap depth is increased adiabatically to 3.46 mK in 5 ms. Then the NRF is turned on for a time t_{NR} while the camera is exposing then the dipole trap is lowered to 1.5 mK.
- **RI2.** Reference image.
- **SD2.** Same as in SD1 but now the atom is optically pumped to the hyperfine state $F = 2, m_F = -2$.
- **RI3.** Reference image.
- **SD3.** Same as in SD1 but in this case there is no optical pumping and the NRF remains off. This part of the sequence is used to characterize losses induced by the imaging process and technical fluctuations. It also serves as a true dark image where no light is detected by the camera.
- **RI4.** Reference image, then got back to step SD1

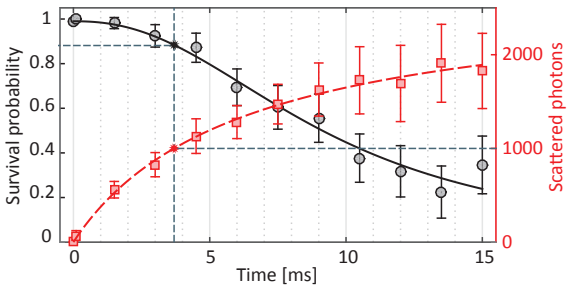

Figure 4.4. *Determination of survival probability for a given number of counts.* Measured survival probability (black circles) and mean number of scattered photons (red squares) for an atom in the bright state and $\Delta_{\mathrm{NR}}/2\pi = 85\,\mathrm{MHz}$. The solid and long-dashed lines are the phenomenological fits. The short-dashed straight lines exemplify the determination of the survival probability for 1000 scattered photons.

Two sets of data were recorded. The first set of data was recorded for 8 different frequencies from $\Delta_{\mathrm{NR}}/2\pi = -12\,\mathrm{MHz}$ to $+39\,\mathrm{MHz}$ using a NRF with an intensity of $4\,I_{\mathrm{sat}}$ and illumination times from 1 to 10 ms in steps of 1 ms. The second set of data was recorded for 11 different frequencies from $\Delta_{\mathrm{NR}}/2\pi = +38\,\mathrm{MHz}$ to $+132\,\mathrm{MHz}$ with an intensity of $0.6\,I_{\mathrm{sat}}$ and illuminations times from 1.5 ms to 15 ms in steps of 1.5 ms.

When the NRF illuminates an atom in the state $F = 1$, which is separated by $\Delta_{\mathrm{Hyp}}/2\pi = 6.8\,\mathrm{GHz}$ from $F = 2$, it will scatter a few photons at a rate

$$R_{\mathrm{sc}}(\Delta') = \frac{\Gamma}{2}\frac{s}{1 + s + 4(\Delta'/\Gamma)^2}, \tag{4.2}$$

where $\Delta' = \Delta_{\mathrm{NR}} + \Delta_{\mathrm{Hyp}}$. In the experiment, the frequency detuning Δ_{NR} was scanned 150 MHz, which has a negligible influence on the scattering rate in Eq. (4.2). Therefore, in the discussion below we focus just on the results for the bright state.

Determining the number of emitted photons and survival probability

To quantify the experimental results, we need to determine the number of emitted photons as well as the survival probability. To this end, we use only well resolved individual atoms. From the reference images (RI1, RI2, RI3 and RI4) the positions of the atoms are obtained. A ROI of 11×25 pixels is defined centered at the atom's position (see Fig. 4.3), in which we expect to collect 94% of incident photons. The number of counts contained in the ROI is integrated for the pictures corresponding to $F = 1$ and $F = 2$ (SD1 and SD2). If the atom's position changes by more than 2 pixels between the reference images, then it is considered that the atom has been lost. An example of the experimental outcome for $\Delta_{\mathrm{NR}}/2\pi = +85\,\mathrm{MHz}$ and $I = 0.6\,I_{\mathrm{sat}}$ is shown in Fig. 4.4. The complete set of results for the bright state has already been presented in Fig. 3.5 in Chap. 3.

4.1.3 Finding optimal parameters for the near-resonant field

From the measured set of data, we are interested on determining the parameters for which the highest state detection fidelity is achieved. This is equivalent to finding the settings where the largest number of photons is scattered while keeping a high survival probability. To this end, we fit a phenomenological

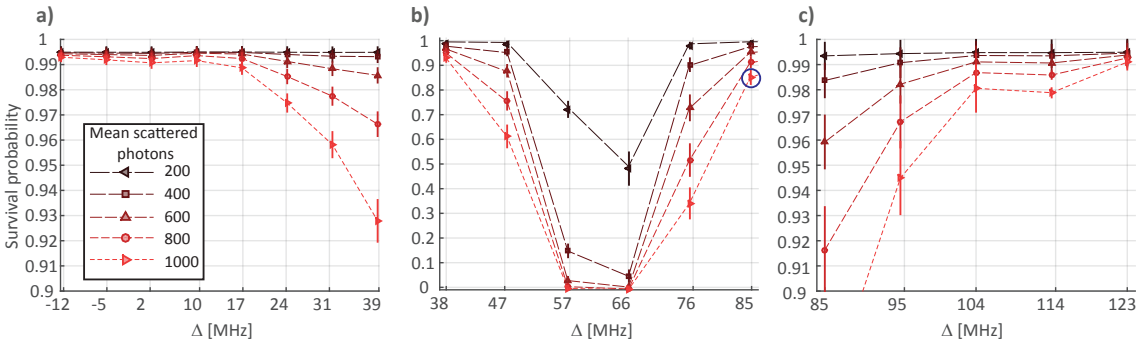

Figure 4.5. *Survival probability for a given number of detected counts for different frequencies.* Experimental data recorded using an illumination intensity of **a)** $4I_{sat}$ and **b-c)** $0.6I_{sat}$, except for the last point in **c** ($\Delta/2\pi = 123$MHz) where $1.9I_{sat}$ was used. The blue circle for $\Delta/2\pi = 85$MHz corresponds to the example shown in Fig. 4.4. The lines are a guide to the eye.

model[4] to the measured data and from the fit we determine the time it takes for an atom to scatter a given number of photons and the corresponding survival probability (see Fig. 4.4).

The fitting procedure described above was used to determine the survival probability after scattering a different number of photons for all the measured data (see Fig. 4.5). Close to the resonance ($\Delta_{Res}/2\pi = 79$MHz) the survival probability severely decreases, e.g. at $\Delta/2\pi = 66$ MHz, 95% of the atoms are lost after scattering just about 400 photons. However, for large detunings, either red or blue, it is possible to scatter a large number of photons without losing the atom. This is expected since for far detunings the dipole force fluctuation is negligible and thus, heating is reduced. Nevertheless, there are few differences between the red and blue-detuned case.

Red detuning. The atom starts at the bottom of the trap and as the atom is heated up, the turning points get closer to resonance creating a runaway heating process (see Fig. 4.6c for $\Delta/2\pi = -5$ MHz). Furthermore, the closer the atom gets to the resonance, the more significant the dipole force fluctuation becomes.

Blue detuning. The atom is closer to resonance when it sits at the bottom of the trap and as its temperature increases, it moves away from the resonance and, therefore, scatters fewer photons (see Fig. 4.6c for $\Delta/2\pi = +123$ MHz).

In both cases (red or blue detuning) it is convenient to choose a large detuning in order to reduce the dipole force fluctuation. However, there is an important difference between the two cases due to the fact that polarization contamination excites the transition $F = 2 \rightarrow F' = 2$ increasing the transfer probability to the dark state. The state $F' = 2$ is separated from $F' = 3$ by $\Delta_{sep} = 266$ MHz $+\Delta_{AC}$, where the last term is the AC-Stark shift induced by the dipole trap (see Fig. 4.6a). Detunings with the same magnitude, but opposite sign, lead to different excitation to the state $F' = 2$, according to

$$\frac{R_{sc}^{blue}(\Delta)}{R_{sc}^{red}(\Delta)} \approx \left(\frac{\Delta_{sep} - \Delta}{\Delta_{sep} + \Delta}\right)^2,$$

where Δ is the magnitude of the detuning and R_{sc} the scattering rate. Therefore, it is expected that blue detunings transfer less atoms to the dark state.

[4] To fit survival vs. time we use $f_1(t) = a\left(1 - \frac{t^n}{b+t^n}\right)$ and to fit scattered photons vs. time we fit $f_2(t) = \frac{at^n}{b+t^n}$ where a, b, n are fitting constants.

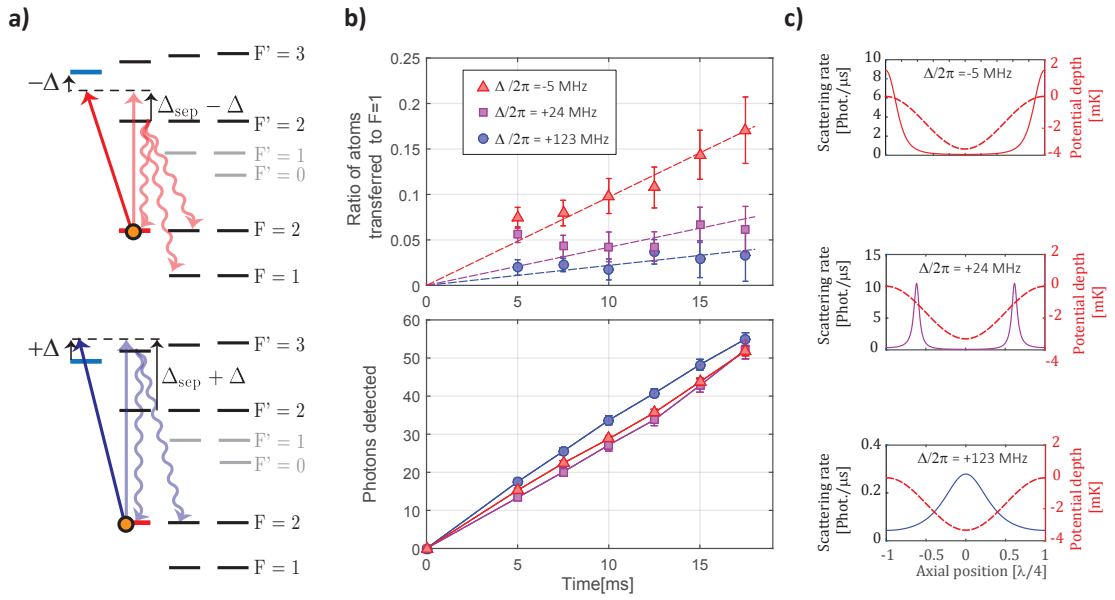

Figure 4.6. *Off-resonant pumping.* **a)** Atom excitation and main decay channels induced by π polarization contamination for red (top) and blue (bottom) detunings. **b)** Experimental data. The top plot shows the ratio of atoms transferred to $F = 1$ and the lower plot shows the number of detected photons, in both cases for three different detunings and different illumination times. The error bars represent 95% confidence intervals. **c)** Scattering rates (black solid lines) at each position of the traps for the chosen powers and detunings. The trapping potential is shown as a reference (red dashed line).

To experimentally quantify the number atoms transferred to the dark state ($F = 1$), atoms are prepared in the state $F = 2, m_F = -2$ in the dipole trap with a depth of 3.46 mK and illuminated with the NRF. After different illumination times, atoms in the state $F = 2$ are removed from the trap by the push-out technique and it is assumed that the remaining atoms were transferred to $F = 1$ by the illumination beam. This measurement was implemented for three different frequency detunings: $\Delta/2\pi = -5, +24$, and 123 MHz . The illumination intensities are chosen such that we detect the same number of photons after 17.5 ms, using $I/I_{\text{sat}} = 3.7,\ 1.2,$ and 3.2 respectively. From the measurement we observe that, as expected, the transfer to the dark state is minimized for blue detuning, e.g. at 10 ms for blue detuning we detect more photons than for the red case and the transfer to the dark state is always lower (see Fig. 4.6b).

Optimum parameters

In summary, larger detunings are necessary to reduce the heating during the readout process. However, with a larger detuning also the required power increases. This leads to a larger transfer from dark to the bright state, which is not suppressed by polarization. In addition, blue detunings transfer fewer atoms from the bright to the dark state and, therefore, it is preferred over red detunings. For these reasons, we conclude that in a standing wave, with a depth of 3.46 mK, it is a good trade-off to use a detuning $\Delta/2\pi = 123$ MHz, i.e. detuned $2\pi \times 44$ MHz from the AC- stark shifted atom at the bottom of the trap, and an intensity of 1.9 I_{sat} for an illumination time of 10 ms.

For systems with lower trap frequencies, and therefore less influence of the dipole force fluctuation, it is possible to go closer to resonance and reduce the required power for the NRF.

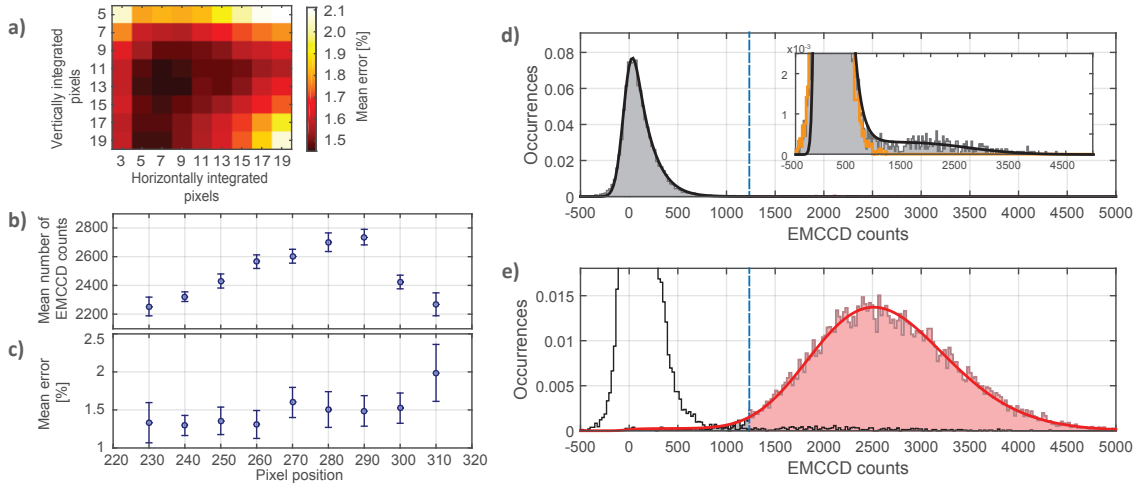

Figure 4.7. *State detection characterization.* **a)** Mean error using different number of pixels for the region of interest. **b)** Mean number of counts at different positions on the EMCCD. **c)** Mean error at different positions on the EMCCD. **d)** Histogram for the number of detected counts for atoms prepared in the state $F = 1$ (gray shaded area) and the fit model described in Sec. 4.2.2 (solid black line) threshold is indicated as the blue vertical line. The inset is a zoom into the low probability events and it includes the histogram for dark images (orange line). **e)** Same as in **d** but for atoms prepared in state $F = 2, m_F = -2$ (red shaded area) and a fit to the histogram (solid red line). The histogram for the state $F = 1$ is included (black line) for a direct comparison.

4.1.4 State detection fidelity for resolved atoms using the threshold method

The idea behind characterizing the state detection fidelity is to prepare atoms in a well-defined initial state and then perform a state detection measurement to later characterize the fidelity of the readout process by comparing the prepared and detected states. The result of such characterization is a combination of state readout and state preparation fidelities and, therefore, the accuracy is limited by the state preparation.

The experimental procedure is the same as described in Sec. 4.1.2 but in this case only for the optimum parameters listed above. For a precise quantification of the fidelity, the mean number of detected photons for the dark ($F = 1$) and bright states ($F = 2, m_F = -2$) is not enough, but it is necessary to record the distribution of the detected counts.

When an atom is illuminated with the NRF, depending on the internal state, a certain number of photons is detected by the camera. In order to count these photons, a region of interest must be defined. The histogram for the counts detected in a ROI of 7×13 pixels using $1.5{\times}10^4$ individual atoms is shown in Fig. 4.7d and e. The count histograms (normalized to its area) can be interpreted as the probability distribution that describes the number of detected counts from an atom in the ground states $F = 1$ and $F = 2$ and will be labeled as $P(c|F = 1)$, and $P(c|F = 2)$ respectively.

In order to infer the internal state from the detected photons, a threshold T is chosen such that for a total number of counts below T the atom is considered to be in the dark state ($F = 1$), and otherwise in the bright state ($F = 2$). Given the above histograms, the state detection error for a threshold T is given

by [43, 44, 119]

$$Err(T, |F = 1) = \int_{T}^{\infty} P(c|F = 1)\,\mathrm{d}c, \tag{4.3a}$$

$$Err(T, |F = 2) = \int_{0}^{T} P(c|F = 2)\,\mathrm{d}c. \tag{4.3b}$$

The optimum threshold T_{opt} is defined as the threshold that minimizes the mean value of both errors, i.e. $\mathrm{ME}(T_{\mathrm{opt}}) = \min\{\mathrm{ME}(T) \mid T \in [0, \infty)\}$, where $\mathrm{ME}(T)$ is the mean value for both errors in Eqs. (4.3). From now on, we will refer to $\mathrm{ME}(T_{\mathrm{opt}})$ as the *mean error*.

The mean error depends on the number of pixels chosen for the ROI. The larger the size of the ROI, the more pixels used to integrate the detected counts, but at the same time the number of clock-induced charges increases. In Fig. 4.7a the mean error dependence on the chosen number of pixels is shown. The plot indicates that the best compromise is to choose a ROI = 7×13 pixels (which collects about 87%) of the incident photons. Using the best parameters for the NRF described in Sec. 4.1.3, we obtain the figures of merit:

Internal state	Survival probability	Mean number of counts	Detection error
True dark image	99.4 ± 0.1%	69 ± 1	-
$F = 1$	99.4 ± 0.1%	113 ± 3	2.10 ± 0.45%
$F = 2$	99.0 ± 0.2%	2 484 ± 6	0.7 ± 0.4%

The survival probability for the true dark image[5] turns out to be the same as for $F = 1$. This is not surprising since atoms in the dark state are not expected to interact with the NRF.

These settings lead to a mean error of 1.43 ± 0.21%. Furthermore after the readout process, ∼ 98% of the atoms remain in its initial state[6]. Therefore, this method is non-destructive not only in the sense that the atom is not lost, but also that the internal state is preserved.

In the histogram for the dark state in Fig. 4.7d, a few events are observed with a large number of EMCCD counts. These high counts can be caused either by bad state preparation or by re-pumping to the bright state. Even though the NRF is detuned by $2\pi \times 6.8$GHz, for the settings used here, we expect, from Eq. (4.2), that after 10 ms of interaction about 2% of the atoms are transferred to the bright state. By comparing the true dark histogram, i.e. the one measured in between the reference pictures where no light is present, and the dark state readout histogram, we estimate that about 2.1% of the atoms appear to be bright, which agrees with our expectation.

To ensure that the readout fidelity does not depend on the atom's position in the dipole trap, we select atoms only in the interval $[x_i - 5, x_i + 5]$ being x_i the position on the EMCCD in pixels. In Fig. 4.7b the mean number of detected counts for each position is plotted. There, due to the AC-Stark shift, the number of detected counts varies about 30%, but nonetheless, in the same region the mean error remains relatively constant (see Fig. 4.7c).

[5] The true dark image corresponds to SD3 in Sec. 4.1.2, i.e. two reference images are taken and a true dark image is taken in between. It is used to characterize the survival probability of the imaging process and losses due to technical fluctuations.

[6] These same settings for the frequency detuning were used in the data shown in Fig. 4.6 (blue circles) were the transfer to the dark state after the readout process was characterized.

Increasing experimental repetition rates

One of the most time consuming parts in a typical experimental sequence is the loading of atoms in the MOT, on the order of one second, which is large compared to the time scales for state manipulation and readout that take a few tens of milliseconds. To understand how the non-destructive state detection can speed up a given measurement, let us assume that N_0 atoms are loaded initially. After n_r repetitions, the number of "effective" atoms that have contributed to the measurement is then given by

$$N_\mathrm{eff} = N_0 \frac{1 - p^{n_\mathrm{r}}}{1 - p},$$

where p is the survival probability. In order to find the optimum number of repetitions, one must consider the MOT loading time t_load and the time t_rep each repetition takes in order to calculate the total number of repetitions per unit of time for a single loading

$$\mathsf{R} = N_\mathrm{eff}/(t_\mathrm{load} + n_\mathrm{r} t_\mathrm{rep}).$$

The number of repetitions that maximize R needs to be found numerically since there is no analytic solution for this equation. For a typical loading time $t_\mathrm{load} = 1$ s, $t_\mathrm{rep} = 0.1$ s and $p = 0.99$, the optimum number of repetitions is $n_r = 465$, which means that each atom is used on average 99 times. This is used in Chap. 5 for the recording of the Rabi oscillation dynamics of a single atom.

4.2 State determination of multiple atoms using Bayesian methods

The threshold method for state estimation presented in Sec 4.1.4 provides a simple and accurate way to infer the internal atomic state of a single atom. However, this method fails when multiple atoms are present in the same region of interest. The collected fluorescence cannot be clearly attributed to different ROIs if two atoms are not optically resolved.

A similar problem arises on the identification of neutral atoms in optical lattices in the context of (non-state-dependent) molasses imaging, where it is necessary to differentiate between empty and occupied lattices sites. Standard approaches for the detection of arrays of bright atom are fitting by multiple PSFs [21, 26], or parametric deconvolution methods [22, 24, 25, 38]. However, the latter relies on the acquisition of a high signal to noise image of the trapped atoms, which is not the case for the state-dependent fluorescence, where the number of photons detected is very small. Related techniques have been employed for the identification of the internal states of ion chains using images obtained by state dependent fluorescence, e.g. in Ref. [120]. There an iterative maximum likelihood method was used in order to determine the maximum state of up to four ions.

In this section, a novel image analysis method is presented. This method uses the information available about the experimental system in order to differentiate between atoms in the bright and dark state using Bayesian methods. In Sec. 4.2.1 some basic principles regarding Bayes' theorem are reviewed and its direct application to the state determination problem is presented. In Sec. 4.2.2 the statistics of photon scattering by a neutral atom in the bright and dark state is discussed and, together with a model for the EMCCD camera response, are used to reproduce the measured count histograms shown in Fig. 4.7. In Secs. 4.2.3 - 4.2.5 the method is applied to experimental data of a few atoms and its accuracy is studied

by numerical simulations. Finally in Sec. 4.2.6 an algorithm that extends the method for 2D optical lattices is presented.

4.2.1 Bayes' Theorem

In Sec. 4.1.4, the state detection fidelity was characterized by preparing atoms in a well-defined state S and then illuminating them with a near-resonant field. By doing this, we have experimentally measured the probability $P(c|\mathrm{S})$ that for an atom in a state S we detect a total number of counts c in the ROI around the atom as shown by the histogram in Fig. 4.7. However, for the determination of the internal state of an atom, one usually asks the opposite question: if a number of counts c is detected, then what is the probability $P(\mathrm{S}|c)$ that the atom is in state S? [121]. The answer to this question is given by Bayes' theorem which relates these two quantities [122]

$$P(\mathrm{S}|c) = \frac{P(c|\mathrm{S})P(\mathrm{S})}{P(c|\mathrm{B})P(\mathrm{B}) + P(c|\mathrm{D})P(\mathrm{D})}. \tag{4.4}$$

The probability $P(\mathrm{S})$, for $\mathrm{S}\in\{\mathrm{B},\mathrm{D}\}$, represents the prior probability that the atom is in state S.

So far, we have experimentally measured $P(c|\mathrm{S})$ by adding up all the detected counts in a ROI but intuitively one notices that this is not the most efficient usage of the information since each pixel provides different amount of knowledge. Pixels that are far from the center position of the atom's image on the detector provide less information than pixels close to the center. This fact can be included in Bayes' theorem by rewriting Eq. (4.4) for each individual pixel i as

$$P_i^{\mathrm{pos}}(\mathrm{S}) = P_i(\mathrm{S}|c) = \frac{P_i(c|\mathrm{S})P_i^{\mathrm{pri}}(\mathrm{S})}{P_i(c|\mathrm{B})P_i^{\mathrm{pri}}(\mathrm{B}) + P_i(c|\mathrm{D})P_i^{\mathrm{pri}}(\mathrm{D})} = \frac{P_i(c|\mathrm{S})P_i^{\mathrm{pri}}(\mathrm{S})}{\sum_{\mathrm{S}} P_i(c|\mathrm{S})P_i^{\mathrm{pri}}(\mathrm{S})}, \tag{4.5}$$

where $P_i(c|\mathrm{S})$ is the count distribution for that pixel, $P_i^{\mathrm{pri}}(S)$ is the probability that the atom is in state S before using the of information in pixel i, and $P_i^{\mathrm{pos}}(S)$ is the probability that the atom is in state S after using the information in pixel i. By utilizing Bayes' theorem in Eq. (4.5), each pixel provides a different amount of information. For pixels far from the center of the atom's image, the distribution of counts for the bright and dark states look very similar, i.e. $P_i(c|\mathrm{D}) \approx P_i(c|\mathrm{B})$, and therefore not much information has been gained, i.e. $P_i^{\mathrm{pos}}(\mathrm{S}) \approx P_i^{\mathrm{pri}}(\mathrm{S})$. In contrast, for pixels close to the center of the atom's image, the count distributions are significantly different providing more information. Furthermore, the information about the state after considering pixel i can be used as the prior knowledge for including the information of pixel $i+1$, i.e. $P_{i+1}^{\mathrm{pri}}(\mathrm{S}) = P_i^{\mathrm{post}}(\mathrm{S})$. Since for the first pixel there is no prior information, we assume that $P_1^{\mathrm{pri}}(S) = 0.5$.

Bayes' formula (4.5), provides a method to use the information contained pixel by pixel taking into account their distance to the atom's position. Nevertheless, to use Bayes' theorem, it is necessary to know the count distribution for every individual pixel $P_i(c|\mathrm{S})$. Unlike the total count distribution $P(c|\mathrm{S})$, the distribution for each pixel cannot be experimentally measured since the atom's position can drift with respect to the camera, which means that the average number of counts hitting the pixel is not constant. Even if the position of the atoms remains constant, in order to obtain reasonable smooth histograms, the required measurement time would be extremely long. Therefore, it is necessary to obtain a general theoretical model to efficiently generate the correct counting distribution for all pixels $P_i(c|\mathrm{S})$. We construct such a model by considering the detector properties of the EMCCD camera and determine the

model parameters by fitting the experimental measured histograms for the counting distribution of a ROI window in Fig. 4.7.

4.2.2 Modeling the EMCCD count histograms

The count distribution as recorded by a EMCCD camera are shaped by two main effects:

- **Photon scattering statistics considering transfer between the states**. Atoms in the bright state scatter typically a large number of photons. However, if they are transferred to the dark state they stop fluorescing. The opposite happens to an atom in the dark state, it remains dark unless it is transferred to the bright state, where it can scatter a large number of photons. The possibility of transitions between the two states during illumination must be considered when describing the statistics of photon scattering events.
- **Camera response**. It is necessary to understand how the EMCCD camera converts photon detection events into digital counts. This process in particular includes the electron multiplication (EM) gain, sources of electronic noise such as Clock-Induced-Charges (CIC) and the digitization stage.

Photon statistics from atoms in the bright and the dark state

As a first step, let us describe the statistics of photons emitted by the atom under interrogation.

Photons detected from an atom in the bright state

For a system driven on an ideal closed cycling transition, the number of photons emitted during the illumination time is Poisson distributed. However, for a real atom, excitations by the illumination light into states outside the two-level system can transfer the atom to a dark state thereby modifying the photon emission distribution. This effect is described in Ref. [119], which provides an analytic expression for the probability to detect n photons during the illumination process

$$P_{\mathrm{B}}\left(n, \alpha_{\mathrm{B}}, n_0\right) = \frac{n_0^n \exp\left[-\left(\alpha_{\mathrm{B}}+1\right) n_0\right]}{n!} + \frac{\alpha_{\mathrm{B}}}{\left(1+\alpha_{\mathrm{B}}\right)^{n+1}} \gamma_{\mathrm{inc}}\left(n+1, \left(1+\alpha_{\mathrm{B}}\right) n_0\right), \tag{4.6}$$

where $\gamma_{\mathrm{inc}}(a, x) = \frac{1}{(a-1)} \int_0^x y^{a-1} e^{-y} \mathrm{d}y$ is the lower incomplete gamma function, α_{B} is the leakage probability per detected photon, and n_0 is the number of photons that would be detected on average without leakage into the dark state.

Photons detected from an atom in the dark state

When an atom is in the dark state and the near-resonant beam is turned on, few photons are scattered at a rate that is much lower than for the bright state. However, one of these scattering processes can transfer the atom to the bright state where it scatters a significant amount of photons. The number of photons that an atom scatters when it is initially prepared in the dark state is be described by [119]

$$P_{\mathrm{D}}\left(n, \alpha_{\mathrm{D}}\right) = \exp[-\alpha_{\mathrm{D}} n_0]\left[\delta_{n,0} + \frac{\alpha_{\mathrm{D}}}{\left(1-\alpha_{\mathrm{D}}\right)^{n+1}}\right] \gamma_{\mathrm{inc}}\left(n+1, \left(1-\alpha_{\mathrm{D}}\right) n_0\right), \tag{4.7}$$

where α_D represents the leakage rate per detected photon. The first term in the square brackets is a Kronequer delta and accounts for the atoms that are never transferred to the dark state and the second term accounts for atoms leaked to the bright state.

Camera response

Part of the photons emitted by the atom reach the CCD detector, where they generate electric charges that are later amplified by electronic multiplication. To model the number of counts after the amplification process, we start by analyzing the amplification of charges contained in a single pixel, and later generalize it to charges distributed over many pixels.

Detecting n electrons in a single pixel

Charges on a pixel of the CCD can either be generated by photon detection events or CIC. After the multiplication process in the EM gain register the probability to detected c counts as a result of n initial charges is given by the Erlangen distribution [80]

$$P_{\mathrm{EM}}(c, n, \gamma) = \frac{1}{\gamma^n \Gamma(n)} c^{n-1} \exp\left(-c/\gamma^n\right), \tag{4.8}$$

where γ is the mean number of counts after amplification per charge generated in the sensor (cf. the definition used in Sec. 2.4.3). After the electronic multiplication process, noise is added in the readout process (cf. Sec. 2.4.3), which is Gaussian distributed

$$P_{\mathrm{read}}(c, \sigma, \mu) = \frac{1}{\sqrt{2\pi}\sigma} \exp\left[-\frac{(c-\mu)}{2\sigma^2}\right]. \tag{4.9}$$

Therefore, the total number of EMCCD counts c after amplification and readout for a single pixel containing n electrons is given by the convolution of the probabilities in Eqs. (4.8) and (4.9)

$$P_1(c, n, \gamma, \sigma, \mu) = P_{\mathrm{EM}}(c, n, \gamma) * P_{\mathrm{read}}(c, \sigma, \mu). \tag{4.10}$$

Detecting N electrons in m pixels.

If a set of m pixels contains a total number of charges $N = \sum n_i$, where n_i is the number of charges contained in pixel i, then the probability distribution describing the total number of EMCCD counts c

after the readout is[7]

$$P_m(c, N, \gamma, \sigma, \mu) \equiv * \prod_{i=1}^{m} P_1(c, n_i, \gamma, \sigma, \mu) \tag{4.11}$$

$$= * \prod_{i=1}^{m} P_{\mathrm{EM}}(c, n_i, \gamma) * P_{\mathrm{read}}(c, \sigma, \mu) \tag{4.12}$$

$$= \left[* \prod_{i=1}^{m} P_{\mathrm{EM}}(c, n_i, \gamma) \right] * \left[* \prod_{i=1}^{m} P_{\mathrm{read}}(c, \sigma, \mu) \right] \tag{4.13}$$

$$= \left[* \prod_{i=1}^{m} P_{\mathrm{EM}}(c, n_i, \gamma) \right] * P_{\mathrm{read}}\left(c, \sqrt{m}\sigma, \mu\right), \tag{4.14}$$

where the definitions in Eqs. (4.9) and (4.10) have been used. The first term in the square brackets is the distribution describing the total number of counts after the EM amplification (before readout), which can be simplified to $* \prod_{i=1}^{m} P_{\mathrm{EM}}(c, n_i, \gamma) = * \prod_{i=1}^{N} P_{\mathrm{EM}}(c, 1, \gamma) = P_{\mathrm{EM}}(c, N, \gamma)$.

Finally, the count distribution after readout for N charges generated in m pixels is

$$P_m(c, N, \gamma, \sigma, \mu) = P_{\mathrm{EM}}(c, N, \gamma) * P_{\mathrm{read}}\left(c, \sqrt{m}\sigma, \mu\right). \tag{4.15}$$

CIC generated in the CCD sensor

In addition to electrons generated by photons hitting the CCD, CIC contaminate the image by generating extra electrons. The probability p_0 to generate a CIC is constant throughout the CCD, and hence the number of counts is Poissonian distributed for each pixel. Therefore, the probability that n charges are generated in a set of m pixels is also Poissonian distributed

$$P_{\mathrm{CIC}}(n, m) = \frac{(m p_0)^n \exp(m p_0)}{n!}. \tag{4.16}$$

Combined effect of camera readout and photon emission statistics

Total number of electrons generated in the sensor (photons + CIC)

The total number of charges generated in the CCD is the combined contribution of the CIC and electrons generated by photon detection. Therefore, the total number of counts after the readout process is described by the convolution of the probabilities in Eqs. (4.6), (4.7), and (4.16)

$$P_{\mathrm{tot,S}}(n, m, \alpha_{\mathrm{S}}, n_0) = P_{\mathrm{S}}(n, \alpha_{\mathrm{S}}, n_0) * P_{\mathrm{CIC}}(n, m) \tag{4.17}$$

$$= \sum_{k=0}^{n} P_{\mathrm{S}}(n-k, \alpha_{\mathrm{S}}) \frac{(m \cdot p_0)^k \exp(m \cdot p_0)}{k!}$$

for S = B, D.

[7] $* \prod_{i=1}^{m} P_1$ represents m times the convolution of P_1, i.e. $* \prod_{i=1}^{m} P_1 = \underbrace{P_1 * P_1 * ... P_1}_{\text{m times}}$.

Distribution of counts for bright and dark atoms

Now, we have all the elements needed to model the statistics of counts generated by the camera during the illumination of an atom by a near-resonant field. On the one hand, Eq. (4.15) describes the camera response when N charges distributed in m pixels; on the other hand, the probability to generate N charges on the sensor is described by Eq. (4.17). Finally, the distributions of EMCCD counts for an atom illuminated in the bright or dark state are given by the sum of the camera response weighted by the probability to generate N electrons

$$D_{\mathrm{B}}(c, n_0\,; \gamma, \sigma, m, \alpha_{\mathrm{B}}) = \sum_{N=0}^{\infty} P_{\mathrm{tot,B}}\,(N, m, \alpha_{\mathrm{B}}, n_0)\, P_m\,(c, N, \gamma, \sigma, \mu) \tag{4.18a}$$

$$D_{\mathrm{D}}(c, n_0\,; \gamma, \sigma, m, \alpha_{\mathrm{D}}) = \sum_{N=0}^{\infty} P_{\mathrm{tot,D}}\,(N, m, \alpha_{\mathrm{D}}, n_0)\, P_m\,(c, N, \gamma, \sigma, \mu)\,. \tag{4.18b}$$

Fig. 4.7 shows the result for a fit of Eqs. (4.18) to the count histograms for the bright and dark states. From the fit we obtain the mean number of detected photons $n_0 = 31.1$ and the leakage rates $\alpha_{\mathrm{B}} = 0.0010$, $\alpha_{\mathrm{D}} = 0.0011$. For simplicity, from now on we will just write $D_{\mathrm{D}}(c, n_0)$ and $D_{\mathrm{B}}(c, n_0)$ since the values of all other variables remain constant.

4.2.3 Single atoms: illustrative example

To illustrate how the model for the count distributions is used in Bayes' theorem for the state detection, we analyze just ROIs containing well-resolved single atoms. So far, Eqs. (4.18) provide a way to determine the distribution of counts after the read out of a ROI with m pixels. However, to use these equations, we need to estimate the mean number of photons that each pixel detects, i.e. we need to provide the information about the spatial distribution of photons on the CCD. To simplify the problem, we will not use the full 2D images but we integrate all images along the vertical direction and work only with the integrated profiles, as shown in Fig. 4.8. By doing so, the spatial distribution of photons for the integrated pixels is provided by the Line Spread Function (LSF), which was determined in Sec. 2.4.5. Using the LSF, we are now able to compute the distributions of counts for each individual pixel, and therefore we can use Bayes' theorem.

Including spatial information of the LSF

We start by selecting a region of interest with m_{H} in the horizontal direction and m_{V} pixel in the vertical direction containing a single atom. Integration along the vertical direction leaves us with m_{H} "integrated-pixels".

Now, we determine the mean number of photons n_i that each individual integrated-pixel detects using the information in the LSF. If an atom is located at position x_0 in the integrated region of interest, then we select the interval $I = [x_0' - p_{\mathrm{H}}, x_0' + p_{\mathrm{H}}]$, where $x_0' = \mathrm{round}(x_0)$ and p_{H} is the number of pixels to the side. We denote the mean number of photons detected in the interval I by N_0. The mean number of photons n_i contained in the integrated-pixel p_i is

$$n_i = \int_{p_i-0.5}^{p_i+0.5} N_0 \times \mathrm{LSF}\,(x_0 - p)\, dp \approx N_0 \times \mathrm{LSF}\,(x_0 - p_i) \tag{4.19}$$

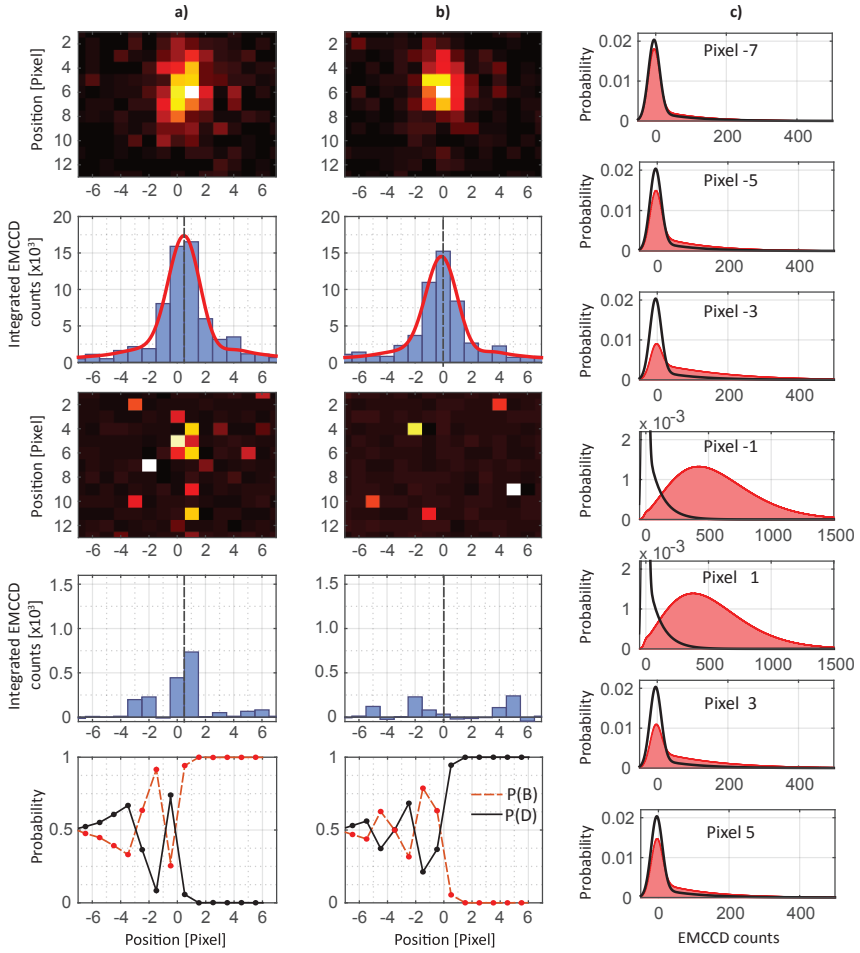

Figure 4.8. *Bayes update with single atoms.* **a)** From top to bottom: single atom reference image; reference image integrated along the vertical direction; state detection image of an atom in the bright state; state detection image integrated along the vertical direction; Bayesian update result, the dots represent the probability after using the previous pixel and prior the use of the next pixel ($P^{\text{pri}}_{i+1} = P^{\text{pos}}_{i}$). **b)** same as in **a** but for an atom in the dark state. **c)** Calculated count distributions of different pixels for the atom shown in **a**.

where LSF is the line spread function normalized to its area in the interval I.

Once n_i is known, we use Eq. (4.18) to calculate the distributions for the bright and dark states, $D_{\text{B}}(c, n_i)$, $D_{\text{D}}(c, n_i)$. These two distributions represent the probabilities needed for the Bayes' update rule described in Eq. (4.5), where $P_i(\text{B}|c) = D_{\text{B}}(c, n_i)$ and $P_i(\text{D}|c) = D_{\text{D}}(c, n_i)$.

If the mean number of photons contained in the interval I is constant, then the distribution of counts for each pixel, $D_{\text{B,D}}(c, n_i)$, only depends on the distance to the center position of the atom's image on the CCD. The numerical calculation for the count histograms can be slow, therefore it is convenient to pre-compute a set of count distributions for different atom-pixel distances. Fig. 4.8c shows examples of the calculated distributions for a few integrated-pixels. It is important to note that the position of the atom does not always correspond to the center of a pixel (see Fig. 4.8). For this reason, it is necessary to

pre-compute a large set of count histograms for different non-integer atom-pixel distances.

Experimental implementation

Fig. 4.8 illustrates the Bayesian update algorithm procedure starting at the integrated-pixel -7. At this point, there is no prior information, thus we set $P^{\text{pri}}_{-7}(\text{B}) = P^{\text{pri}}_{-7}(\text{D}) = 0.5$. The number of counts detected in the integrated-pixel -7 is used to calculate the probability $P^{\text{post}}_{-7}(\text{S})$. The result is then used as the prior probability for the next pixel, i.e. $P^{\text{pri}}_{-6}(\text{S}) = P^{\text{post}}_{-7}(\text{S})$. This procedure is repeated up to pixel 7.

If the final probability of an atom to be in the bright state is above 0.5, then we assume that the atom is in the bright state, else it is considered to be in the dark state. By applying this procedure to the recorded set of experimental data, we obtain a detection error of $2.20 \pm 0.35\%$ for the dark state and $0.63 \pm 0.18\%$ for the bright state, which leads to a mean error of $1.4 \pm 0.2\%$. This error is the same value as the one obtained by the threshold method in Sec. 4.1.4.

Although the mean error for the state detection of a single atom using the threshold method and the Bayesian update algorithm is the same, the latter has the advantage that it provides a certainty on the state determination since the result is a probability. The usefulness of the Bayesian method becomes clear when estimating the state of many atoms that are close together, where the threshold method fails.

4.2.4 Atom pairs

When two atoms are present in the same ROI, there are four possible outcomes for the readout of the internal state, BB, BD, DB and DD, which represent all possible combinations of bright (B) and dark (D) states. The application of Bayes' formula in Eq. (4.5) is straightforward by using $\text{S} \in \{\text{BB, BD, DB, DD}\}$ once the four counting distributions $P_i(c|\text{BB})$, $P_i(c|\text{BD})$, $P_i(c|\text{DB})$, $P_i(c|\text{DD})$ have been determined.

Including spatial information of the LSF

The procedures is the same as described in Sec. 4.2.3, but here the origin of the image is defined by $x_0 = \min\{x_1, x_2\}$ where x_i is the positions of each atom. Then we select the interval $I_2 = [x'_0 - p_{\text{H}}, x'_0 + p_{\text{H}} + d']$, where x'_0 =round(x_0), p_{H} is the number of pixels to the side, d' =round(d), and d is the distance between the atoms (in a multiple of $\lambda_{\text{DT}}/2$).

To calculate the count distributions, first we consider the mean number photons detected from each atom in the integrated-pixel p_i using

$$n_{1,i} \approx N_0 \times \text{LSF}\,(x_0 - p_i)\,, \tag{4.20a}$$

$$n_{2,i} \approx N_0 \times \text{LSF}\,(x_0 - p_i + d)\,, \tag{4.20b}$$

where LSF is normalized to its area in the interval I_2 and N_0 is the mean number of photons expected from a single atom in the interval I_2.

The number of photons detected from the two atoms is the sum of the photons coming from each atom. Therefore, the total distribution of detected photons is obtained by convoluting the distributions for each atom (see Eqs. (4.6), (4.7)).

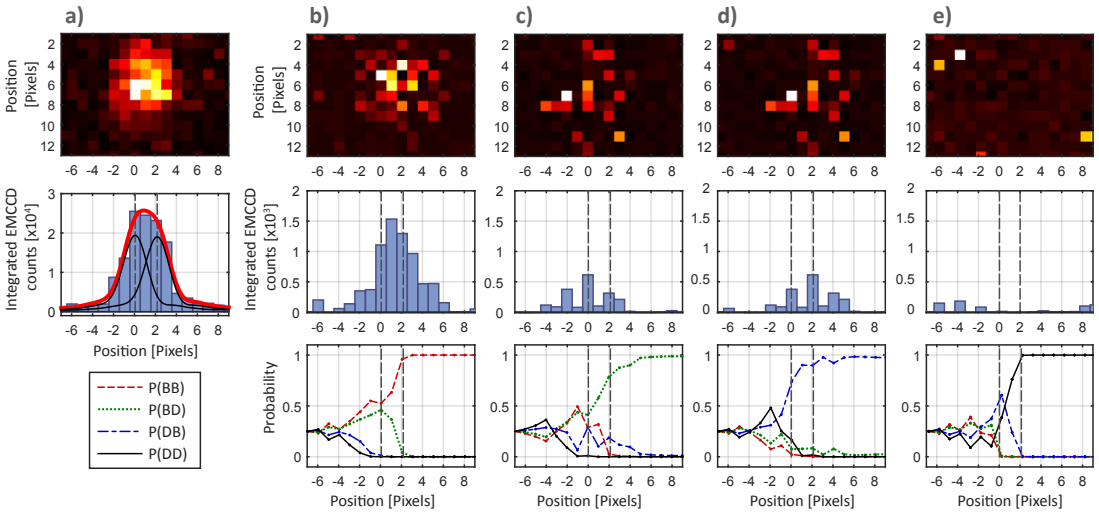

Figure 4.9. *Bayes update with two atoms.* **a)** Top: Reference image of two atoms separated by 2 lattice sites. Middle: Reference image integrated along the vertical and fitted using two LSF. **b**) Top: State detection image of two atoms in the BB state. Middle: State detection image integrated along the vertical direction. The dashed vertical lines represent the position of each atom. Bottom: Bayesian update result. The probability at each pixel represents the prior probability. **c-e)** Same as **b** but for the states BD DB and DD respectively.

$$P_{S_1,S_2}(n_{1,i}, n_{2,i}, \alpha_{S_1}, \alpha_{S_2}, n_0) = P_{S_1}(n_{1,i}, \alpha_{S_1}, n_0) * P_{S_2}(n_{2,i}, \alpha_{S_2}, n_0) \tag{4.21}$$

for S_1,$S_2 \in$ {B,D}.

Finally, the four count distributions are obtained by replacing P_S in Eqs. (4.17) and (4.18) by the two-atom distributions defined Eq. (4.21).

In the case for two atoms in the same ROI, the distributions of counts for each pixel depends not only on the distance from the pixel to the atom's position but also on the distance between the atoms. Therefore, a large set of distributions that contains many different combinations of pixel-atom distance and atom separations must be pre-computed.

Experimental implementation

In our experimental setup, we can prepare atom pairs in either the state BB or DD but we cannot address neighboring atoms individually to create the states BD and DB in a deterministic fashion. Nevertheless, we can use the fact that the "signal" from an atom in the dark state during the illumination is very similar to the one of an empty lattice site. We characterize the detection method for the cases of BD and DB, by simply simulating the dark state with an empty lattice site[8].

[8] In Sec. 4.1.4 it has been shown that about 2% of the atoms in the dark state appear to be bright due to the transfer $F = 1 \rightarrow F = 2$ induced by the near-resonant illumination, therefore, replacing the dark state with an empty lattice creates an error of the same order.

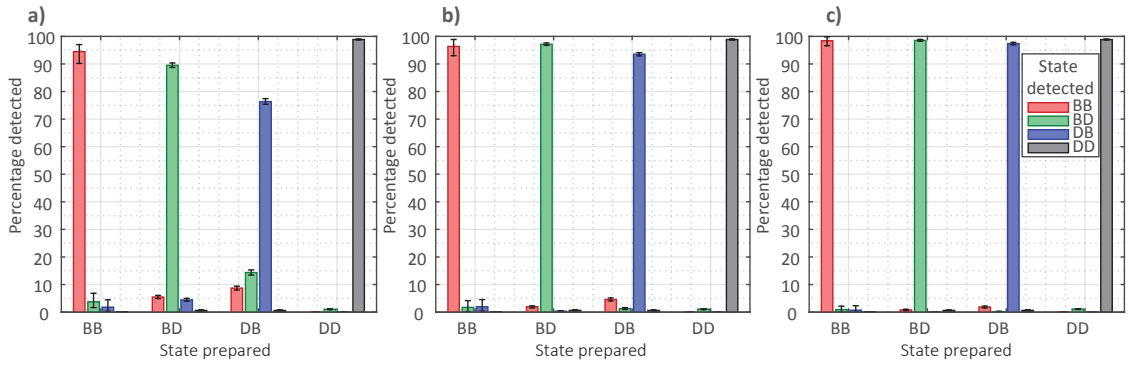

Figure 4.10. *Bayes update result for atom pairs.* Detection probability for every possible outcome for atom pairs prepared in different states, $P(S'|S)$. **a-c)** corresponds to separations of 1, 2 and 3 lattice sites respectively. The error bars are obtained by bootstrap resampling.

The Bayesian update algorithm works in the same way as described in Sec. 4.2.3, the only difference is that now we have four states and their respective distributions for each pixel. Fig. 4.9 shows the application of the algorithm to the four states for a pair of atoms separated by two lattices sites.

To characterize the state detection fidelity, we are interested on determining the probability that an atom pair prepared in a state S is detected in a state S′, which will be denoted as $P(S'|S)$ for the states S,S' ∈ {BB, BD, DB, DD}. The probability $P(S'|S)$ for the state determination using experimental data is plotted in Fig. 4.10 for atoms separated by 1, 2 and 3 lattices sites.

Even though atoms separated by one lattice represent the most challenging case, the determination of DD and BB states is quite accurate (> 95%). However, it is more complicated when just one atom is bright, i.e. for the state BD and DB. In this case, on average, only 85% of the cases are determined properly. Moreover, one can observe that the state BD is determined with higher accuracy than the state DB. This arises from the fact that the LSF has a small asymmetry that creates more light contamination to one side than to the other. For two and three lattices separation, the accuracy of the algorithm is always high (> 95%), which is remarkable taking into account that for these separations the atoms are not optically resolved.

We define as a figure of merit the *detection error* for the state S

$$Err(S) = 1 - P(S|S). \tag{4.22}$$

The mean error is then given by the average value of $Err(S)$ for the four states. This is plotted in Fig. 4.11 for atom separations up to 6 lattice sites. As expected, the detection error decreases as the distance between the atoms increases and it approaches the value for the single atom case (see Sec.4.2.3).

Bayesian update using the full 2D image

The Bayesian update algorithm has been applied, so far, using the vertically integrated image. If one intends to use the algorithm over the full 2D image, then an "effective" PSF that describes the 2D distribution of counts on the sensor is required. As a rough approximation for the effective PSF, we use an average image of many individual atoms. The image was calculated as described in 2.4.5 but instead of using the integrated profiles, each rows of pixels is used.

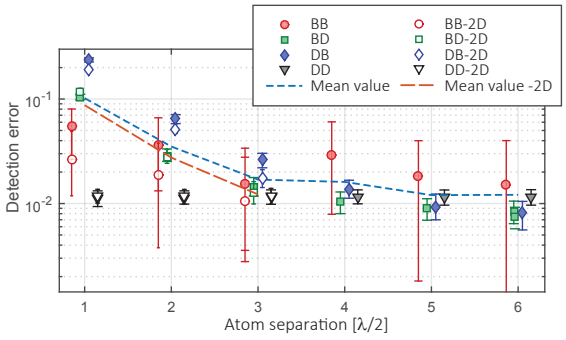

Figure 4.11. *Bayes update results for atom pairs.* Detection error $Err(S)$ for two atoms separated from one to six lattice sites. The filled (unfilled) markers are obtained using the 1D(2D)-Bayesian update. The error bars are obtained by bootstrap resampling.

The Bayesian update in 2D is performed in the same way as in the 1D case, but now using every single pixel in the chosen region of interest containing a total of 13×15 pixels. The results of the 2D analysis for atoms separated by 1, 2 and 3 lattice sites are shown in Fig. 4.11. We see that, as expected, the average detection error decreases. However, the gain is almost negligible compared to the computational cost, which has increased by a factor of 13.

4.2.5 Multiple atoms

The Bayesian update algorithm used to determine the state of two atoms can be extended for multiple atoms by calculating all possible combinations of bright and dark atoms. For a sparsely filled lattice, it is possible to divide the image into smaller ROI containing a few atoms, where the algorithm can be applied. However, this is not possible for images containing a large number of atoms. For many atoms the algorithm becomes computationally intractable due to its exponential scaling. In this section we present a procedure, which allows the determination of the internal state of an arbitrary number of atoms for a one-dimensional lattice. First the algorithm is introduced and later the fidelity is characterized with numerical simulation. Finally, the algorithm is compared with an alternative detection method based on the simultaneous fitting of many LSF to the fluorescence signal.

Bayes update for multiple atoms

When a large number of atoms N_{atoms} are present in the same region of interest, the direct application of Bayes' formula in Eq. (4.5) requires the calculation of $2^{N_{\text{atoms}}}$ combinations, which demands a large computation power. For example, in Fig. 4.12a, the schematic representation of a ROI with 13 lattice sites containing 7 atoms is shown. In this case, all 128 combinations of bright and dark states would have to be calculated. Fortunately, this problem can be significantly simplified. The pixels surrounding a particular atom are mainly influence by neighbor atoms and contain very little information about atoms that are far away. Therefore, when Bayes' formula (4.5) is applied to a set of pixels surrounding an atom, we can limit ourselves to including into the analysis only a few neighboring atoms. This reduces the number of combinations that must be calculated.

Before starting with the description of the algorithm some considerations and definitions are listed below:

- In our system, we study a region of interest in a 1D lattice. In the lattice, some sites can contain a bright or a dark atom, but they can also be empty. For simplicity, we assume that a dark atom is

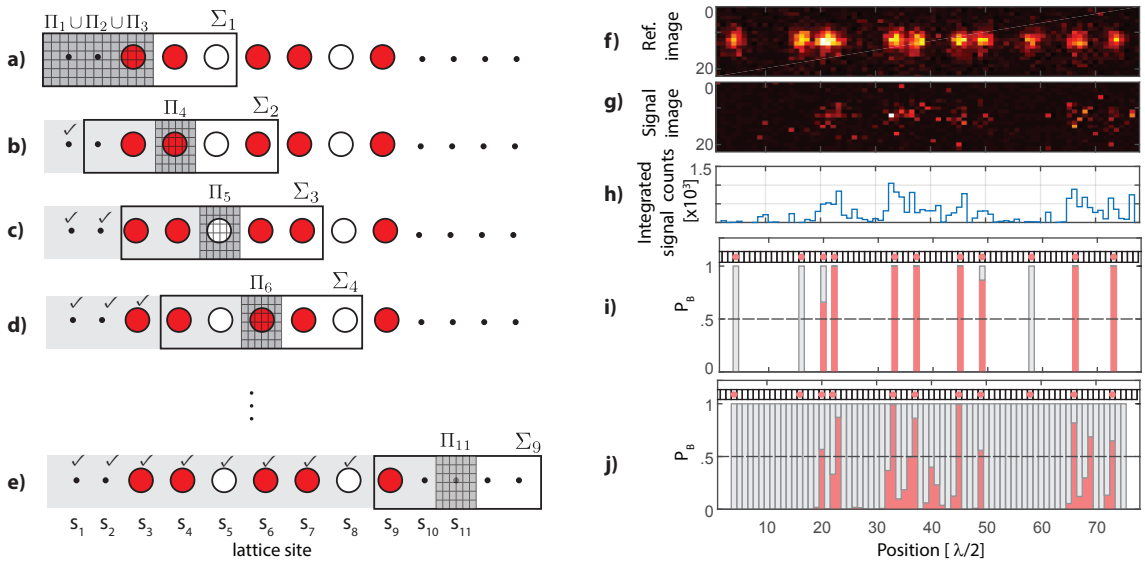

Figure 4.12. *Bayes update with multiple atoms.* **a-e)** Schematic representation of the Bayesian update algorithm for a one dimensional chain of neutral atoms. The dark gray regions represent the pixels used in every step. **f)** Reference image for the atoms trapped in the optical lattice. **g)** State detection image of atoms randomly prepared in the bright and dark state. **h)** Integrated counts of the signal image. **i)** Bayesian update result using the information of empty lattice sites. **j)** Bayesian update result without using the information on empty lattice sites.

indistinguishable from an empty lattice site and, therefore, the problem of detecting if an atom is bright or dark is the same as finding the probability that a lattice site s_i contains a bright atom. This probability will be denoted as $P_B(s_i)$. In the case that we have prior knowledge on which sites are empty, we include this information by setting $P_B^{\text{pri}}(s_i) = 0$, where i is the index for an empty site. Note that if the initial probability is zero then it remains zero after the application of Bayes' formula, Eq. (4.5).

- For a lattice site s_i located at position x_i, we define a corresponding set of surrounding integrated-pixels $\Pi_i = [-d/2, x_i + d/2]$, with d being the lattice separation (see Fig. 4.12a-e).

- The fluorescence of an atom in a lattice site s_i is not contained only in its corresponding set of pixels Π_i but the light contaminates pixels that correspond to other lattices sites. We assume that the fluorescence of the atom contaminates n_c lattice sites to each side. This implies that a set of pixels Π_i contains information of atoms in the sites $s_{i-nc}, ..., s_{i+nc}$.

- The set of pixels containing the atoms under study must include at least n_c empty lattice sites to the left of the first atom and to the right of the last atom. This is necessary to guarantee that all information available for the atoms contained in the pixels on the sides is included.

We demonstrate the algorithm using the example of a ROI containing 7 atoms and 13 lattice sites, as shown in Fig. 4.12. We assume that the fluorescence of each atom contaminates 2 neighboring sites to each side, i.e. $n_c = 2$. For this reason, the corresponding number of empty lattice sites has been artificially added to each side. The information on the empty sites is included by setting $P_B^{\text{pri}}(s_i) = 0$ for $i = 1, 2, 10, 11, 12, 13$. The procedure is then implemented as follows:

1. First we define the subset of lattice sites $\Sigma_1 = \{s_1, s_2, s_3, s_4, s_5\}$. We then calculate the probability for 2^5 possible combinations of bright and dark states of the form $S = S_1 S_2 S_3 S_4 S_5$ for $S_i \in \{\mathrm{B,D}\}$ and $i = 1, ...5$.

2. To apply Bayes update algorithm on Σ_1 we must use only the set of pixels $\Pi_1 \cup \Pi_2 \cup \Pi_3$. This is because the set Π_4 contains information about the atom in lattice site s_6 and it is not inside the set Σ_1 (see Fig. 4.12a). As a result of the application of Bayes' Theorem we obtain $P^{\mathrm{post}}_{\Sigma_1}(\mathrm{S})$, which contains information about the five lattice sites in Σ_1.

3. At this point we have used all the pixels that provide information to the site s_1. Therefore, we can remove it from the set under study and include s_6 instead. To remove the site s_1 we need to calculate the probability that it contains a bright atom, which is done by marginalization.

$$P_{\mathrm{B}}(s_1) = \sum_{\mathrm{S}_2 ... \mathrm{S}_5 \in \{\mathrm{B,D}\}} P^{\mathrm{pos}}_{\Sigma_1}(\mathrm{BS}_2\mathrm{S}_3\mathrm{S}_4\mathrm{S}_5)\,. \tag{4.23}$$

4. Including the site s_6 means that we redefine the set of lattice sites under study, which now is $\Sigma_2 = \{s_2, s_3, s_4, s_5, s_6\}$ (see Fig. 4.12b).

5. In order to apply Bayes update for the states in Σ_2, first we need to calculate a set of prior probabilities. To this end, we use the result of the calculated posterior probabilities $P^{\mathrm{post}}_{\Sigma_1}(\mathrm{S})$ together with the information for the site that was added, i.e. $P^{\mathrm{pri}}_{\mathrm{B}}(s_6)$. The new set of priors are then given by

$$\begin{aligned} P^{\mathrm{pri}}_{\Sigma_2}(\mathrm{S}_2...\mathrm{S}_5\mathrm{B}) &= P^{\mathrm{pos}}_{\Sigma_1}(\mathrm{BS}_2...\mathrm{S}_5)\, P^{\mathrm{pri}}_{\mathrm{B}}(s_6) \\ P^{\mathrm{pri}}_{\Sigma_2}(\mathrm{S}_2...\mathrm{S}_5\mathrm{D}) &= P^{\mathrm{pos}}_{\Sigma_1}(\mathrm{BS}_2...\mathrm{S}_5)\, P^{\mathrm{pri}}_{\mathrm{D}}(s_6) \end{aligned} \quad \text{if} \quad P_{\mathrm{B}}(s_1) > 0.5$$

$$\begin{aligned} P^{\mathrm{pri}}_{\Sigma_2}(\mathrm{S}_2...\mathrm{S}_5\mathrm{B}) &= P^{\mathrm{pos}}_{\Sigma_1}(\mathrm{DS}_2...\mathrm{S}_5)\, P^{\mathrm{pri}}_{\mathrm{B}}(s_6) \\ P^{\mathrm{pri}}_{\Sigma_2}(\mathrm{S}_2...\mathrm{S}_5\mathrm{D}) &= P^{\mathrm{pos}}_{\Sigma_1}(\mathrm{DS}_2...\mathrm{S}_5)\, P^{\mathrm{pri}}_{\mathrm{D}}(s_6) \end{aligned} \quad \text{if} \quad P_{\mathrm{B}}(s_1) < 0.5 \tag{4.24}$$

   Here the new priors $P^{\mathrm{pri}}_{\Sigma_2}$ needs to be renormalized. In this way, all the correlations between the state of the atoms in Σ_2 are maintained.

6. We apply Bayes update formalism to Σ_2 using only the set of pixels Π_4. By doing this, we obtain the posterior probabilities $P^{\mathrm{post}}_{\Sigma_2}(\mathrm{S})$. Starting from step 3, the same procedure is repeated until the last set of pixels that contains information on the last lattice site is reached. In this example, the last lattice site is s_9, therefore we use up to the set Π_{11} (see Fig. 4.12c-e)

By using this algorithm, all the pixels containing significant information about a given atom are used to estimate its internal state.

Characterization of the algorithm

The application of the Bayesian algorithm for multiple atoms to experimental data is shown in Fig. 4.12f-j. The chosen image corresponds to a set of atoms that has been prepared in state $F = 2, m_F = -2$ and then a $\pi/2$ microwave pulse has been applied leading to a random distribution of bright and dark atoms. The algorithm has been applied in two different ways. In the first, the information on empty lattice sites at

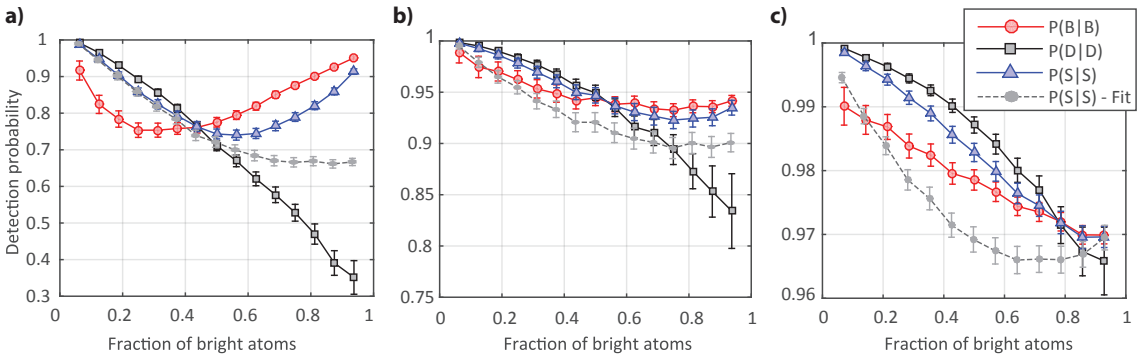

Figure 4.13. *Simulation for Bayes update with multiple atoms.* **a)** Numerical simulation for the internal state detection fidelity of neutral atoms in a 1D standing wave as a function of the filling factor of bright atoms. The red circles (black squares) represent the correct detection probability for the bright (dark) atoms. The blue triangles represent the correct detection probability for an arbitrary state. The light gray dashed lines are the results for the correct detection probability obtained by the fitting method. In the simulation, we assume a lattice spacing of 1.051 pixels and use the LSF of our experimental system, which has a FWHM of 3.15 pixels. **b)-c)** same as **a** but assuming lattice separations of 2.1 and 3.15 pixels respectively. All error bars represent 95% confidence interval estimated by bootstrap resampling.

positions j is included by $P_j(\mathrm{B}) = 0$ (see Fig. 4.12i). In the second case, no information about the empty lattice sites was provided (Fig. 4.12j). The latter case is equivalent to finding the location of an unknown number of atoms in the lattice using the signal image, which contains only a few photons. Even though this is a complex scenario, the algorithm still gives reasonable good results.

To characterize the performance of the algorithm, it is necessary to have a large number of atom combinations in bright and dark states in well-defined positions. Since we cannot deterministically prepare the atoms in different states, we have implemented a numerical simulation. The simulation creates a one-dimensional lattice, where 16 atoms are next to each other. The number of randomly positioned bright atoms in the lattice was varied from 1 to 15 and each case was repeated 1000 times. In this way we quantify the probability to detect the state properly as the ratio of bright atoms increases (see Fig. 4.13a).

In addition to the Bayesian algorithm, the results of a second detection method are presented. This method works by fitting multiple LSF to the state-dependent fluorescence signal and depending on the amplitude of the fit the state is determined to be either bright or dark. For the fitting procedure only $P(\mathrm{S}|\mathrm{S})$ is shown as a gray dashed line Fig. 4.13a. From the results of both simulations, we concluded that by using the Bayesian algorithm, at least, 75% of the atoms are detected in the correct state. This is superior to the fitting method where the number of detected atoms is only 68% for densely filled lattices.

In Fig. 4.13b,c two more simulations are presented. The simulations assume optical systems that have two and three times better optical resolution, which were chosen because experimental setups with these characteristics already exist [21, 22]. For these optical resolutions, the fidelity of the Bayesian method increases and gives always better results compared to the fitting procedure. The Bayesian method is not only better in terms of accuracy but also in the computational time required. While the fitting procedure requires 90 ms to fit the fluorescence signal of 7 atoms, the Bayesian algorithm requires only 2 ms and scales linearly with the number of atoms.

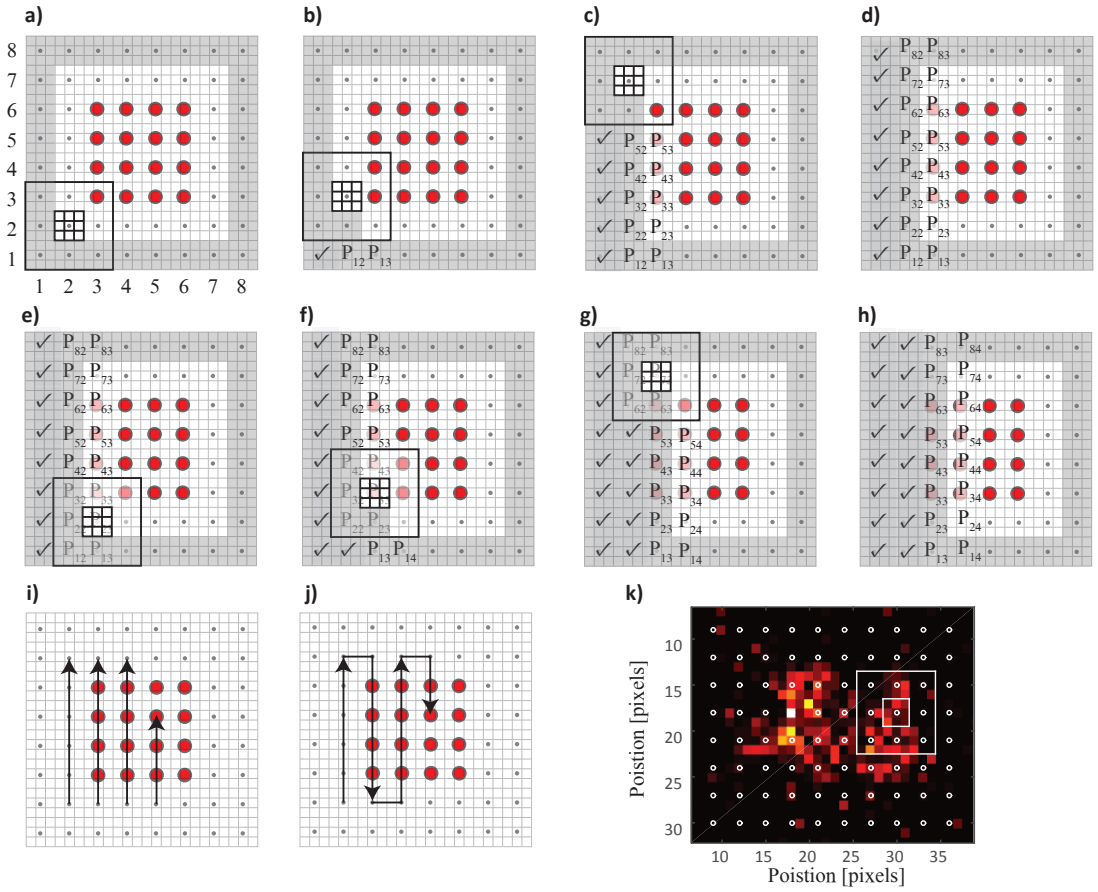

Figure 4.14. *Bayes update scheme for a 2D lattice* **a)-h)** Schematic diagrams showing the steps for the Bayesian update algorithm in a 2D image. The dark shaded regions represent the pixels from which the information has already been used, and the red circles represent the positions where atoms are located. **i,j)** Possible paths for the update algorithm. **k**) Sample of an image generated in the simulation.

4.2.6 Extension to a 2D lattice

The Bayesian algorithm for multiple atoms, presented in the previous section, represents a fast and accurate way to determine the state of an atom and it can be applied to an arbitrarily large 1D lattice. However, experimental systems that deal with large atom numbers typically consist of 2D arrays of optically trapped atoms [21, 22, 24–26]. Also in these systems the implementation of Bayesian techniques could be a powerful tool for the detection of bright atoms. Here we present a brief description of how this can be implemented.

The implementation of a Bayesian algorithm for a 2D system is closely related to the one describe in the previous section. For this reason most of the details are omitted and just an example following the schematic representation in Fig. 4.14 is presented:

a) We use a 2D lattice where only nearest neighbor contamination is present. Two rows of empty sites have been added on the sides of the atom array under study. The pixels corresponding to outermost sites (shaded region in Fig. 4.14a) contain no information . In each iteration, we select a

square patch containing 3×3 lattice sites and only the pixels corresponding to the central lattice site are used in Bayes formula to calculate the probability for the 2^9 combination of states. This guarantees that no pixel containing information on atoms outside the patch is used in the update.

b-d) After each update step, the patch is shifted by one lattice site in the vertical direction. The probability for the dropped sites to contain a bright atom is estimated by marginalization. The correlations between the six remaining atoms inside the patch are preserved and used as priors for the next iteration together with the priors of the newly included sites. After every shift, there are sites on the left side of the array for which no more significant information is available (indicated by a check mark). However, for the other two dropped sites there is still information available in the unevaluated pixels and therefore the probabilities are kept in memory and will be used as priors later when needed. The patch is shifted upwards until the final lattice site of the vertical direction is reached.

e-h) The patch is shifted one lattice site to the right and the whole procedure is repeated starting from the bottom. All the previously calculated probabilities are used as priors when needed.

i) The algorithm is repeated until the last lattice site is reached.

With this algorithm, it is assured that the information contained in each pixel is used only once and that all pixels containing information of a given lattice site are taken into account during the update procedure. The trade-off for this method is that the correlations between the atoms inside the patch and the atoms dropped during the shifts of the patch are lost by the marginalization process. This way to use the information of the pixels is of course not unique (see Fig. 4.14i-j).

In order to quantify the performance of the method, a numerical simulation was implemented using the evaluation path shown in Fig. 4.14i. For the sake of simulation speed we make the simplification to use Poissonian counting distributions with an average of 30 photons per atom and 0.019 CICs per pixel[9] rather than the correct counting. An ideal Airy PSF is used to simulate the imaging system with a FWHM of three pixels. The lattice spacing corresponds to one FWHM of the LSF, which would correspond to a diffraction limited imaging system with a NA ≈ 0.65. Fig. 4.14k shows an example of an image generated. By simulating a lattice with 50% bright atoms at random positions, the state detection error was estimated to be less than 1%. Due to the different magnification and the simplified counting statistics the absolute value of the simulation error obtained should not be directly compared to the results in 1D.

It is important to mention that the mean number of 30 detected photons used in the simulation correspond the number of photons detected in our system with a detection efficiency of $\sim 2.9\%$. However, systems with larger numerical apertures, not only have better resolutions but also larger collection efficiencies. For example in reference [21] approximately 10% of the light scattered by an atom is detected, which would dramatically increase the detection fidelity.

4.3 Summary and conclusions

In this chapter, we have shown that by using a single light beam with clean sigma polarization, it is possible to scatter a large number of photons on a closed cycling transition of optically trapped ^{87}Rb

[9] Contamination from background light can also be included in the CICs.

atoms. This allows us to achieve simultaneous and spatially resolved internal state readout of the atomic ensemble using an EMCCD camera.

We have determined a set of parameters for the illumination light that allows the fast state determination with a fidelity of $98.6 \pm 0.2\%$, which is similar to the push-out method [39, 123] and has the advantage that the atom remains in the trap for $99.0 \pm 0.2\%$ of the cases. Moreover, after the readout process, less than 2% of the atoms change their initial ground state. It can therefore be said that the method is non-destructive not only in the sense that it keeps atoms in the trap, but also that it preserves the initial hyperfine state of the atom. In addition, by re-cooling the atom after the application of a state detection pulse, it is possible to re-use every atom an average of 100 times.

A novel image analysis technique was developed for the state determination of an atom using Bayesian methods, which is particularly powerful for not fully resolved registers of multiple atoms. To this end, we have presented a model that includes the statistics of the detected photons as well as the response from the EMCCD camera, which allows us to reproduce the experimentally measured count histograms for dark and bright atoms under near-resonant illumination.

The Bayesian method was implemented on experimental data for images containing single atoms and atom pairs. Its accuracy for multiple atoms was tested by numerical simulations and compared with the more established method of fitting multiple line spread functions to the fluorescence images. The Bayesian method outperforms the fitting method not only in accuracy but also in computation time, which is relevant for applications that require feedback. We have evaluated the Bayesian image analysis not only for our own experimental parameters but have also estimated the performance for state-of-the-art cold atom imaging systems. The performance of the state analysis improves dramatically with the numerical aperture of imaging optics due to the increase in optical resolution and collection efficiency.

Finally, we have shown how the Bayesian image analysis algorithm can be applied to atoms trapped in two-dimensional arrays. The computational time for this algorithm increases linearly with the number of atoms. This allows for the scalable internal state readout of registers formed by large numbers of atoms.

CHAPTER 5

Manipulation of internal and external states of small atomic ensembles

The coherent control of the internal atomic states is an essential requirement in most of the protocols for quantum information and communication [8, 9, 124], where the information from a flying qubit, e.g. a photon, is mapped onto the internal states of an atom. ^{87}Rb has been shown to be an ideal candidate for quantum information storage since its internal structure allows for the storage of a polarization-encoded qubit [125]. To store this information, a strong photon-atom interaction is necessary [126, 127]. One way to achieve this strong interaction is by confining the light into a small volume, for example inside a high finesse optical fiber based Fabry-Perot resonator [53, 128], which are of particular interest for future experiments in our experimental system (see Chap. 6). In such resonators, the light is confined in a Gaussian mode with a small waist of $\sim 5\,\mu$m creating strong atom-light coupling. The interaction between light and matter can also be enhanced by using a large number of atoms which, due to collective effects, lead to an enhancement of the coupling strength proportional to $\sqrt{N}$ [129–134]. In order to confine many atoms in the small mode volume, it is necessary to implement a compression technique that allows us to increase the density of atoms.

This final chapter is divided into two parts. In the first section I utilize the non-destructive state detection method as the main tool to study the coherent manipulation of small atomic ensembles, first by the usage of microwave radiation and later by a two-photon Raman process. The latter is used to reduce the temperature of the trapped atoms below the Doppler limit by the resolved sideband cooling technique. In the second section, I characterize a compression method that allows the creation of small and dense atomic ensembles [45].

5.1 Coherent manipulation

Coherent manipulation of the ground states of ^{87}Rb can be achieved, e.g. by using electromagnetic radiation in the Microwave (MW) range or in the optical domain by a two-photon Raman process. The coherent coupling to the motional degrees of freedom of atoms trapped in deep potentials can be exploited to manipulate their vibrational state and cool them below the Doppler limit. In this section, the experimental implementation of both tools is presented.

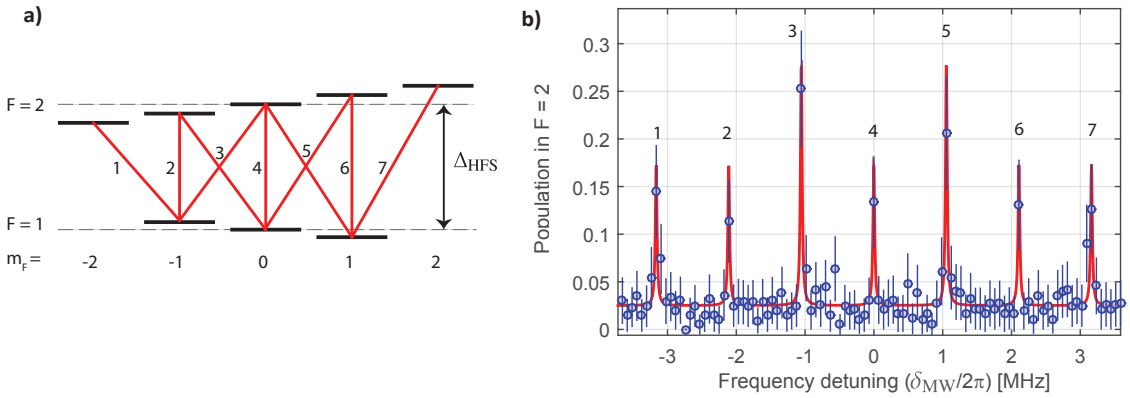

Figure 5.1. *Microwave spectroscopy of ^{87}Rb ground states.* **a)** Ground state levels and allowed MW transitions for ^{87}Rb. **b)** Experimental measurement of the MW spectrum. The red solid line is a fit of 7 equidistant Lorentzian curves to the experimental data.

5.1.1 Microwave manipulation

Coherent superposition of the two ground states of ^{87}Rb can be created by a magnetic field oscillating at the hyperfine splitting frequency $\Delta_{\mathrm{HFS}} = 6.83\mathrm{GHz}$. The dynamics of the two-level system can be described analogously to nuclear magnetic resonance by the optical Bloch equations (see e.g. Refs. [71, 75]). In our experimental system, MW radiation is generated using a Phase Locked Dielectric Resonator Oscillator and a Direct Digital Synthesizer. The radiation is then amplified and sent to the experimental chamber by a home-built helix antenna. This setup is described in detail in Ref. [135].

Microwave spectroscopy

MW radiation can be used to address the nine transitions between the two hyperfine ground states of ^{87}Rb, (see Fig. 5.1a). These transitions can be used to measure the Zeeman splitting induced by the presence of a constant magnetic field, which allows a precise calibration of the fields generated by the compensation coils of the system.

To experimentally measure the Zeeman splitting, a few atoms are illuminated with a beam resonant with the transition $F = 2 \rightarrow F' = 2$. During the illumination process, the magnetic field is set roughly to zero. This creates a mixture of polarization in the illumination light leading to a uniform population of the Zeeman manifold of $F = 1$. Then a bias magnetic field of 1.5 G is applied along the z direction and a square MW pulse with a duration of 500 µs is shone onto the atoms for different frequencies $\omega_{\mathrm{MW}} = \Delta_{\mathrm{HFS}} + \delta_{\mathrm{MW}}$. Fig. 5.1b shows the population in $F = 2$ after the interaction with the MW for different frequencies. The two larger peaks correspond to the degenerate transitions. To measure the population in state $F = 2$ for the data shown in Fig. 5.1b the non-destructive state detection technique was used.

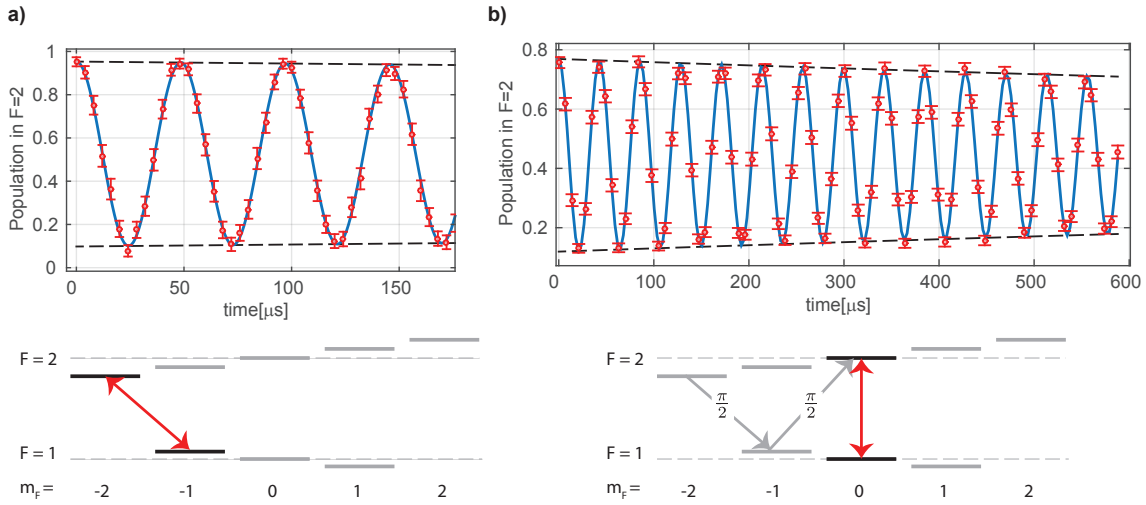

Figure 5.2. *Rabi oscillations between the ground states of ^{87}Rb.* **a)** The top figure shows the experimental measurement of Rabi oscillations (red circles) between the two outermost Zeeman levels (depicted in the lower scheme) and a fit to the experimental data (solid blue). From the fit we obtain $\omega_{\text{Rabi}} = 20.62 \pm 0.02\,\text{kHz}$, and a decay time $\tau = 1.95^{+2.5}_{-0.4}$ ms. The dashed lines represent the exponential decay. **b)** Same as in **a** but for the clock transitions. From the fit we obtain $\omega_{\text{Rabi}} = 23.373 \pm 0.004\,\text{kHz}$, and a decay time $\tau = 2.93 \pm 0.25$ ms. The population transfer process is depicted in the lower scheme.

Rabi oscillations and MW pumping to the clock states.

To coherently manipulate a small ensemble of atoms it is necessary to prepare a well-defined starting Zeeman state. To this end, atoms are optically pumped to state $F = 2, m_F = -2$ using a σ_--polarized light resonant with the transition $F = 2 \rightarrow F' = 2$ and a repumper beam resonant with $F = 1 \rightarrow F' = 2$ with the same polarization. Once all atoms are transferred to the outermost Zeeman state, they interact with the MW field in the same way. A continuous interaction leads to Rabi oscillations between the levels $|2, -2\rangle$ and $|1, -1\rangle$ as shown in Fig. 5.2a. For this measurement, a resonant MW pulse of different duration is shone onto the atoms. From the amplitude of the oscillation, it is estimated that $92.0 \pm 1.8\%$ of the atoms are transferred to the state $|1, -1\rangle$[1]. The population transfer is mainly limited by a short coherence time of only $52 \pm 5\,\mu$s, which was measured by Ramsey spectroscopy (for details regarding this measurement see Ref. [135]).

The simple Zeeman structure of ^{87}Rb can be utilized to transfer the atomic population to the $m_F = 0$ levels by using two consecutive MW $\pi/2$ pulses resonant with the transitions $|2, -2\rangle \rightarrow |1, -1\rangle$ and $|1, -1\rangle \rightarrow |2, 0\rangle$ (see Fig. 5.2b). To characterize the population transfer to the Zeeman state $m_F = 0$, we measure the Rabi flopping between the levels $|2, 0\rangle$ and $|1, 0\rangle$ (see Fig. 5.2b). From a fit to the experimental data it is estimated that $71 \pm 1\%$ of the atoms are transferred to the $m_F = 0$ levels. This transfer is also limited by the short coherence time but it can be improved by using the adiabatic rapid passage technique [136] instead of the simple square $\pi/2$ pulse.

The main advantage of the non-destructive detection method developed in Chap.4 is the reuse of an atom at a fixed position multiple times. For example, Fig. 5.3a shows the trace for a Rabi oscillation using a single atom in the same lattice site. In this case, since just one atom is used, the only possible outcome

[1] From the fit we obtain an amplitude of 0.863 ± 0.015 and we assume a state detection error of $3 \pm 1\%$ for this measurement.

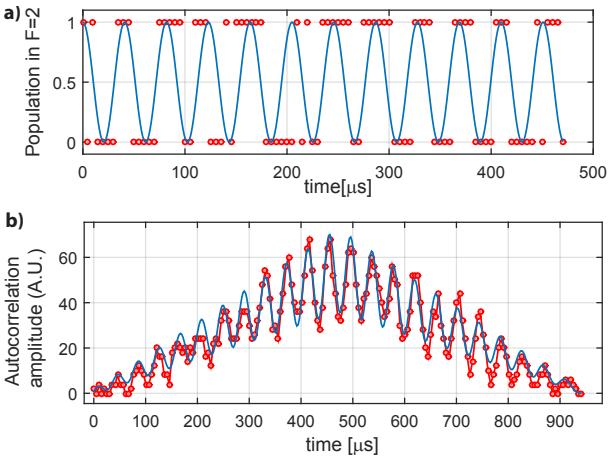

Figure 5.3. *Single atom Rabi oscillation.* **a)** Single atom Rabi oscillation between the state $|2,-2\rangle$ and $|1,-1\rangle$ (red circles) and a reference oscillation (blue line). **b)** Auto correlation function for the single atom trace (red dots) and a fit of Eq.(5.1) to the experimental data (blue curve).

for the state is either 0 or 1. As a reference, in the same figure, the cosine function is plotted with a Rabi frequency of $\omega_{\text{Rabi}}/2\pi = 24.44 \pm 0.01$ kHz, which is estimated by using 1×10^4 atoms for the same measurement.

To visualize the oscillation of the single atom trace we calculate the autocorrelation function (see Fig. 5.3b), which clearly shows the periodic structure. From a fit to

$$g = f(x) * f(x) \quad \text{, where} \quad f(x) = \left[1 + \frac{1}{2}\cos(\omega_{\text{Rabi}} t)\right] \eta(t_{\text{max}} - t)\,\eta(t), \tag{5.1}$$

and $\eta(t)$ is the step function, we obtain a frequency[2] of $\omega_{\text{Rabi}}/2\pi = 24.40 \pm 0.02$ kHz, which is close to the value obtained by using multiple atoms. This method allows a precise determination of the Rabi frequency after an acquisition time of only ~ 5 s by using the same atom. This result can be a useful tool for systems with position-dependent Rabi frequencies.

5.1.2 Raman manipulation

An alternative way to drive coherent transitions is by a two-photon Raman process [137]. In this case, a pair of laser fields, usually referred as the pump and Stokes beams, are used in Λ configuration with two ground states $|\uparrow\rangle, |\downarrow\rangle$ and an excited state $|e\rangle$. The implementation of this configuration for ^{87}Rb is depicted in Fig. 5.4b. When the detuning between the laser beams and the excited state is large compared to the atomic linewidth ($\Gamma \ll \Delta_r$), the excited state can be adiabatically eliminated and the system is reduced to an effective two-level system, where the two ground states are coherently coupled (see e.g. Refs. [138, 139]). At the two-photon resonance ($\delta_R = 0$, see Fig. 5.4b.) the coupling strength is characterized by an effective Rabi frequency given by

$$\Omega_R = \frac{\Omega_{\text{pump}}\Omega_{\text{Stokes}}}{2\Delta_R}, \tag{5.2}$$

where Ω_{pump} and Ω_{stokes} are the Rabi frequencies of each laser beam. In the two-photon resonant case, the population between the two ground states oscillates with the effective frequency Ω_R. If the beams are

[2] This error represents 95% confidence interval obtained directly from a least squares fit using the Jacobian matrix, while for all other values presented in this section the errors are obtained by Bootstrap resampling.

not at resonance ($\delta_R \neq 0$), then the amplitude of the oscillation is reduced and the ground state population oscillates according to

$$P_\uparrow = \frac{\Omega_R^2}{\Omega^2} \sin^2\left(\frac{\Omega}{2}t\right), \tag{5.3}$$

where $\Omega = \sqrt{\Omega_R^2 + \delta_R^2}$ is the generalized Rabi frequency.

Coupling to the atomic motion

In the two-photon Raman process described above, an atom absorbs a photon from one field and coherently emits it into the other. This emission and absorption process leads to a momentum transfer from the photons to the atom. If the two Raman beams are co-propagating, then the absorbed and emitted photons have the same direction leading to a negligible momentum transfer. However, if they have a different orientation, e.g. opposite or orthogonal direction, then the momentum transfer is significant and the coupling to the atomic motion plays an important role.

Ultracold atoms trapped in a standing wave dipole trap are usually confined close to the bottom of the trap. In this regime, the sinusoidal potential is well approximated by a harmonic potential and the quantized motion can be described using the creation and annihilation operators $\hat{a}$ and $\hat{a}^\dagger$. When the atom in the harmonic potential interacts with the two Raman beams, they couple not only the internal states but also to the vibrational levels (see Fig. 5.4c). By choosing the two-photon detuning δ_R accordingly, one can drive coherent transitions between the states $|\uparrow, n\rangle$ and $|\downarrow, m\rangle$. The coupling to the motional degrees of freedom by a two-photon Raman process has been extensively studied in the literature (see e.g. Ref. [89]), here just a brief summary is presented.

The resonant coupling strength between two vibrational states is given by the matrix element [64]

$$\begin{aligned} \Omega_{n\to m} &= \Omega_0 \left|\langle m| \exp\left(i\eta(\hat{a} + \hat{a}^\dagger)\right)|n\rangle\right| \\ &= \Omega_0 \sqrt{\frac{n_<!}{n_>!}} \eta^{|n-m|} L_{n_<}^{|n-m|} \exp\left(-\eta^2/2\right) \end{aligned} \tag{5.4}$$

where $n_< = \min(n, m)$, $n_> = \max(n, m)$, L_n^α are the generalized Laguerre polynomials, η the Lamb-Dicke parameter defined as

$$\eta = \Delta k_R \Delta x = \Delta k_R \sqrt{\frac{\hbar}{2m\omega_{trap}}}, \tag{5.5}$$

were Δx is the extension of the atom in the trap, and $\Delta k_R = |\mathbf{k}_{pump} - \mathbf{k}_{Stokes}|$ [89]. The Lamb-Dicke regime is defined by the condition

$$\eta^2 (2n + 1) \ll 1, \tag{5.6}$$

which means that the extension of the atomic wave function is much smaller than $1/\Delta k_R$. In this regime Eq. (5.4) can be approximated by

$$\Omega_{n\to m\neq n} \approx \Omega_0 \frac{\eta^{|n-m|}}{|n-m|} \sqrt{\frac{n_<!}{n_>!}}, \qquad \Omega_{n\to n} \approx \Omega_0 \left(1 - \frac{2n+1}{2}\eta^2\right). \tag{5.7}$$

Eq. (5.7) indicates that for $|n - m| > 1$, the transition strength is strongly suppressed.

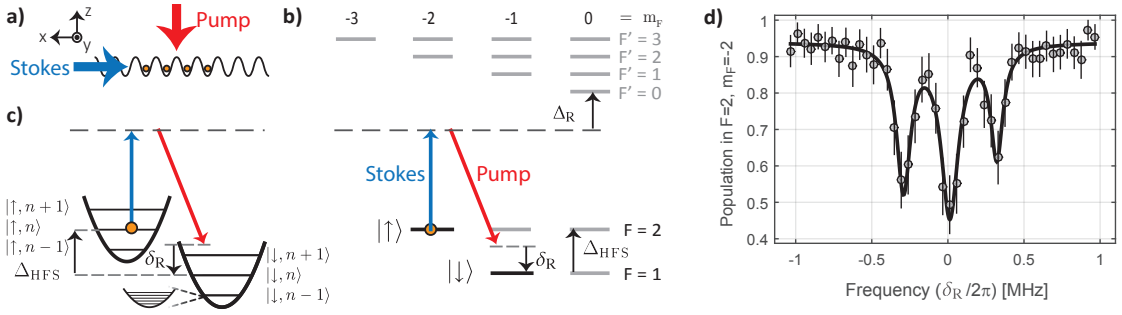

Figure 5.4. *Raman spectroscopy implementation for ^{87}Rb.* **a)** Experimental configuration for the Raman beams illuminating atoms in the optical lattice. **b)** Λ configuration for the two-photon Raman process implemented for the outermost Zeeman levels of the ground states of ^{87}Rb. **c)** Raman transitions including the coupling to the quantized axial vibrational levels. In deep traps, also radial sidebands can be resolved. **d)** Experimental measurement of the motional spectrum using the Raman transitions. The solid line is a fit of three equidistant Lorentzian curves to the experimental data.

Raman sideband spectroscopy

To experimentally implement the two-photon Raman process described above, we use a couple of home-built diode lasers detuned by 6.8 GHz from each other and stabilized using a phase lock loop (described in Ref. [135]). Both lasers are detuned by ~220 GHz from the D_2 line. The Stokes laser propagates along the axial direction with a beam waist of 80 µm, a power of 0.18 mW and is linearly polarized along the z axis. The pump laser is σ_--polarized and it propagates along the z direction with a waist of 310 µm and a power of 2.1 mW (see Fig. 5.4a).

The experimental sequence works in a similar way as for the MW spectroscopy described in Sec. 5.1.1 but now using Raman beams instead of MW radiation. We start by loading a few atoms in the optical dipole trap using 36 mW for each arm ($U_0 \approx 1.6$ mK). The molasses illumination is used to acquire an image and to cool the atoms at the same time. Then, the population is transferred to the state $F = 2, m_F = -2$ by optical pumping followed by an adiabatic reduction of the power of the dipole trap[3] to 9 mW ($U_0 \approx 0.4$ mK). Finally, both Raman beams are turned on for 500 µs and in each repetition the value of δ_R is changed. The recorded spectrum is shown in Fig. 5.4c.

By fitting three equidistant Lorentzian curves to the experimental, we extract a trap frequency of 307 ± 5 kHz, which is close to the theoretical value of $\omega_{axial}/2\pi = 312$ kHz (see Table 2.1). This value for the trap frequency leads to a Lamb-Dicke parameter $\eta \approx 0.16$. For this reason, only the first sidebands are visible. The sidebands also contain information about the temperature of the atom in the trap. By assuming a Boltzmann, distribution one can estimate the mean temperature of an atomic ensemble according to [89]

$$T = \frac{\hbar\omega_{trap}}{k_B \ln\left(\frac{\bar{n}+1}{\bar{n}}\right)}, \tag{5.8}$$

where $\bar{n} = R/(1-R)$ is the mean vibrational quantum number, $R = A_{\Delta n=-1}/A_{\Delta n=+1}$, and $A_{\Delta n=\pm1}$ is the amplitude of the sideband that changes the vibrational state by ±1 [140]. This leads to a mean vibrational number of $\bar{n} = 2.4 \pm 0.9$ and to a temperature of $T = 42 \pm 27$ µK.

[3] We use this power for the trap since for higher values the sidebands are strongly reduced. Furthermore, these settings are used later for resolved sideband cooling.

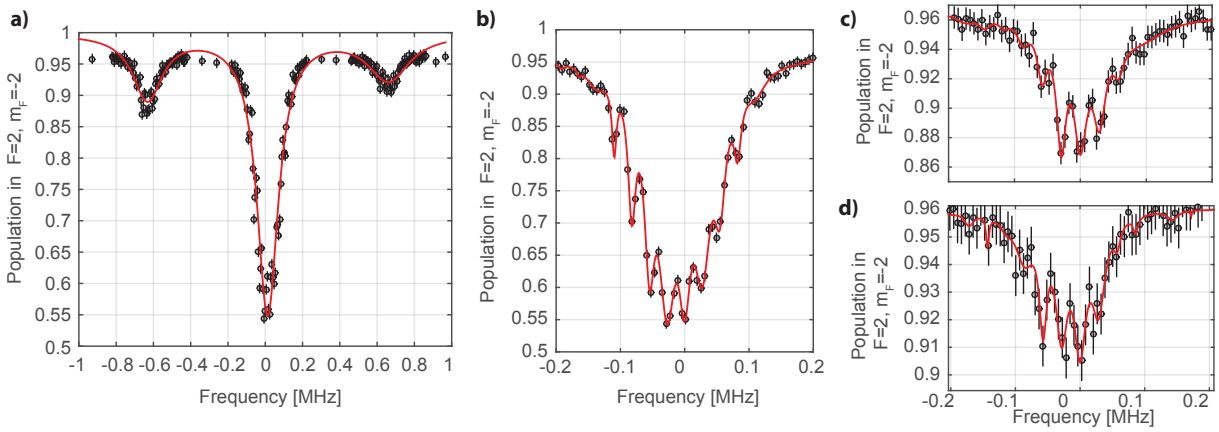

Figure 5.5. *Raman Spectrum in a deep trap for* ^{87}Rb. **a)** Full vibrational spectrum using a power of 36 mW for each arm ($U_0 \approx 1.6$ mK). The solid line is a fit to three equidistant Lorentzian curves **b)** Zoom into the carrier peak. The solid line is a fit to the radial sidebands using 15 equidistant Lorentzian curves. **c)** Same as **b** but for the heating (left) sideband. **d)** Same as **b** but for the cooling (right) sideband.

For higher powers of the dipole trap, the Lamb-Dicke parameter is reduced and, therefore, also the amplitude of the sidebands. This is visible in the recorded spectrum using a power of 36 mW for each arm of the dipole trap presented (see Fig. 5.5a). This configuration of the trap leads to $\omega_{\text{axial}}/2\pi = 645 \pm 1$ kHz, $\bar{n} = 2.3 \pm 0.2$ and $T = 87 \pm 7$ µK. By zooming into the peaks, a finer structure arises from the vibrational levels of the radial motion (see Fig. 5.5b-d). Fitting multiple equidistant Lorentzian curves to the experimental data, we obtain $\omega_{\text{radial}}/2\pi = 27.2 \pm 0.2$ kHz. In both cases, for axial and radial sidebands, the frequencies are slightly larger than the expected value $\omega_{\text{Th,axial}}/2\pi = 623$ kHz, $\omega_{\text{Th,radial}}/2\pi = 24$ kHz (see Table 2.1). A beam waist of 4.75 µm for the dipole trap would explain the measured radial and axial frequency. Therefore, we assume this value as the beam waist for the dipole trap.

Raman sideband cooling

Coherent transfer between the vibrational levels by a two-photon Raman transition provides a powerful tool since the well controlled momentum transfer from a photon to an atom can lead to sub-Doppler cooling. Here we present a brief description of the so-called resolved-sideband cooling cycle implemented in our experimental system. For more details regarding this method see e.g. Refs. [89, 141].

When the two-photon detuning is set on resonance with the cooling sideband, $\delta_R = \omega_{\text{trap}}$, an atom undergoes Rabi oscillations between the states $|\uparrow, n\rangle$ and $|\downarrow, n-1\rangle$. In the absence of decoherence an atom remains in this cycle. To break the cycle, a weak repumper resonant with the transition $F = 1 \rightarrow F' = 2$ with σ_- polarization is introduced (see Fig. 5.6a). Once an atom is coherently transferred by the Raman process to the state $|\downarrow, n-1\rangle$, it is then excited to the state $F' = 2$ by the weak repumper. In the Lamb-Dicke regime, $E_{\text{rec}} \ll \hbar\omega_{\text{trap}}$, an atom cannot gain momentum from the photon recoil and, therefore, during the photon absorption and emission the vibrational state does not change. If the Lamb-Dicke condition is fulfilled, an atom decays from the state $F' = 2$ to $|\uparrow, n-1\rangle$, which reduces the vibrational number by one unit. If the process is repeated many times, an atom reaches its vibrational ground state.

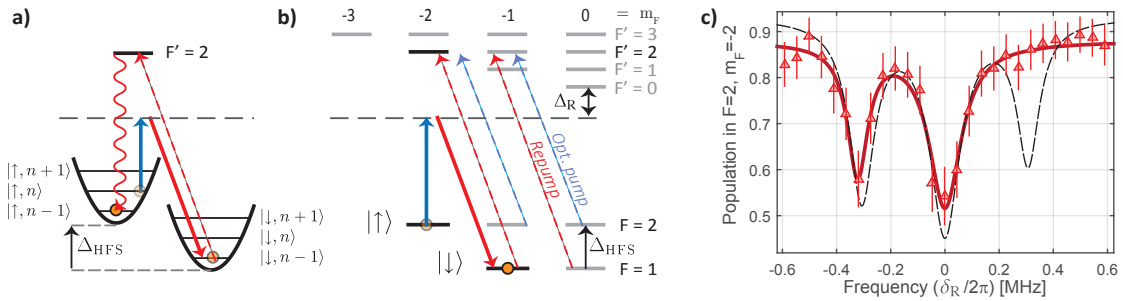

Figure 5.6. *Raman cooling of ^{87}Rb.* **a)** The two-photon Raman process (solid line arrows) coherently transfers the atom from $|\uparrow, n\rangle$ to $|\downarrow, n-1\rangle$, from where it is transferred back to $|\uparrow, n-1\rangle$ by the repumper (red dashed arrow). **b)** Relevant levels of ^{87}Rb and the beams used in the cooling scheme. **c)** Vibrational spectrum after 1 ms of sideband cooling. The solid red line is a fit of three equidistant Lorentzian curves to the experimental data. The black dashed-line is the fit shown in Fig. 5.4d (spectrum without Raman cooling)

This cooling scheme is implemented in the experimental setup using a trap with an axial frequency of $\omega_{\text{axial}}/2\pi = 305\,\text{kHz}$ and the same settings for the Raman beams as described before. The repumper beam has a waist of 1 mm and a power of 12 µW. A weak optical pumping is added to guarantee that the atom remains in the outermost Zeeman levels (see Fig. 5.6b). The optical pumping beam has a waist of 1 mm and a power of 10 µW. From the vibrational spectrum after 1 ms of Raman cooling in Fig. 5.6c, we estimate a mean vibrational number $\bar{n} = 0.054^{+0.058}_{-0.054}$, which leads to a temperature $T < 6\,\mu\text{K}$. For the measurement of the vibrational spectrum, the same settings are used as for the data shown in Fig. 5.4b.

It is important to mention that even though the Lamb-Dicke condition must be fulfilled, in our experimental setup, one cannot arbitrarily increase the trap depth. This comes from the fact that for ^{87}Rb, the dipole trap creates a repulsive potential for the excited states. Therefore, the deeper the trap, more heating is induced during the short time the atom remains in the excited state (see Chap. 3). In our experimental system, it was not possible to cool the atoms in a trap with an axial frequency above 600 kHz.

5.2 Atomic ensemble compression

In the future this experiment aims to achieve a strong interaction of a small atomic ensemble with the electromagnetic field of single photons confined in the small volume of a high finesse optical-fiber-based Fabry-Perot resonator [53, 128] (see Chap. 6). This means that atoms must be confined in a small region of $\sim 10\,\mu\text{m}$. However, the atoms are distributed in a region of about 60 µm when they are loaded from the MOT into the 1D dipole trap. It is therefore necessary to implement a compression scheme to reduce the width of the distribution of atoms in the trap. In this section we explore a technique realized in Ref. [45], where the authors introduce a method to increase the filling factor of atoms trapped in an optical lattice. They characterize their method by measuring the atomic fluorescence using a (non-spatially resolved) photodetector. Here we analyze the method in more detail by using the spatial resolution provided by the EMCCD camera and implementing Raman sideband cooling.

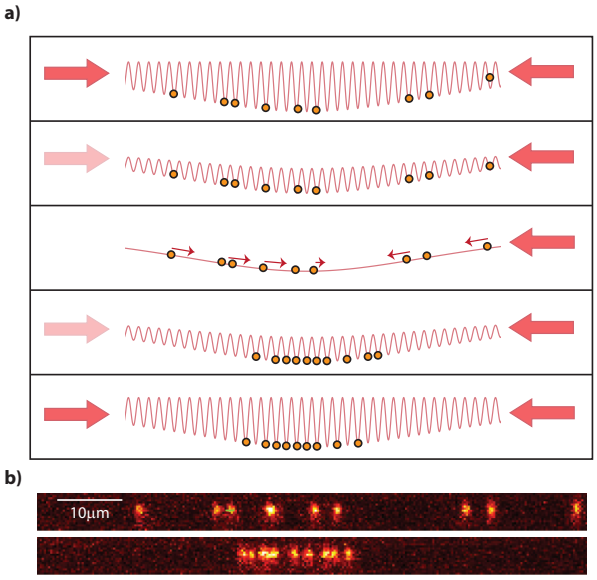

Figure 5.7. *Atomic compression scheme.* **a)** Schematic representation of the compression procedure. The wavelength has been scaled by a factor of 10 for better visualization of the standing wave potentials. In this method, one of the beams is adiabatically switched off for a small time and turned on when the density of atoms is maximum at the center. **b)** Image of atoms in the dipole trap before and after a compression sequence.

5.2.1 Method description

The compression procedure starts by loading a few atoms in a standing wave dipole trap created by two counter-propagating beams. Once the atoms are loaded into the lattice, they are cooled down, e.g. by molasses illumination. After the cooling process, one arm is adiabatically switched off and the atoms are released from their individual potentials. The atoms are now confined in the trap created by the running wave, where the Gaussian profile of the trap attracts the atoms towards the center. By switching on the second arm again at a time $t = T/4$ (being T the oscillation period in the running wave trap) most of the atoms are trapped close to the center. This is procedure is schematically illustrated in Fig. 5.7. The final size of the atomic ensemble depends on the dipole trap parameters and on the initial temperature of the atoms. This dependence is discussed in detail below.

Adiabaticity criteria

To implement this compression scheme, it is necessary to carefully choose the switching time of the trap. On the one hand, if the trap is switched off too fast, the atoms can escape the trapping potential. On the other hand, a slow change limits the repetition rate of any experiment. From classical mechanics, it is known that for an infinitesimally slow change of the trapping potential, the action integral $s = \oint p\mathrm{dx}$ over one oscillation period is conserved. For a harmonic potential this is a simple integral leading to $s = E/\nu$, where $\nu = \omega_{\mathrm{trap}}/2\pi$ is the trap frequency. Therefore, if the trap frequency is changed adiabatically, since s remains constant, the energy changes by a proportional amount, i.e. the trapped atom follows adiabatically the potential change [142]. This statement remains valid in the quantum regime, where for adiabatic changes of the trapping potential the vibrational quantum number is conserved. In a real experiment, however, the changes on the trapping potential cannot be infinitesimally slow. Nevertheless, one can use a more practical criteria: the trap depth must not change significantly during an oscillation [142, 143]. Since the trap frequency depends on the trap depth, the change on the trap frequency during one

oscillation period must be small compared to the frequency, i.e. $\Delta\nu/\nu = \dot{\nu}T/\nu \ll 1$, which reduces to

$$\left|\frac{\dot{\nu}}{\nu^2}\right| \ll 1. \tag{5.9}$$

Harmonic approximation: Compression limit

For atoms located around the center of the trap at a position $z \ll z_R$, where z_R is the Rayleigh length, the trap is well approximated by a harmonic potential. By Taylor expanding the Gaussian potential created by the running, in the harmonic approximation one finds the oscillation frequency [82]

$$\omega_{rw} = \sqrt{\frac{2U_0}{mz_R^2}}. \tag{5.10}$$

In a harmonic potential, all atoms oscillate at the same frequency regardless of their initial position. Furthermore, if all atoms are initially at rest, then all of them will reach the center of the trap at a time $t = T/4$, where $T = 2\pi/\omega_{rw}$ is the oscillation period. In reality, the atoms are not initially at rest and their initial velocity is randomly distributed, which creates a small difference in the time the atoms take to arrive at the center of the trap. Assuming that the initial velocity of the atoms is described by a Maxwell-Boltzmann distribution [82], the width of the spatial distribution of atoms in the trap has a minimum at the time $t = T/4$, with a standard deviation given by

$$\sigma_z = \frac{\sigma_{v_z}}{\omega_{rw}}, \tag{5.11}$$

with σ_{v_z} being the standard deviation of the initial velocity distribution of the atoms. Eq. (5.11) indicates that, as expected, a higher compression is achieved by low temperatures and deep traps.

5.2.2 Experimental implementation

In this section, we implement the compression sequence using two different configurations for the trapping light, first creating a running-wave potential with a depth of 0.3 mK (shallow trap) and later with a depth 1.3 mK (deep trap).

Measurements in a shallow trap

Atoms are loaded in a standing wave trap and cooled down using the optical molasses. The trap is created using $\lambda_{DT} = 880\,\text{nm}$ and a power of 20 mW for each arm leading to a (measured) trap depth of $\sim 0.56\,\text{mK}$ and an axial trap frequency of $\omega_{axial}/2\pi = 367 \pm 10\,\text{kHz}$. Then, one of the arms is switched off by lowering its power during a time $t_{ramp} = 2\,\text{ms}$ following the ramp[4] $P(t) = P_1 \cos^2(\pi t/2t_{ramp})$, while the other is increased up to 36 mW in the same way. The arm of the dipole trap remains off for a time t_{wait} creating a running wave potential[5] with $U_{rw} \approx 0.3\,\text{mK}$. Afterwards the power of the arm is turned on

[4] Following this ramp, the adiabatic condition in Eq. (5.9) is fulfilled for the axial $\left|\dot{\nu}/\nu^2\right| < 2 \times 10^{-2}$ and the radial direction $\left|\dot{\nu}/\nu^2\right| < 1 \times 10^{-3}$ up to $t \approx 1.95\,\text{ms}$.

[5] During this time, a RF-switch (Mini Circuits ZYSWA-2-50DR) is used to attenuate the RF source driving the AOM used for power regulation in order to fully suppress the power of the dipole trap arm.

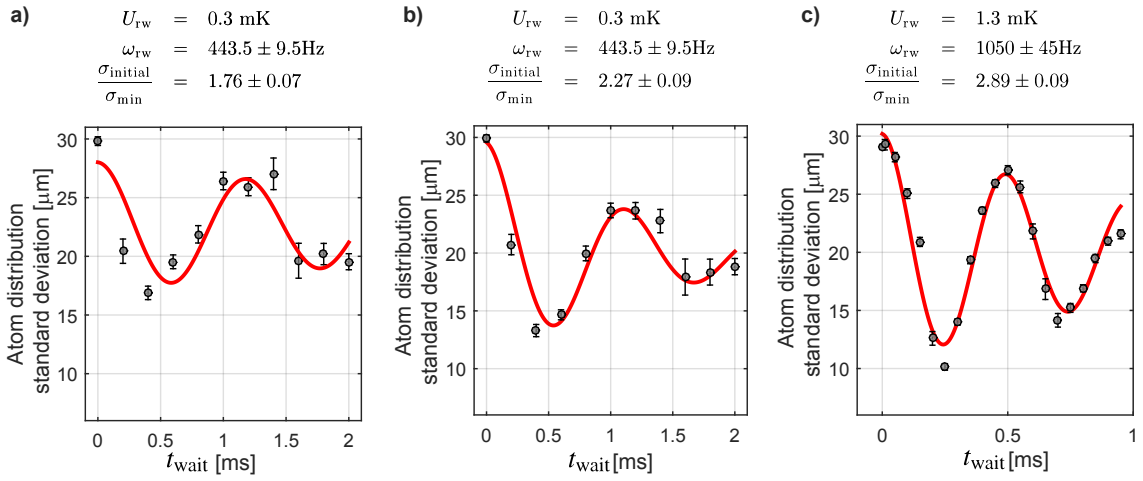

Figure 5.8. *Density oscillations in the running wave.* Standard deviation obtained from a Gaussian fit to the distribution of atoms in the dipole trap after the compression sequence for different waiting times. **a)** 'Using a dipole trap at 880 nm and $P = 36$ mW with molasses cooling. **b)** Using a dipole trap at 880 nm and $P = 36$ mW with Raman cooling. **c)** Using a dipole trap at 860 nm and $P = 112$ mW with molasses cooling. The error bars represent 95% confidence interval obtained by bootstrap resampling.

following the same ramp.

The experiment is repeated for ten different waiting times from 0.05 ms to 2 ms. For each time step, 500 repetitions are performed,where in each repetition we load on average 2.1 atoms. The small number of atoms is necessary to guarantee that there are no multiple occupancies of the same site after the compression sequence, which can lead to losses due to light-induced collisions during the imaging process. From the experimental data, it is possible to fit the distribution of atoms in the lattice by a Gaussian curve and obtain the width for the different waiting times, which is shown in Fig. 5.8a. In the plot, the oscillations in the running wave can be observed. The initial distribution of atoms has a width of 30.2 ± 0.3 µm and reaches a minimum value of 17.1 ± 0.6 µm, which represents a compression of $\sigma_{\text{initial}}/\sigma_{\text{min}} = 1.76 \pm 0.07$.

In order to find the oscillation frequency in the running wave potential we fit the phenomenological function $f(t) = A\left[1 + \cos(2\omega_{\text{rw}}\, t)\exp(-t/\tau)\right] + B$ to the data, where A and B are constants. The factor of two in the cosine function comes from the fact that the variation of the width for the atomic distribution changes at twice the oscillation frequency. From the fit, we extract a frequency of $\omega_{\text{rw}}/2\pi = 443.5 \pm 9.5$ Hz, which is close to the expected oscillation frequency $\omega_{\text{Th, rw}}/2\pi = 423$ Hz obtained by using Eq. (5.10).

The same measurement was repeated using Raman sideband cooling instead of molasses cooling. The variation of the width at different times is shown in Fig. 5.8b. From the data we obtain a maximum compression of $\sigma_{\text{initial}}/\sigma_{\text{min}} = 2.27 \pm 0.09$ and an oscillation frequency of $\omega_{\text{rw}}/2\pi = 421 \pm 11$ Hz. As expected the compression is more efficient since the atoms start with a narrower energy distribution.

Measurement in a deep trap

In the second configuration, we use a dipole trap wavelength of 860 nm, and the power is increased by a couple of tapered amplifiers. The experimental sequence is similar to the one described before for

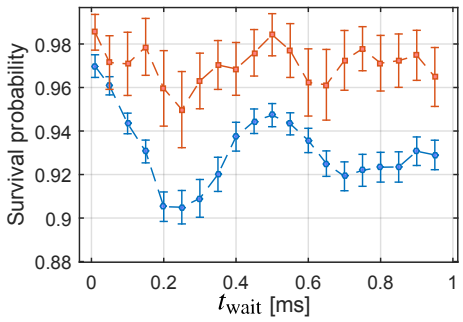

Figure 5.9. *Losses in the compression procedure*. Losses for the set containing initially 1 or 2 atoms (red squares) and initially containing more than 8 atom (blue circles) after a single compression sequence in a dipole trap at 860 nm and $P = 112$ mW with molasses cooling.

molasses cooling but with some subtle differences.

One arm of the dipole trap is ramped down from $P_{1,\mathrm{i}}$ =30 mW to $P_{1,\mathrm{f}}$ =0.16 mW in time $t_{\mathrm{ramp}} = 5$ ms, while the other is increased from $P_{2,\mathrm{i}}$ =30 mW to $P_{2,\mathrm{f}}$ =112 mW. The power on the first beam is reduced following $P_1(t) = (P_{1,\mathrm{i}} - P_{1,\mathrm{f}})\cos^2(\pi t/2t_{\mathrm{ramp}}) + P_{1,\mathrm{f}}$ and $P_2(t)$ is changed such that the intensity $I \propto [\sqrt{P_1(t)} + \sqrt{P_2(t)}]^2$ remains constant. With this restriction, the radial frequency remains unchanged and only the axial frequency must fulfill the adiabaticity condition in Eq. (5.9). Then the power P_1 is set to zero creating a running wave potential with $U_{\mathrm{rw}} \approx 1.3$ mK. Finally the power P_1 is increased to 30 mW in 0.1 ms and the power P_2 is adiabatically reduced to 30 mW in 5 ms. The fast switching time is necessary to trap the atoms at a well-defined time since, in this case, the trap is deeper and atoms move faster. With this procedure we trap about 97% of the atoms in the standing wave potentials.

The variation of the width at different times is shown in Fig. 5.8c. From the data we obtain a maximum compression of $\sigma_{\mathrm{initial}}/\sigma_{\mathrm{min}} = 2.89 \pm 0.09$ and an oscillation frequency of $\omega_{\mathrm{rw}} = 2\pi = 1\,050 \pm 45$ Hz, which is slightly larger than the expected frequency of 967 Hz (obtained by using Eq. 5.10). This might indicate that the beam waist is smaller than the expected value of 4.75 µm since a waist 3% smaller explains the measured frequency.

For this configuration of the running wave, we loaded an average of 6 atoms in each repetition. In order to analyze the losses in the compression process, we select two subsets of data. In the first set, we use images containing just one and two atoms. This guarantees that there are no light induced collisions during illumination and, therefore, the losses are attributed only to the ramping of the traps. In the second set, we select images where initially more than 8 atoms are loaded, which can lead to light-induced collisions. The survival probability for different waiting times is plotted for both sets in Fig. 5.9. For the set containing a few atoms, the losses remain relatively constant (within the error bars) and only at $t = 0.25$ ms they seem to increase slightly. For the set containing many atoms, the losses increase when the density is higher (at $t = 0.25$ ms) indicating that atoms have been trapped in the same lattice site. These losses limit the efficiency of this compression method when the trap contains a large number of atoms.

Effects of the anharmonicity of the trap

In all cases presented above, the compression efficiency is also limited by the anharmonicity of the trap. Far from the center of the trap, the harmonic approximation is not valid anymore. Atoms located initially far to the side are accelerated slower and do not reach the center at $t = T/4$, however they enter the harmonic region. Therefore, in a second compression, most of the atoms oscillate in phase, which leads to a higher compression rate. Fig. 5.10 shows the distribution of atoms in the dipole trap for different

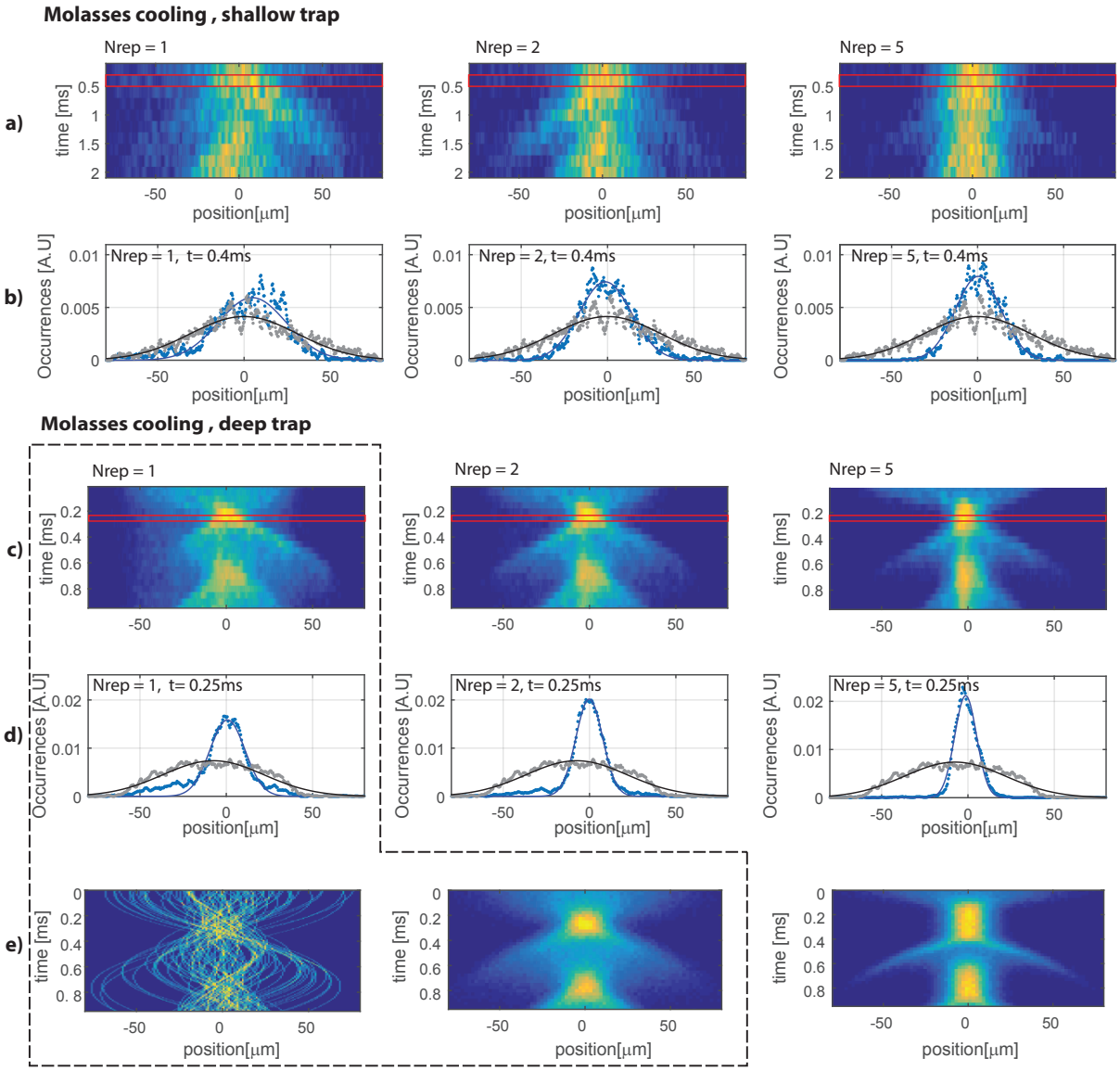

Figure 5.10. *Atom distribution in the lattice after the compression sequence.* **a)** Measured distribution of atoms in the dipole trap for different waiting times after 1, 2 and 5 compressions. Here we use the shallow trap: $\lambda_{\mathrm{DT}} = 880\,\mathrm{nm}$, $P = 36\,\mathrm{mW}$ ($U_{\mathrm{rw}} = 0.3\,\mathrm{mK}$) with molasses cooling. **b)** Initial distribution of atoms in the trap (gray dots) and the distribution after a time $t \approx T/4$ (blue dots, also indicated by the red rectangle in **a**). The solid lines are the Gaussian fits of each distribution. **c**), **d)** Same as **a**,**b** but using the deep trap: $\lambda_{\mathrm{DT}} = 860\,\mathrm{nm}$, $P = 112\,\mathrm{mW}$ $U_{\mathrm{rw}} = 1.3\,\mathrm{mK}$) with molasses cooling. **e)** Results of a Monte Carlo simulation for the deep trap. The left plot shows the trajectory for few atoms moving in the running wave trap, here the origin of the wings can be visualized. The middle and right plots show the result after one and five compressions respectively simulating 10^4 atoms.

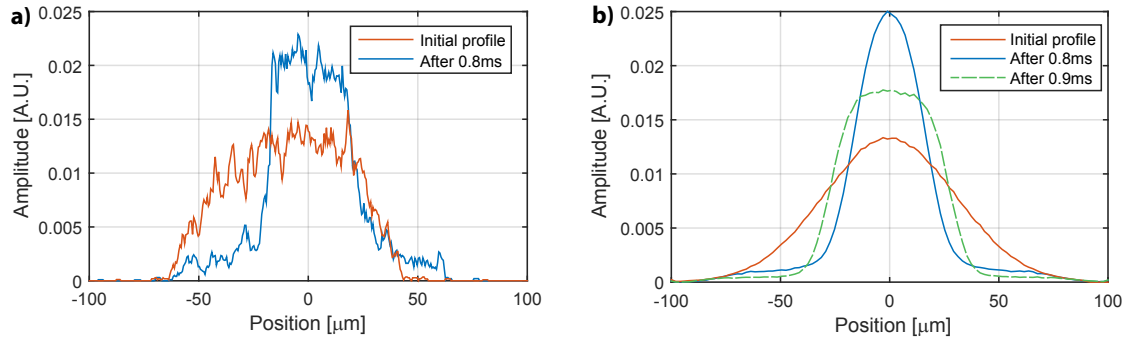

Figure 5.11. *Flat distribution of atoms at the center of the trap.* Distribution of atoms in the dipole trap after $t_{\text{wait}} \approx 0.8T$ for **a)** experimental data and **b)** Monte Carlo simulation in a dipole trap at 860 nm and $P = 112$ mW using molasses cooling.

waiting times and for 1, 2 and 5 iterations of the compression sequence. The atoms that are trapped in the harmonic region oscillate at the same frequency leading to density maxima at times multiples of $t = T/4$, while atoms outside the harmonic region are dephased and lead to the formation of wing structures, which are also visible in a Monte Carlo simulation[6] presented in Fig.5.10e.

Light-induced collisions set an upper limit for the density of atoms in the lattices. When the compression sequence is implemented with a waiting time of $t_{\text{wait}} = T/4$, the density is Gaussian distributed and the probability that many atoms end up in the same lattice site is higher at the center. One can take advantage of the anharmonicity of the trap and turn on the lattice at a time different from $t_{\text{wait}} = T/4$. For example for a time $t_{\text{wait}} \approx 0.8$ ms, the atomic distribution is flatter at the center. This was observed in the experimental data (Fig. 5.11a) and verified in a Monte Carlo simulation (Fig. 5.11b). This effect is, however, not present in a purely harmonic trap. Such flat distribution can help to reduce the losses at the center of the trap.

Compression limit and temperature estimation

In a lattice loaded with few atoms, the losses due to light-induced collisions during the compression sequence are rare. In this case it is possible to use this technique more than one time leading to higher compression efficiency. Another advantage of this method is that the atoms are symmetrically distributed around the center of the trap, where the AC-Stark shift at different positions is minimized. This is especially useful in tightly-focused dipole traps, where the AC-Stark shift significantly modifies the number of scattered photons by atoms trapped at different positions during the molasses imaging process.

Although multiple repetitions create a better compression, the width of final distribution is limited by the initial temperature of the atoms. Fig. 5.12 shows the reduction of the distribution width using up to five repetitions, reaching a minimum value of 6.20 ± 0.13 μm. In the plot, it is visible that the width is already close to its minimum value after two compressions. The minimum width can be used to obtain information about the temperature of the atoms in the running wave potential. Assuming a Boltzmann

[6] The simulation calculates the trajectories of atoms trapped in a 1D running wave for the deep potential with random initial position and momentum that are Gaussian and Boltzmann distributed respectively.

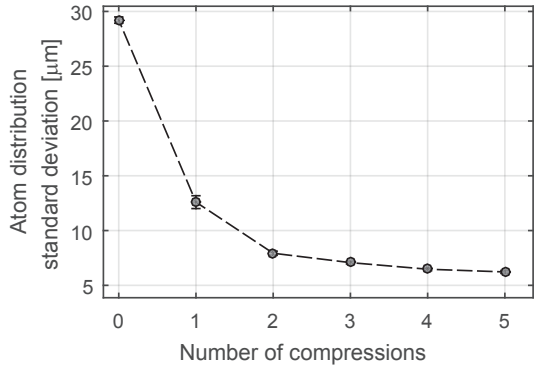

Figure 5.12. *Distribution of atoms in the trap after different iterations of the compression sequence.* The results are obtained for molasses-cooled atoms in a dipole trap at 860 nm with $P = 112$ mW and a free oscillation time $t_{\mathrm{wait}} = T/4$.

distribution for the energy of the atoms and a harmonic approximation for the trap, the distribution of atoms in the dipole trap is described by a Gaussian distribution[143]

$$\rho(z) = \sqrt{\frac{m\omega_{\mathrm{rw}}^2\sigma^2}{2\pi k_{\mathrm{B}}T_{\mathrm{rw}}}}\exp\left(-\frac{m\omega_{\mathrm{rw}}^2 z^2}{2k_{\mathrm{B}}T_{\mathrm{rw}}}\right) \tag{5.12}$$

where the temperature is

$$T_{\mathrm{rw}} = \frac{m\omega_{\mathrm{rw}}^2\sigma^2}{k_{\mathrm{B}}}. \tag{5.13}$$

The measured width of the distribution of atoms in the lattice leads to a temperature of $16 \pm 1\,\mu$K in the trap.

To further compress the atomic distribution, the initial temperature can be reduced by Raman sideband cooling. However, even without Raman cooling, the final density is limited by the light-induced collisions. One way to overcome this limitation is by implementing a 3D lattice, which reduces the probability of multiple occupancies of a single site (see Chap. 6).

5.3 Summary and conclusions

In the first part of this chapter, I have illustrated the usage of the non-destructive method for the internal state determination of ^{87}Rb atoms. Using microwave radiation I have shown that the high fidelity of the state detection technique allows for a precise determination of the Rabi frequency using a single atom at a fixed lattice site in a time of ~ 5 s. The ability to reuse the atom many times represents a big improvement over the push-out technique, which is currently used for the state determination of neutral atoms in optical lattices in other experimental systems.

The trap characteristics were determined by two-photon Raman spectroscopy and later, using resolved-sideband cooling, the axial temperature of the atoms was reduced to $T < 6\,\mu$K. Raman manipulation has some advantages over MW manipulation. Besides the coupling to the atomic motion, higher Rabi frequencies can be achieved using Raman beams, which allows a faster manipulation of the internal states (see e.g. Ref. [135]). The laser beams employed to drive the Raman process can be used, e.g. in combination with a spatial light modulator, to create position-dependent Rabi frequencies. This, combined with the ability to measure position-dependent Rabi frequencies in short times can be a useful experimental tool to study neutral atoms in complex optical lattice structures.

In the second part of this chapter, we have studied the compression of the atomic distribution in the optical lattice. By using molasses cooling in a deep trap ($U_{\mathrm{rw}} = 1.3\,\mathrm{mK}$), it was demonstrated that width of the atomic distribution is reduced almost three times and Raman cooling can improve the compression efficiency even further. We observe that losses by light induced collisions start to limit the achievable densities. Therefore, to create a dense ensemble with a larger number of atoms it is necessary to reduce the multiple occupancies, e.g. by using the anharmonicity of the trap to create a flatter atomic distribution in combination with a 3D lattice to provide more sites. A configuration for such a 3D lattice is proposed in Chap. 6, which will at the same time allow the usage of the non-destructive state detection technique.

CHAPTER 6

Outlook

In this work, I have presented experimental methods that allow for the first time the simultaneous, non-destructive, and spatially resolved, state detection of neutral atoms trapped in a 1D optical lattice by near-resonance fluorescence. For this purpose a novel image analysis technique has been employed that uses Bayesian methods to include information about the experimental system and to make efficient use of the photon counts recorded.

The tools developed here are scalable and can be extended for atoms confined in other trap configurations, including in 3D optical lattices with thousands of atoms [21, 22, 24–26]. One of the conditions for a high-fidelity readout of the internal state, described in Chap. 4, is that the polarization of the optical trap is well aligned with the magnetic field. One way to create a 3D lattice that fulfills this condition is by using three pairs of orthogonal counter-propagating beams. Two of the beams can be linearly polarized along z. The third one, however, cannot be polarized in the same direction but the effect of its polarization can be minimized by using a blue-detuned field since, for a blue-detuned dipole trap, the atoms are confined at the intensity minima. This configuration is illustrated in Fig. 6.1a. In a 3D trap with such characteristics, it should be possible to use near-resonant illumination along the z direction to implement non-destructive state detection. The image analysis technique developed in Chap. 4 is useful not only for the internal state readout but it can also be used for fast determination of the position of atoms in the lattice.

The configuration of a 3D lattice as depicted in Fig. 6.1a is of a particular interest for future experiments in this system. Currently, a high finesse optical-fiber-based Fabry-Perot resonator has been introduced in the system [53, 128], which will allow for strong atom-light interaction between compact ensembles of neutral atoms and single photons on the D2 line. The cavity is directly attached to the aspheric lens holder (see Fig. 6.1b) and connected to the damping stage, which reduces external vibrations caused by high-frequency noise.

The set of aspheric lenses will be used to create a 3D lattice for the atoms inside the resonator; two standing wave red-detuned dipole traps will be created along the x and y direction and a blue-detuned results from the intra-cavity lock light along the z direction (see Fig. 6.1d). The cavity will be used to enhance the interaction between single photons and a small atomic ensemble trapped in the optical lattice inside the resonator.

Optical cavities can be used to determine the internal state of a single neutral atom [40, 41, 144, 145] but they do not provide precise spatial information. Therefore, state detection via the optical cavity can be complemented by the spatially resolved state detection method presented in this work. This will allow

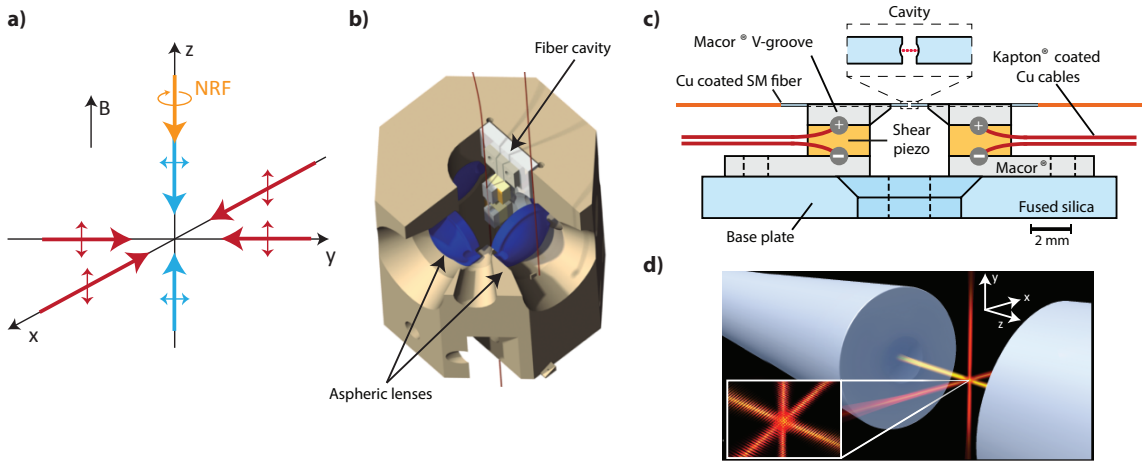

Figure 6.1. *3D optical lattice inside an optical cavity.* **a)** Beam configuration for a 3D optical lattice that allows non-destructive state dependent fluorescence. **b)** Optical-fiber-based cavity combined with the lens system. **c)** Schematic representation of the actively stabilized fiber cavity. **d)** Artistic view of a 3D lattice created inside the resonator.

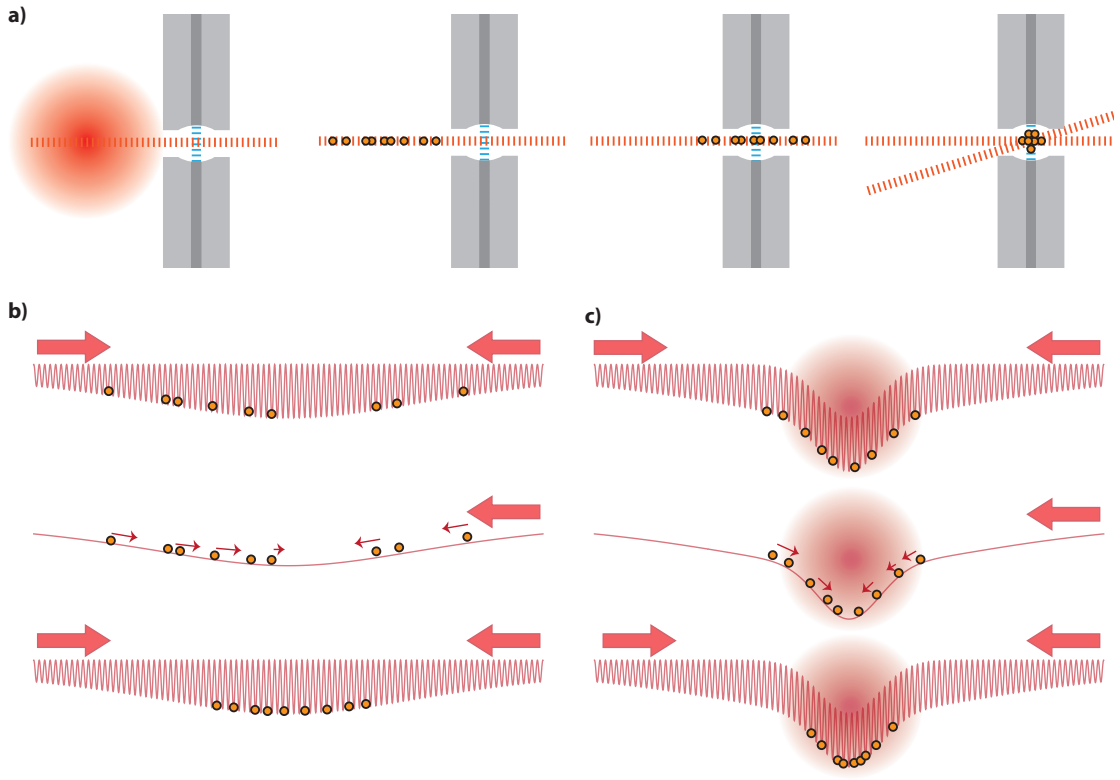

Figure 6.2. *Creation of dense ensembles inside the resonator* **a)** From left to right. Atoms are loaded in the MOT, transferred into the dipole trap, and transported inside the cavity using the optical conveyor belt technique. Then a compression sequence using the crossed traps is applied to increase the density of atoms inside the resonator. **b)** Compression scheme using a single standing wave. **c)** Second compression sequence using the crossed dipole traps.

for a high fidelity position determination of atoms inside the resonator, which is of particular relevance for entanglement schemes [146], where the position determination of atoms is important. Furthermore, the fast position and internal state determination can be used to implement real-time feedback on the system providing it with great versatility.

To place the atoms inside the resonator, they must be transported from a MOT (located ~ 1 mm away) into the cavity. This will be done by the well known optical conveyor belt technique, implemented previously in our research group [66, 123, 147]. However, with this transport alone, only a few atoms can be placed in the interaction region inside the cavity mode, which has a waist of $\sim 5\,\mu$m. To increase the number of atoms in the interaction region, the compression sequence described in Sec. 5.2 will be used (see Fig. 6.2b). In addition to the compression technique presented in Chap. 5, which uses only a single standing wave, the second dipole trap can be used to achieve a better compression efficiency (see Fig. 6.2c). Moreover, the 3D lattice inside the resonator creates more than 100 lattice sites inside the interaction region. This large number of sites minimizes the multiple occupancies of lattice sites reducing the losses during the compression sequence, which should possible to place tens of atoms inside the cavity mode.

The combination of the high-finesse cavity and a small atomic ensemble trapped in an optical lattice is a promising system to implement quantum communication and quantum information storage protocols [9] mentioned in the introduction of this thesis. In long distance communication, light is usually guided using by optical fibers, and the fact that the resonator is already fiber-coupled, reduces losses due to free space to fiber coupling. Using atomic ensembles, in contrast to single quantum systems, leads to collective effects that enhance the interaction between matter and light and can therefore increase storage fidelity. The experimental apparatus and the novel techniques presented in this thesis represent an important step towards the creation of a high-fidelity quantum memory.

APPENDIX A

Lens alignment

We use an aspheric lens (Lightpath 352240, anti-reflection B-coated) with a NA=0.5, a working distance of 5.9 mm, and an effective focal length of 8 mm to create the optical dipole trap and to image single atoms. Although these lenses were designed by the manufacturer for laser diode collimation and the factory design accounts for the diode glass window, they can be used as an objective lens for single atom imaging and the absence of the glass window is compensated by using an extra long-focal distance lens, which restores the aberration-free operation [50]. In this alignment procedure, we use a compensation lens with a focal length of 1000 mm separated by 450 mm from the aspheric lens.

Using a set of 4 aspheric lenses, we create a create a 2D lattice where trapped atoms in a fixed position, to this end we need a lens configuration as shown in Fig. A.1a. To align the perpendicular directions, we use a high quality sphere at the center of the lens system. When the wavefront of a focused laser beam matches the curvature of the sphere, it is back-reflected and the sphere its located at the focal point of the lens. This effect is used to align two lenses to the same focal point (see Fig. A.1b). We use a Si_3N_4 sphere with a diameter of 4 mm from the company *Saphirwerk Industrieprodukte AG*. This is grade 3 sphere, which deviates from a perfect sphere at most by 0.08 µm and has a surface roughness of 0.01µm

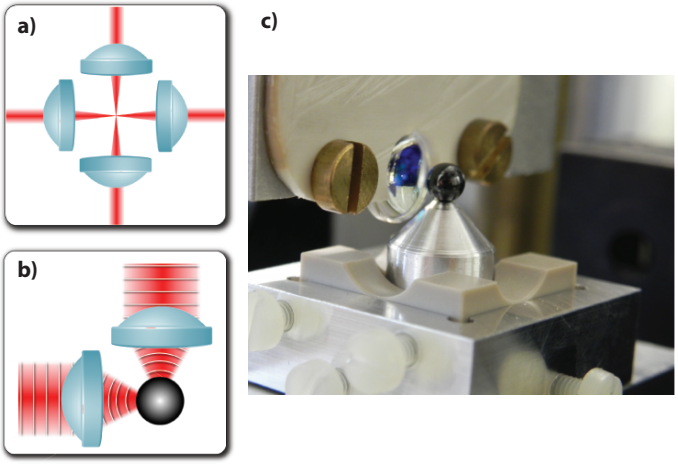

Figure A.1. *Lens alignment using a high-quality sphere.* **a)** Desired lens configuration. **b)** The wavefront of a focused Gaussian beam matches the curvature of a sphere and is reflected. **c)** Si_3N_4 sphere used for the alignment procedure.

The alignment procedure is schematically depicted in Fig. A.2.

a) We use two orthogonal Gaussian beams with a diameter of 10 mm. The beams are collimated using a sharing interferometer[1] and a beam profile camera is used to set a constant height. The beams are retro-reflected using the end mirrors and directed to a screen that is used as a reference (see Fig. A.2a).

b) The sphere is introduced on the beam using a translation stage and its position is monitored by imaging the created diffraction pattern with the beam profile camera (see Fig. A.2b).

c) The correction lenses are placed and the aspheric lenses are introduced using a translation stage. Using the reflected beam on screen as a reference it is possible to roughly align the lenses and all directions and the final positioning along the axial direction is done by using the shear plate interferometer (see Fig. A.2c). After the alignment, the lenses are glued to the upper part of the PEEK holder using a small amount of UV-curing Epoxy glue[2]. We have cured the glue using a UV light bulb of 80 W for $\sim$ 1 hr and then used small drops of Epotek 353ND glue, which was cured it at 150 degrees[3] for 3 hrs.

d) Finally, to align the last two lenses we use the transmitted beam to position the lenses. First using the reflected image on the screen and finally using the shear plate of the transmitted beam (see Fig. A.2d).

[1] Shearing Interferometer model SI100 from Thorlabs, Inc.
[2] Epotek OG116
[3] It is important to mention that the 353ND glue becomes extremely watery when heated up.

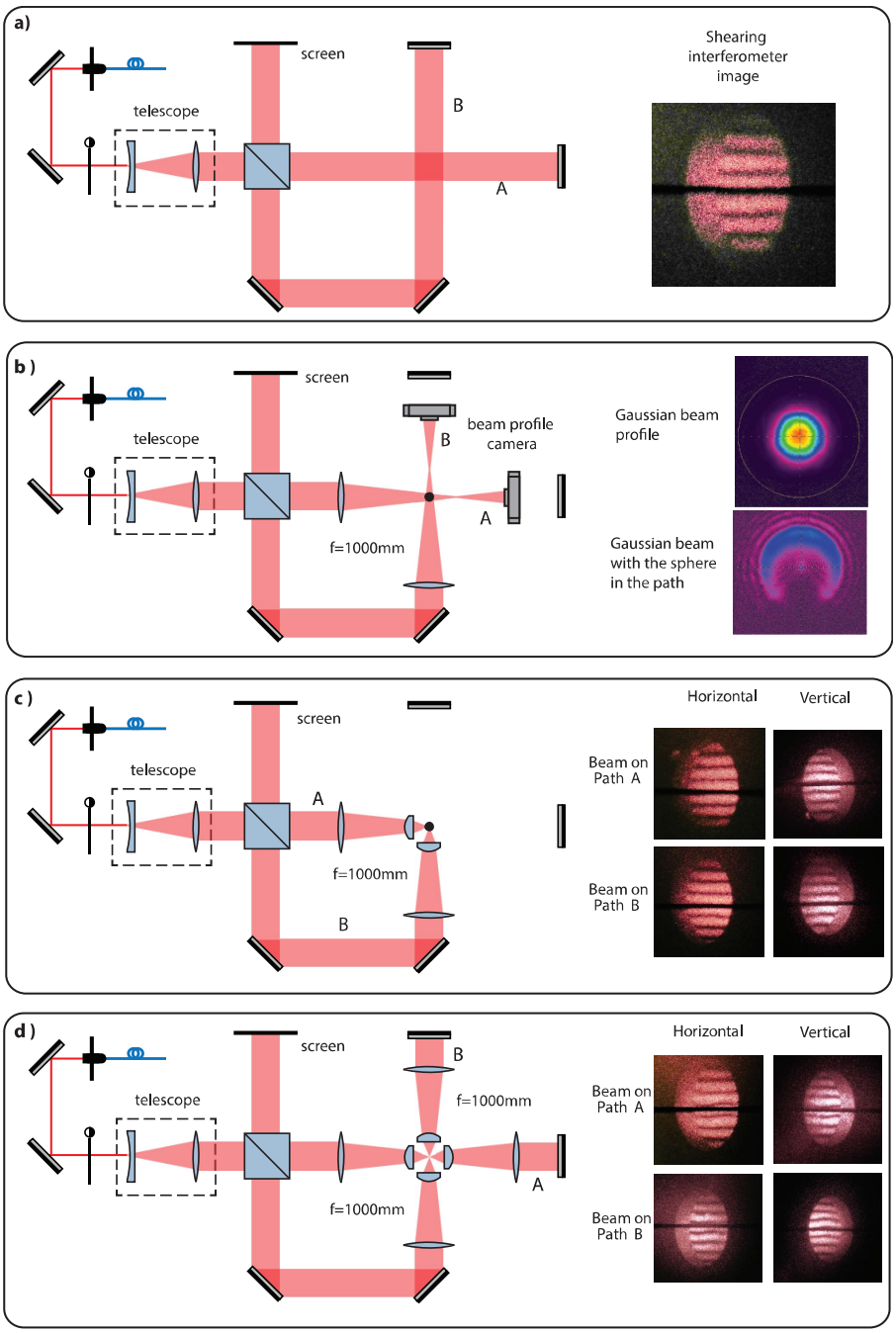

Figure A.2. *Lens alignment procedure.***a)** 10 mm diameter beams are collimated and aligned with respect to the table. **b)** Compensation lenses are placed and the sphere is introduced by using the beam profile camera to measure its position. **c)** The aspheric lenses are aligned by monitoring the reflected signal in the screen and using the shear plate interferometer. **d)** The two last aspheric lenses are aligned.

APPENDIX B

Crossed dipole traps

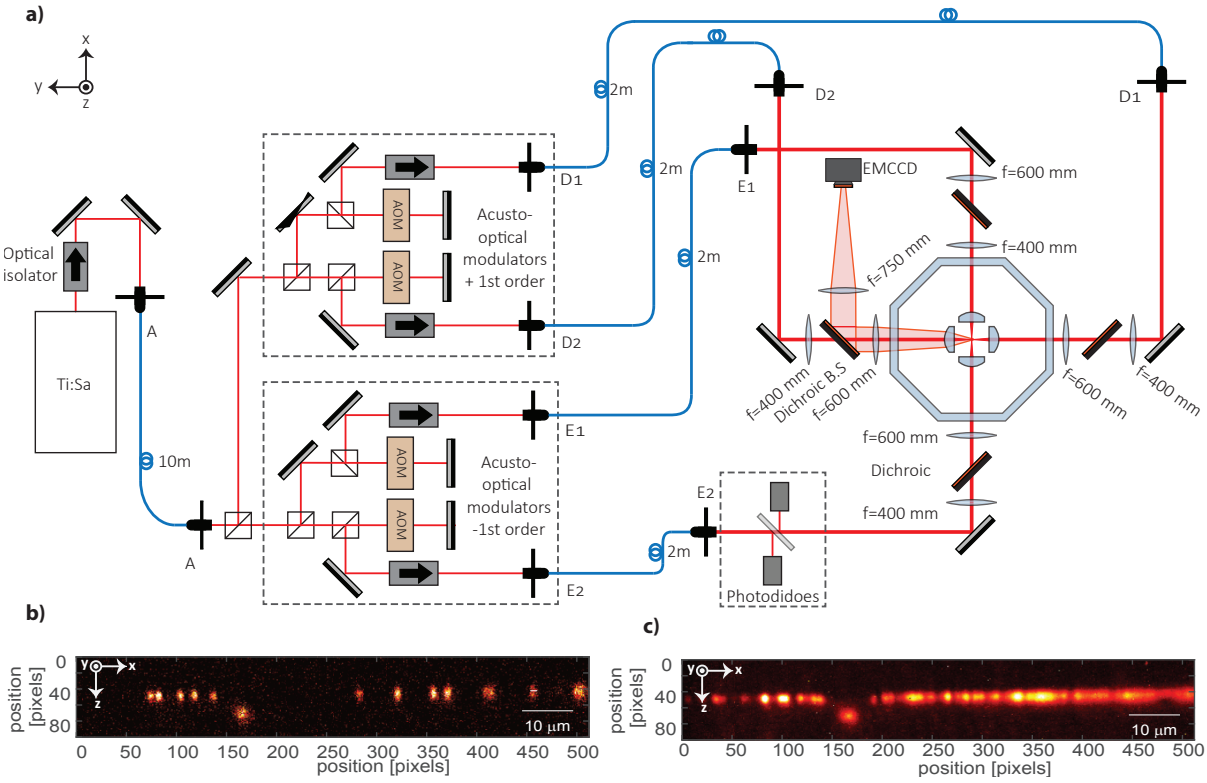

Figure B.1. *Crossed dipole traps.* **a)** Simplified setup for the creation of a small 2D optical lattice. After the optical fiber (A) the beam is split into two parts. Each part is split again and shifted using a couple of AOM's (in double-pass configuration) and then coupled to optical fibers (E_1,E_2, D_1, D_2). After the optical fibers, the light is focused using the aspheric lenses. Light from the atoms is collected using the same lenses in order to image the atoms using the EMCCD camera. The setup for the MOT beams is not shown. **b)** Image of atoms in 1D standing wave along the x direction and a running wave along the y direction. In the image, only the beam from the fiber D_2 was used to create the running wave along y. The beam has a small offset for better visualization of both traps. All beams have a waist of $\sim 5\,\mu$m **c)** Same as **b** but in this case the image is an average of 700 individual pictures.

APPENDIX C

Monte Carlo simulation for the heating dynamics

Photon scattering events are determined by a scattering rate R_{sc}, which in general is not constant. For an atom trapped in a deep dipole potential, the photon scattering events depend on the atoms' position due to the position dependent AC-Stark shift. Furthermore, the multilevel structure of the atom introduces additional scattering channels from which the atom can decay into the dark state $|F = 1, m_F = -1\rangle$. In order to simulate the dynamics of the system, a Monte-Carlo simulation is implemented.

C.1 Position dependent scattering rate

If the scattering rate has an upper bound, i.e. $R_{\mathrm{sc}}(\mathbf{r}) \leq R_{\mathrm{max}}$, the bound can be used to randomly determine the time it takes to scatter a photon. To this end, we use an algorithm by Zipkes et al. [148] that does not suffer from time discretization errors. It works as follows:

1. The atom starts at a position $\mathbf{r}_0$ at time $t = 0$.
2. The system is advanced a time τ that is drawn according to the distribution
$$P_{\mathrm{max}} = R_{\mathrm{max}} \exp(-R_{\mathrm{max}} t).$$
3. At the new position, the re-scaled rate is calculated
$$g = \frac{R_{\mathrm{sc}}(\mathbf{r}(\tau))}{R_{\mathrm{max}}}$$
4. The scattering event will occurred with a probability g. To decide if the event takes place or not, a random number r is drawn from a uniform distribution in the interval $[0, 1)$.
   - If $r < g$, the event has taken place.
   - If $r > g$, the event has not taken place, then go back to 2

C.2 Multiple rates

When two different random events (independent from each other) described by exponential distributions with rates R_1 and R_2 take place, one way to decide which event takes place can be implemented as follows:

1. Draw a random time from each distribution and take the lowest value.

$$\begin{aligned} \tau_1 &\leftrightarrow R_1 \exp(-R_1 t) \\ \tau_2 &\leftrightarrow R_2 \exp(-R_2 t) \\ \tau &= \min(\tau_1, \tau_2) \end{aligned}$$

2. If $\tau = \tau_1$ event 1 has occurred otherwise it was event 2.

With this procedure, both events combined are described by an exponential distribution with a total rate $R_1 + R_2$ (see e.g. Ref. [149]) but the individual occurrences are still described by the individual rates. If the rates are position dependence, but upper-bounded, then an event takes place with a probability g in the same way as in C.1.

The extension to more than two random events is straightforward.

C.3 Off-resonant scattering

we have experimentally measured that the π component is the main contribution to the polarization impurity (see App. 5.1.1). Furthermore, after the state detection process, only a few percent of the atoms are pumped into the dark state (see Sec. 4.1.3), showing that only a few events will occur due to the polarization impurity. This allows us to model the off-resonant scattering process with a simplified model: just the π component for the polarization is considered. In addition, we assume that the events are instantaneous, i.e. the dynamics while the atom is in the "wrong" m_F state is neglected.

With the assumptions mentioned above, the simplified off-resonant process is implemented as follows:

1. The atom starts in the state $|F = 2, m_F = -2\rangle$
2. The π-polarization impurity can transfer the atom to a new state $|\phi\rangle$ with a probability P_ϕ, where

$$P_\phi = \frac{R^\pi_{sc|2,-2\rangle\to|\phi\rangle}(\mathbf{r})}{R^\pi_{sc|2,-2\rangle\to|2,-2\rangle}(\mathbf{r}) + R^\pi_{sc|2,-2\rangle\to|2,-1\rangle}(\mathbf{r}) + R^\pi_{sc|2,-2\rangle\to|1,-1\rangle}(\mathbf{r})}.$$

   for $\phi = |2,-2\rangle,\ |2,-1\rangle,\ |1,-1\rangle$ and

$$R^Q_{sc,|i\rangle\to|f\rangle} \approx \frac{8\pi\alpha^2\omega_L^3 I}{3\hbar c^2}\left|\sum_{m,q}\frac{\langle f|\,\mathbf{r}_q\,|m\rangle\langle m|\,\mathbf{r}_Q\,|i\rangle}{\omega_m - \omega_L + i\Gamma/2}\right|^2 \tag{C.1}$$

   is the Kramers-Heisenberg formula [150], where α is the fine structure constant, ω_L is the angular frequency of the laser light, I is the incident light intensity, Q indicates the incident laser polarization, q the scattered light polarization, i, m, and f, are the initial, intermediate and final states. The

Kramers-Heisenberg formula accounts for the effects of interference due to scattering from the excited states $F' = 3$ and $F' = 2$..

3. For $|\phi\rangle = |F = 1, m_F = -1\rangle$ the atom has been transferred to the dark state and simulation is over.

4. For $|\phi\rangle = |F = 2, m_F = -1\rangle$ the atom has changed its Zeeman level. If this is the case, then one of the following two events can happen:

   - Go to state $|F = 2, m_F = -2\rangle$ with a probability P_{back}
   - Go to state $|F = 1, m_F = -1\rangle$ with a probability $1 - P_{\text{back}}$, where

$$P_{\text{back}} = \frac{R^{\sigma}_{sc_{|2,-1\rangle\to|2,-2\rangle}}(\mathbf{r})}{R^{\sigma}_{sc_{|2,-1\rangle\to|2,-2\rangle}}(\mathbf{r}) + R^{\sigma}_{sc_{|2,-1\rangle\to|1,-1\rangle}}(\mathbf{r})}. \tag{C.2}$$

C.4 Monte Carlo loop implementation for the weak resonant field

Here we implement the experimental situation described in Sec. 3.1.3. A neutral atom trapped in an optical dipole trap interacting with a weak resonant field. In this case the effects of polarization contamination are completely neglected.

1. The atom is initially in its ground state. The initial energy E_0 is drawn from a Boltzmann distribution. $\mathbf{r}_0$ and $\mathbf{p}_0$ are randomly chosen according to the initial energy.[1]

2. Calculate the maximum scattering rate $R_{\max}$ for the given energy E_i. There are two cases.

   - If the atom is in resonance with the near resonant field at some energy-accessible position, then $R_{\max} = R_{\text{sc}}(\Delta = 0)$.
   - If the atom is never in resonance, there is a detuning $\Delta_{\min}$ that is the closest point to resonance. In such a case $R_{\max} = R_{\text{sc}}(\Delta_{\min})$, where the scattering rate is

$$R_{\text{sc}}(\Delta(\mathbf{r})) = \left(\frac{\Gamma}{2}\right)\frac{s}{1 + 4\left(\frac{2\pi\Delta(\mathbf{r})}{\Gamma}\right)^2 + s}.$$

   Here s is the saturation parameter $s = I/I_0$, and $\Delta(\mathbf{r})$ is the position dependent detuning.

3. The system is advanced a random time t_0 drawn from the distribution

$$\rho(t) = R_{\max}\exp(-tR_{\max})$$

4. Calculate the new position and momentum, $\mathbf{r}_1$, $\mathbf{p_1}$ for the atom after the time t_0, i.e. solve the equations of motion for the potential $U_g(\mathbf{r})$

[1] To obtain initial random positions for the given energy we first set $\mathbf{r} = 0$ and all the energy is kinetic. Then we choose a random time t_r in the interval $[0, T)$, where T is the period of oscillation in the radial direction. Numerically solve the equation of motion for the ground state potential for the time t_r and used the obtained momentum and position as the initial values.

5. A scattering event takes place with a probability

$$g = \frac{R_{sc}(\mathbf{r}_1)}{R_{\max}}$$

   - If there was not scattering event then $\mathbf{r}_0 = \mathbf{r}_1$ and $\mathbf{p}_0 = \mathbf{p}_1$ and go back to 3.
   - If there is a scattering event, then continue.

6. The atom remains in the excited state for a time t_e drawn from an exponential distribution

$$\rho(t) = \Gamma \exp(-\Gamma t)$$

   where Γ is the natural decay rate. The position and momentum of the atoms is updated by solving the equations of motion for $U_e(\mathbf{r})$.

7. The simulation terminates in the following cases:

   - The atom has left the trap.
   - The total simulation time has reached the limit .

   If none of the previous is satisfied, then the atom is again in its ground state and ,therefore, go back to 2.

C.5 Monte Carlo loop implementation for the dressed-state potentials

This Monte Carlo simulation describes an atom trapped in the dressed state potential created by the interaction with a near resonant field with an intensity I that contains a small polarization contamination $I_\pi = I/250$.

1. Initial atomic parameters:

   - Hyperfine state: $|F = 2, m_F = -2\rangle$.
   - Dressed state : $|+, N\rangle$ for red-detuning of the NRF.

     $|-, N\rangle$ for blue-detuning of the NRF.

   - E_0 is drawn from a Boltzmann distribution. $\mathbf{r}_0$ and $\mathbf{p}_0$ are randomly chosen according to the initial energy.[2]

2. Calculate maximum rates for the current energy E:

   - Scattering rates for π off-resonant pumping, using Eq. (C.1).
   - Decay rates for the current dressed state according to Eq. (3.21).

[2] To obtain initial random positions for the given energy we first set $\mathbf{r} = 0$ and all the energy is kinetic. Then we choose a random time t_r in the interval $[0, T)$, where T is the period of oscillation in the radial direction. We numerically solve the equation of motion for the ground state potential for the time t_r and use the obtained momentum and position as the initial values.

3. Draw random times from the four distributions.

$$\Gamma_{\pm\pm,},\ \Gamma_{\pm\mp},\ R^{\pi}_{sc_{|2,-2\rangle\to|2,-1\rangle}},\ R^{\pi}_{sc_{|2,-2\rangle\to|1,-1\rangle}}.$$

   where the signs for Γ_{ij}, defined in Eq. (3.21), must be chosen according to the current dressed state and $R^{\pi}_{sc\,|\text{initial}\rangle\to|\text{final}\rangle}$ is calculated using Kramers-Heisenberg formula in Eq. (C.1). Then find the minimum time τ. Identify the rate function that corresponds to τ. This will be labeled by $R(\mathbf{r})$, and its upper bound $R_{\max}$.

4. Advance the system a time τ, i.e. solve equation of motion for the current dressed state potential Eq. (3.18)

5. The scattering event will take place with a probability $g = R(\mathbf{r})/R_{\max}$. If the event doesn't take place then go back to 3.

6. Update the new hyperfine or dressed state according to the scattering event that has occurred. Add the photon recoil to atomic momentum and calculate total energy.

7. The simulation terminates in the following cases:

   - The atom has left the trap.
   - The total simulation time has reached the limit.
   - The hyperfine state is $|F = 1, m_F = -1\rangle$

   If none of the previous conditions is fulfilled then continue.

8. If the hyperfine state is $|F = 2, m_F = -2\rangle$ go to 2.

9. Change the hyperfine state to either $|F = 2, m_F = -2\rangle$ with probability P_{back} or $|F = 1, m_F = -1\rangle$ with probability $(1 - P_{\text{back}})$, where P_{back} is defined in Eq. (C.2)

10. If the hyperfine state is $|F = 1, m_F = -1\rangle$ then the simulation stops, else go to 2.

APPENDIX D

Measuring polarization contamination

In every experimental system, it is desirable to identify the sources of experimental imperfections. In our system, one of the key elements is the polarization of the light. It is meaningful to know what are the possible reasons for light polarization contamination. For example, if the circularity of the light is badly prepared it gives rise to a small degree of ellipticity leading only to a σ contamination. However, magnetic fields imperfections create both σ and π components. Therefore, both sources create a different kind of light contamination. Here I present a measurement that allows us to characterize the polarization contamination present in σ_- polarized light.

When an ensemble of atoms, prepared in the state $F = 2, m_F = -2$, is illuminated with σ_- light, then any polarization impurity transfers them into the dark state $F = 1$ (see Fig. D.1b). If a large number of atoms is transferred to the dark state, the final distribution of Zeeman levels in $F = 1$ can be used to obtain information about the polarization contamination.

For this purpose, atoms are loaded into the dipole trap of 1 mK and then optically pumped to the state $F = 2, m_F = -2$. The dipole trap is then adiabatically lowered to $220\,\mu$K, where an AC-Stark shift of $2\pi \times 3.3$ MHz is expected. A σ_- beam resonant with the transition $F = 2 \rightarrow F' = 2$ is turned on for 40 ms with an intensity of $0.9 I_{\text{sat}}$ [1].

To measure the final distribution of Zeeman states we perform microwave spectroscopy on the non-degenerated transitions $|1,-1\rangle \rightarrow |2,-2\rangle$, $|1,0\rangle \rightarrow |2,0\rangle$, $|1,1\rangle \rightarrow |2,2\rangle$. From the microwave spectrum we estimate that $98.7 \pm 0.5\%$ of the population is transferred to $m_F = -1$ (see Fig. D.1a).

Using a Monte Carlo simulation that takes into account all the possible excitation and decays channels it is possible to calculate the polarization ratio σ_+/π from the ratio of the population in the Zeeman levels $N_{m_F=0}/N_{m_F=-1}$. From the amplitudes obtained in the microwave spectrum, we estimate that $\sigma_+/\pi = 4.8(1.9)\%$. This means that the main polarization impurity in our system is the linear component (see Fig. D.1e).

[1] We use as a reference the saturation intensity for the $F = 2, m_F = 2 \rightarrow F' = 3, m_F = 3$ $I_{\text{sat}} = 1.67\,\text{mW/cm}^2$ [151]

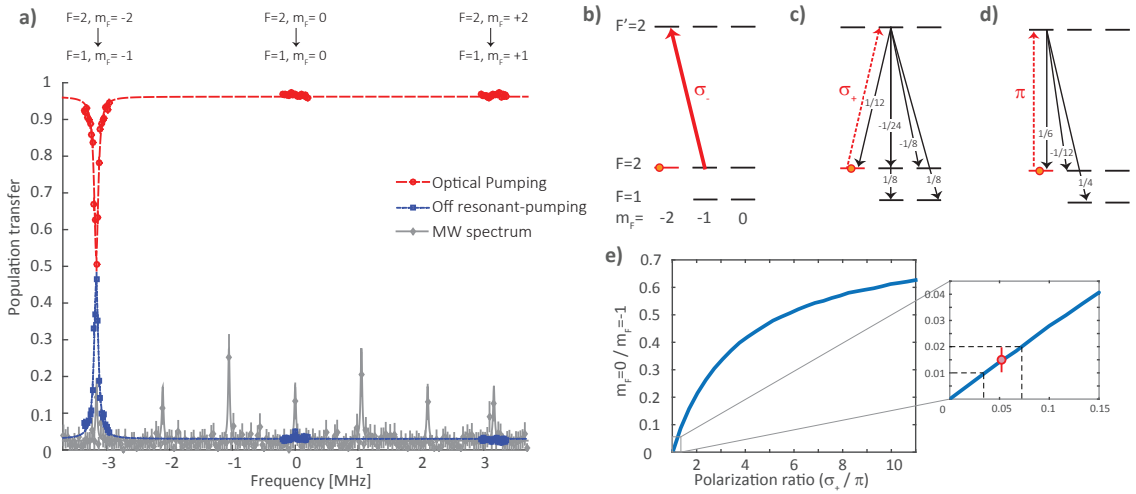

Figure D.1. *Off-resonant pumping characterization.* **a)** Three microwave spectra. The gray diamonds and solid lines are the full spectrum of uniformly distributed m_F states in the ground state $F = 1$. The red circles and long-dashed line denote the spectrum after optical pumping to $F = 2, m_F = -2$. The blue squares and small-dashed line denote the spectrum after 40 ms of resonant σ_- light illumination. **b)** Laser configuration. The thick arrow represents the main polarization σ_- and the two dashed lines represent the polarization impurities σ_+ and decay channels for **c)** σ_+ and **d)** π excitation respectively. The Clebsch-Gordan coefficients are included in each transition. **e)** Numerical calculation for the m_F distribution for different ratios of the polarization contamination components. The shows the measured value obtained by microwave spectroscopy.

References

[1] G. S. Vernam,
Cipher printing telegraph systems: For secret wire and radio telegraphic communications,
AIEE, Journal of the **45**.2 (1926) 109.

[2] V. Scarani et al., *The security of practical quantum key distribution*,
Reviews of modern physics **81**.3 (2009) 1301.

[3] C. E. Shannon, *Communication theory of secrecy systems*,
Bell system technical journal **28**.4 (1949) 656.

[4] W. K. Wootters and W. H. Zurek, *A single quantum cannot be cloned*,
Nature **299**.5886 (1982) 802.

[5] C. H. Bennett and G. Brassard, *Quantum cryptography: public key distribution and coin tossing*,
Conf. on Computers, Systems and Signal Processing (Bangalore, India, Dec. 1984) (1984) 175.

[6] C. H. Bennett et al.,
Teleporting an unknown quantum state via dual classical and Einstein-Podolsky-Rosen channels,
Phys. Rev. Lett. **70**.13 (1993) 1895.

[7] A. K. Ekert, *Quantum cryptography based on Bell's theorem*, Phys. Rev. Lett. **67**.6 (1991) 661.

[8] L.-M. Duan et al.,
Long-distance quantum communication with atomic ensembles and linear optics,
Nature **414**.6862 (2001) 413.

[9] N. Sangouard et al., *Quantum repeaters based on atomic ensembles and linear optics*,
Reviews of Modern Physics **83**.1 (2011) 33.

[10] A. I. Lvovsky, B. C. Sanders and W. Tittel, *Optical quantum memory*,
Nature photonics **3**.12 (2009) 706.

[11] R. Grimm, M. Weidemüller and Y. B. Ovchinnikov, "Optical Dipole Traps for Neutral Atoms",
ed. by B. Bederson and H. Walther, vol. 42,
Advances In Atomic, Molecular, and Optical Physics, Academic Press, 2000 95.

[12] D. Jaksch and P. Zoller, *The cold atom Hubbard toolbox*, Annals of physics **315**.1 (2005) 52.

[13] M. Lewenstein et al.,
Ultracold atomic gases in optical lattices: mimicking condensed matter physics and beyond,
Advances in Physics **56**.2 (2007) 243.

[14] I. Bloch, J. Dalibard and W. Zwerger, *Many-body physics with ultracold gases*,
Reviews of Modern Physics **80**.3 (2008) 885.

[15] A. J. Kerman et al., *Beyond optical molasses: 3D Raman sideband cooling of atomic cesium to high phase-space density*, Phys. Rev. Lett. **84**.3 (2000) 439.

[16] D.-J. Han et al., *3D Raman sideband cooling of cesium atoms at high density*,
Phys. Rev. Lett. **85**.4 (2000) 724.

[17] A. Reiserer et al., *Ground-State Cooling of a Single Atom at the Center of an Optical Cavity*,
Phys. Rev. Lett. **110** (22 2013) 223003.

[18] S. Kuhr et al., *Deterministic delivery of a single atom*, Science **293**.5528 (2001) 278.

[19] D. Schrader et al., *Neutral Atom Quantum Register*, Phys. Rev. Lett. **93** (15 2004) 150501.

[20] Y. Miroshnychenko et al., *Quantum engineering: An atom-sorting machine*, Nature **442**.7099 (2006) 151.

[21] W. S. Bakr et al., *A quantum gas microscope for detecting single atoms in a Hubbard-regime optical lattice*, Nature **462**.7269 (2009) 74.

[22] J. F. Sherson et al., *Single-atom-resolved fluorescence imaging of an atomic Mott insulator*, Nature **467**.7311 (2010) 68.

[23] C. Weitenberg et al., *Single-spin addressing in an atomic Mott insulator*, Nature **471**.7338 (2011) 319.

[24] M. Miranda et al., *Site-resolved imaging of ytterbium atoms in a two-dimensional optical lattice*, Phys. Rev. A **91** (6 2015) 063414.

[25] L. W. Cheuk et al., *Quantum-Gas Microscope for Fermionic Atoms*, Phys. Rev. Lett. **114**.19 (2015) 193001.

[26] M. F. Parsons et al., *Site-Resolved Imaging of Fermionic Li 6 in an Optical Lattice*, Phys. Rev. Lett. **114**.21 (2015) 213002.

[27] D. Jaksch et al., *Fast quantum gates for neutral atoms*, Phys. Rev. Lett. **85**.10 (2000) 2208.

[28] C. Monroe, *Quantum information processing with atoms and photons*, Nature **416**.6877 (2002) 238.

[29] L. Isenhower et al., *Demonstration of a neutral atom controlled-NOT quantum gate*, Phys. Rev. Lett. **104**.1 (2010) 010503.

[30] M. Anderlini et al., *Controlled exchange interaction between pairs of neutral atoms in an optical lattice*, Nature **448**.7152 (2007) 452.

[31] H. Katori et al., *Ultrastable optical clock with neutral atoms in an engineered light shift trap*, Phys. Rev. Lett. **91**.17 (2003) 173005.

[32] M. Takamoto et al., *An optical lattice clock*, Nature **435**.7040 (2005) 321.

[33] A. D. Ludlow et al., *Sr lattice clock at 1× 10–16 fractional uncertainty by remote optical evaluation with a Ca clock*, Science **319**.5871 (2008) 1805.

[34] I. Buluta and F. Nori, *Quantum simulators*, Science **326**.5949 (2009) 108.

[35] J. Simon et al., *Quantum simulation of antiferromagnetic spin chains in an optical lattice*, Nature **472**.7343 (2011) 307.

[36] I. Bloch, J. Dalibard and S. Nascimbene, *Quantum simulations with ultracold quantum gases*, Nat Phys **8**.4 (2012) 267.

[37] M. Lewenstein, A. Sanpera and V. Ahufinger, *Ultracold Atoms in Optical Lattices: Simulating quantum many-body systems*, OUP Oxford, 2012.

[38] M. Karski et al., *Nearest-neighbor detection of atoms in a 1D optical lattice by fluorescence imaging*, Phys. Rev. Lett. **102**.5 (2009) 053001.

[39] S. Kuhr et al.,
Coherence Properties and Quantum State Transportation in an Optical Conveyor Belt,
Phys. Rev. Lett. **91** (21 2003) 213002.

[40] R. Gehr et al., *Cavity-based single atom preparation and high-fidelity hyperfine state readout*,
Phys. Rev. Lett. **104**.20 (2010) 203602.

[41] J. Bochmann et al., *Lossless state detection of single neutral atoms*,
Phys. Rev. Lett. **104**.20 (2010) 203601.

[42] S. Reick et al.,
Analyzing quantum jumps of one and two atoms strongly coupled to an optical cavity,
J. Opt. Soc. Am. B **27**.6 (2010) A152.

[43] A. Fuhrmanek et al., *Free-space lossless state detection of a single trapped atom*,
Phys. Rev. Lett. **106**.13 (2011) 133003.

[44] M. J. Gibbons et al., *Nondestructive fluorescent state detection of single neutral atom qubits*,
Phys. Rev. Lett. **106**.13 (2011) 133002.

[45] M. T. DePue et al., *Unity occupation of sites in a 3D optical lattice*,
Phys. Rev. Lett. **82**.11 (1999) 2262.

[46] N. Schlosser et al., *Sub-poissonian loading of single atoms in a microscopic dipole trap*,
Nature **411**.6841 (2001) 1024.

[47] C. Robens et al.,
Ideal negative measurements in quantum walks disprove theories based on classical trajectories,
Physical Review X **5**.1 (2015) 011003.

[48] I. Bloch, *Ultracold quantum gases in optical lattices*, Nature Physics **1**.1 (2005) 23.

[49] W. Alt, *An objective lens for efficient fluorescence detection of single atoms*,
Optik-International Journal for Light and Electron Optics **113**.3 (2002) 142.

[50] Y. R. Sortais et al., *Diffraction-limited optics for single-atom manipulation*,
Physical Review A **75**.1 (2007) 013406.

[51] S. Pollock et al., *Characteristics of integrated magneto-optical traps for atom chips*,
New Journal of Physics **13**.4 (2011) 043029.

[52] *Thorlabs, Vibration sources and isolation systems tutoral*.

[53] J. Gallego et al.,
High Finesse Fiber Fabry-Perot Cavities: Stabilization and Mode Matching Analysis,
arXiv preprint arXiv:1508.05289 (2015).

[54] A. Öttl et al., *Hybrid apparatus for Bose-Einstein condensation and cavity quantum electrodynamics: Single atom detection in quantum degenerate gases*,
Review of scientific instruments **77**.6 (2006) 063118.

[55] Y. Kuk and P. Silverman, *Scanning tunneling microscope instrumentation*,
Review of scientific instruments (1989).

[56] M. Okano et al., *Vibration isolation for scanning tunneling microscopy*,
Journal of Vacuum Science & Technology A **5**.6 (1987) 3313.

[57] A. Oliva, M. Aguilar and V. Sosa,
Low-and high-frequency vibration isolation for scanning probe microscopy,
Measurement Science and Technology **9**.3 (1998) 383.

[58] A. Oliva et al., *Vibration isolation analysis for a scanning tunneling microscope*, Review of scientific instruments **63**.6 (1992) 3326.

[59] T. P. Meyrath, "Electromagnet Design Basics for Cold Atom Experiments", Atom Optics Laboratory Center for Nonlinear Dynamics University of Texas at Austin.

[60] W. D. Phillips and H. Metcalf, *Laser deceleration of an atomic beam*, Phys. Rev. Lett. **48**.9 (1982) 596.

[61] S. Chu et al., *Three-dimensional viscous confinement and cooling of atoms by resonance radiation pressure*, Physical Review Letters **55**.1 (1985) 48.

[62] E. Raab et al., *Trapping of neutral sodium atoms with radiation pressure*, Phys. Rev. Lett. **59**.23 (1987) 2631.

[63] H. J. Metcalf and P. Van der Straten, *Laser cooling and trapping*, Springer Science & Business Media, 2012.

[64] D. J. Wineland and W. M. Itano, *Laser cooling of atoms*, Physical Review A **20**.4 (1979) 1521.

[65] C. Wieman and T. W. Hänsch, *Doppler-free laser polarization spectroscopy*, Phys. Rev. Lett. **36**.20 (1976) 1170.

[66] W. Alt, *Optical control of single neutral atoms*, PhD thesis: University of Bonn, 2004.

[67] M. Harris et al., *Polarization spectroscopy in rubidium and cesium*, Physical Review A **73**.6 (2006) 062509.

[68] V. Gomer and D. Meschede, *A single trapped atom: Light-matter interaction at the microscopic level*, Annalen der Physik **10**.1-2 (2001) 9.

[69] S. Yoon et al., *Characteristics of single-atom trapping in a magneto-optical trap with a high magnetic-field gradient*, Journal of Physics: Conference Series **80**.1 (2007) 012046.

[70] Z. Hu and H. Kimble, *Observation of a single atom in a magneto-optical trap*, Optics letters **19**.22 (1994) 1888.

[71] C. Cohen-Tannoudji et al., *Atom-photon interactions: basic processes and applications*, Wiley Online Library, 1992.

[72] J. Gordon and A. Ashkin, *Motion of atoms in a radiation trap*, Physical Review A **21**.5 (1980) 1606.

[73] J. Dalibard and C. Cohen-Tannoudji, *Dressed-atom approach to atomic motion in laser light: the dipole force revisited*, JOSA B **2**.11 (1985) 1707.

[74] C.-Y. Shih and M. S. Chapman, *Nondestructive light-shift measurements of single atoms in optical dipole traps*, Physical Review A **87**.6 (2013) 063408.

[75] M. Karski, *State-selective transport of single neutral atoms*, PhD thesis, 2010.

[76] A. Alberti et al., *Super-resolution microscopy of single atoms in optical lattices*, arXiv preprint arXiv:1512.07329 (2015).

[77] R. E. Thompson, D. R. Larson and W. W. Webb,
Precise nanometer localization analysis for individual fluorescent probes,
Biophysical journal **82**.5 (2002) 2775.

[78] S. M. Olmschenk, *Quantum teleportation between distant matter qubits*,
PhD thesis: The University of Michigan, 2009.

[79] *Andor hardware guide*.

[80] K. B. Harpsøe, M. I. Andersen and P. Kjægaard,
Bayesian photon counting with electron-multiplying charge coupled devices (EMCCDs),
Astronomy & Astrophysics **537** (2012) A50.

[81] A. Basden and C. Haniff, *Low light level CCDs and visibility parameter estimation*,
Monthly Notices of the Royal Astronomical Society **347**.4 (2004) 1187.

[82] Y. Voelzke, *Simultaneous Non-Destructive State Detection of Neutral Atoms*,
Master thesis, 2014.

[83] J. B. Pawley, *Points, pixels, and gray levels: digitizing image data*, Springer, 2006.

[84] K. Fliegel, *Modeling and measurement of image sensor characteristics*,
Radioengineering **13**.4 (2004) 27.

[85] T. Williams, *The optical transfer function of imaging systems*, CRC Press, 1998.

[86] H. Hopkins, *The frequency response of a defocused optical system*, Proceedings of the Royal Society of London A: Mathematical, Physical and Engineering Sciences **231**.1184 (1955) 91.

[87] R. Jindra, *Positioning of single atoms in a dipole trap*,
Master thesis: Vienna University of Technology, 2014.

[88] S. L. Winoto et al., *Laser cooling at high density in deep far-detuned optical lattices*,
Physical Review A **59**.1 (1999) R19.

[89] D. Leibfried et al., *Quantum dynamics of single trapped ions*,
Reviews of Modern Physics **75**.1 (2003) 281.

[90] P. Horak et al., *Cavity-induced atom cooling in the strong coupling regime*,
Phys. Rev. Lett. **79**.25 (1997) 4974.

[91] G. Hechenblaikner et al., *Cooling an atom in a weakly driven high-Q cavity*,
Physical Review A **58**.4 (1998) 3030.

[92] V. Vuletic and S. Chu, *Laser cooling of atoms, ions, or molecules by coherent scattering*,
Phys. Rev. Lett. **84**.17 (2000) 3787.

[93] K. Murr et al., *Three-dimensional cavity cooling and trapping in an optical lattice*,
Physical Review A **73**.6 (2006) 063415.

[94] F. Marquardt et al., *Quantum theory of cavity-assisted sideband cooling of mechanical motion*,
Phys. Rev. Lett. **99**.9 (2007) 093902.

[95] H. Ritsch et al., *Cold atoms in cavity-generated dynamical optical potentials*,
Reviews of Modern Physics **85**.2 (2013) 553.

[96] G. Morigi, J. Eschner and C. H. Keitel,
Ground state laser cooling using electromagnetically induced transparency,
Phys. Rev. Lett. **85**.21 (2000) 4458.

[97] G. Morigi, *Cooling atomic motion with quantum interference*, Physical Review A **67**.3 (2003) 033402.

[98] D. J. Wineland, J. Dalibard and C. Cohen-Tannoudji, *Sisyphus cooling of a bound atom*, JOSA B **9**.1 (1992) 32.

[99] R. Taieb et al., *Cooling and localization of atoms in laser-induced potential wells*, Physical Review A **49**.6 (1994) 4876.

[100] M. Gehm et al., *Dynamics of noise-induced heating in atom traps*, Physical Review A **58**.5 (1998) 3914.

[101] C. Cohen-Tannoudji and S. Reynaud, *Dressed-atom description of resonance fluorescence and absorption spectra of a multi-level atom in an intense laser beam*, Journal of Physics B: Atomic and Molecular Physics **10**.3 (1977) 345.

[102] R. Robinett, *Quantum and classical probability distributions for position and momentum*, American Journal of Physics **63**.9 (1995) 823.

[103] L. Yatsenko and H. Metcalf, *Dressed-atom description of the bichromatic force*, Physical Review A **70**.6 (2004) 063402.

[104] M. Plenio and P. Knight, *The quantum-jump approach to dissipative dynamics in quantum optics*, Reviews of Modern Physics **70**.1 (1998 and references therein.) 101.

[105] R. Dum, P. Zoller and H. Ritsch, *Monte Carlo simulation of the atomic master equation for spontaneous emission*, Physical Review A **45**.7 (1992) 4879.

[106] K. Mølmer, Y. Castin and J. Dalibard, *Monte Carlo wave-function method in quantum optics*, JOSA B **10**.3 (1993) 524.

[107] L. D. Landau, *Zur Theorie der Energieübertragung. II*, Physics of the Soviet Union **2**.46-51 (1932) 28.

[108] C. Zener, "Non-adiabatic crossing of energy levels", *Proceedings of the Royal Society of London A: Mathematical, Physical and Engineering Sciences*, vol. 137, 833, The Royal Society, 1932 696.

[109] E. K. G. Stueckelberg, *Theorie der unelastischen Stösse zwischen Atomen*, Birkhäuser, 1933.

[110] D. A. Steck, *Quantum and atom optics*, 2007.

[111] J. T. Barreiro et al., *An open-system quantum simulator with trapped ions*, Nature **470**.7335 (2011) 486.

[112] P. M. Preiss et al., *Strongly correlated quantum walks in optical lattices*, Science **347**.6227 (2015) 1229.

[113] R. Gerritsma et al., *Quantum simulation of the Dirac equation*, Nature **463**.7277 (2010) 68.

[114] J. Benhelm et al., *Towards fault-tolerant quantum computing with trapped ions*, Nature Physics **4**.6 (2008) 463.

[115] D. McGloin et al., *Applications of spatial light modulators in atom optics*, Opt. Express **11**.2 (2003) 158.

[116] O. Mandel et al., *Controlled collisions for multi-particle entanglement of optically trapped atoms*, Nature **425**.6961 (2003) 937.

[117] R. Islam et al.,
Measuring entanglement entropy through the interference of quantum many-body twins,
arXiv preprint arXiv:1509.01160 (2015).

[118] M. E. Rose, *Elementary theory of angular momentum*, Courier Corporation, 1995.

[119] M. Acton et al., *Near-perfect simultaneous measurement of a qubit register*,
Quantum Info. Comput. **6**.6 (2006) 465.

[120] A. H. Burrell et al., *Scalable simultaneous multiqubit readout with* 99.99% *single-shot fidelity*,
Phys. Rev. A **81** (4 2010) 040302.

[121] S. Brakhane et al., *Bayesian feedback control of a two-atom spin-state in an atom-cavity system*,
Phys. Rev. Lett. **109**.17 (2012) 173601.

[122] D. S. Sivia, *Data analysis: a Bayesian tutorial*, Oxford university press, 1996.

[123] S. Kuhr, *A controlled quantum system of individual neutral atoms*,
PhD thesis: University of Bonn, Germany., 2003.

[124] C. H. Bennett and D. P. DiVincenzo, *Quantum information and computation*,
Nature **404**.6775 (2000) 247.

[125] H. P. Specht et al., *A single-atom quantum memory*, Nature **473**.7346 (2011) 190.

[126] T. Wilk et al., *Single-atom single-photon quantum interface*, Science **317**.5837 (2007) 488.

[127] T. Northup and R. Blatt, *Quantum information transfer using photons*,
Nature Photonics **8**.5 (2014) 356.

[128] D. Hunger et al., *A fiber Fabry–Perot cavity with high finesse*,
New Journal of Physics **12**.6 (2010) 065038.

[129] R. H. Dicke, *Coherence in spontaneous radiation processes*, Physical Review **93**.1 (1954) 99.

[130] Y. Colombe et al.,
Strong atom–field coupling for Bose–Einstein condensates in an optical cavity on a chip,
Nature **450**.7167 (2007) 272.

[131] F. Brennecke et al., *Cavity QED with a Bose–Einstein condensate*, Nature **450**.7167 (2007) 268.

[132] R. Zhao et al., *Long-lived quantum memory*, Nature Physics **5**.2 (2009) 100.

[133] D. Matsukevich and A. Kuzmich, *Quantum state transfer between matter and light*,
Science **306**.5696 (2004) 663.

[134] C.-W. Chou et al.,
Measurement-induced entanglement for excitation stored in remote atomic ensembles,
Nature **438**.7069 (2005) 828.

[135] L. Paulet, *Raman and Microwave Manipulation of Small Atomic Ensembles*,
Master thesis: Institut fuer Angewandte Physik, Universität Bonn, 2014.

[136] J. Camparo and R. Frueholz,
Parameters of adiabatic rapid passage in the 0-0 hyperfine transition of Rb 87,
Physical Review A **30**.2 (1984) 803.

[137] K. Bergmann, H. Theuer and B. Shore,
Coherent population transfer among quantum states of atoms and molecules,
Reviews of Modern Physics **70**.3 (1998) 1003.

[138] B. Shore, *The theory of coherent atomic excitation*, John Wiley & Sons, Inc., New York, 1990.

[139] I. Dotsenko, *Raman spectroscopy of single atoms*,
Master thesis: Institut fuer Angewandte Physik,Universität Bonn, 2002.

[140] Q. Turchette et al., *Heating of trapped ions from the quantum ground state*,
Physical Review A **61**.6 (2000) 063418.

[141] C. Monroe et al.,
Resolved-Sideband Raman Cooling of a Bound Atom to the 3D Zero-Point Energy,
Phys. Rev. Lett. **75** (22 1995) 4011.

[142] L. Landau and E. Lifshitz, *Mechanics, vol. 1*, 1976.

[143] W. Alt et al., *Single atoms in a standing-wave dipole trap*,
Physical Review A **67**.3 (2003) 033403.

[144] M. Khudaverdyan et al.,
Quantum jumps and spin dynamics of interacting atoms in a strongly coupled atom-cavity system,
Phys. Rev. Lett. **103**.12 (2009) 123006.

[145] J. Volz et al., *Measurement of the internal state of a single atom without energy exchange*,
Nature **475**.7355 (2011) 210.

[146] M. J. Kastoryano, F. Reiter and A. S. Sørensen,
Dissipative preparation of entanglement in optical cavities,
Phys. Rev. Lett. **106**.9 (2011) 090502.

[147] D. Schrader, *A Neutral Atom Quantum Register*, PhD thesis: Universität Bonn, 2004.

[148] C. Zipkes et al., *Kinetics of a single trapped ion in an ultracold buffer gas*,
New Journal of Physics **13**.5 (2011) 053020.

[149] P. Van Mieghem, *Performance analysis of communications networks and systems*,
Cambridge University Press, 2006.

[150] T. Takekoshi, J. Yeh and R. Knize, *Quasi-electrostatic trap for neutral atoms*,
Optics communications **114**.5 (1995) 421.

[151] D. A. Steck, *Rubidium 87 D line data*, 2001.

Acknowledgments

It has been a long way the busy but also exciting road of working on this Ph.D. thesis. I was guided and supported by many people, to whom I am very grateful.

Firstly, and most of all, I would like to thank Prof. Dieter Meschede for giving me the opportunity of being part of his group and financially supporting me during this thesis. Thanks for letting me work in the fascinating field of atomic physics and play with single atoms.

I greatly appreciate the financial support during this thesis from the Atomic Quantum Technologies (EU, AQUTE), the Bundesministerium für Bildung und Forschungduring (BMBF), the State of Nordrhein-Westfalen, and from the Bonn-Cologne Graduate School for Physics and Astronomy (BCGS).

I want to sincerely thank current and former post-docs Dr. Wolfgang Alt and Dr. Marcel Spurny for sharing their knowledge and providing me with answers and solutions to many different questions and complications through these years. Thanks to Dr. Andrea Alberti for sharing his image analysis knowledge and useful tools. My deepest gratitude goes to Dr. Lothar Ratschbacher for the professional guidance and advice, for sharing his theoretical and experimental knowledge which has made my research experience very rewarding. Thanks for all the help provided in the lab, the useful suggestions and enlightening discussions.

I would also to thank all current and former members of the FCQED experiment: Dr. Wolfgang Alt, José Gallego, Sutapa Ghosh, Lucie Paulet, Dr.Lothar Ratschbacher, Dr. Marcel Spurny and Yannik Völzke. Thanks for all the fruitful discussions and all the help you have given me through these years and for the nice time during this project. Without you, this work would not have been possible to complete. I also want to thank the rest of my colleagues in the research group for always having an ear for discussions, stories and complaints, and for creating a pleasant working atmosphere. I would also like to thank Wolfgang Alt, José C. Gallego Fernández, Dr. Lothar Ratschbacher, Carsten Robens and Natalie Thau for the extensive proofreads and useful suggestions for this manuscript.

I would like to thank all the other members of Prof. Meschede's group, Annelise Miglo, Fien Latumahina and Dietmar Haubrich, for all their help for administrative and bureaucratic paperwork. And also thanks to all the staff of the mechanical and electronic workshops for all the equipment and devices manufactured

Quiero agradecer en especial a Miriam por haber compartido esta experiencia conmigo, y por todo su apoyo incondicinal a través de estos años por lo cual siempre estaré infinitamente agradecido.

Quiero agradecer a mi madre por apoyarme desde lejos y por todo el amor que me ha brindado. También quiero agradecer al resto de mi famila por el apoyo a lo largo de todos estos años, no tengo palabras para expresarles mi gratitud.